(12)

AD-A149 472

AD

B
R
L

MEMORANDUM REPORT BRL-MR-3417

A STUDY OF SHAPED-CHARGE COLLAPSE AND JET FORMATION USING THE HEMP CODE AND A COMPARISON WITH EXPERIMENTAL OBSERVATIONS

Brian M. Simmons

December 1984

US ARMY BALLISTIC RESEARCH LABORATORY
ABERDEEN PROVING GROUND, MARYLAND

UNCLASSIFIED
SECURITY CLASSIFICATION OF THIS PAGE (When Data Entered)

REPORT DOCUMENTATION PAGE		READ INSTRUCTIONS BEFORE COMPLETING FORM
1. REPORT NUMBER MEMORANDUM REPORT BRL-MR-3417	2. GOVT ACCESSION NO. AD-A149472	3. RECIPIENT'S CATALOG NUMBER
4. TITLE (and Subtitle) A STUDY OF SHAPED-CHARGE COLLAPSE AND JET FORMATION USING THE HEMP CODE AND A COMPARISON WITH EXPERIMENTAL OBSERVATIONS		5. TYPE OF REPORT & PERIOD COVERED FINAL 6. PERFORMING ORG. REPORT NUMBER
7. AUTHOR(s) Brian M. Simmons		8. CONTRACT OR GRANT NUMBER(s)
9. PERFORMING ORGANIZATION NAME AND ADDRESS USA Ballistic Research Laboratory ATTN: AMXBR-TBD Aberdeen Proving Ground, MD 21005-5066		10. PROGRAM ELEMENT, PROJECT, TASK AREA & WORK UNIT NUMBERS 1L162618AH80
11. CONTROLLING OFFICE NAME AND ADDRESS US Army Ballistic Research Laboratory ATTN: AMXBR-OD-ST Aberdeen Proving Ground, MD 21005-5066		12. REPORT DATE DECEMBER 1984 13. NUMBER OF PAGES 111
14. MONITORING AGENCY NAME & ADDRESS(if different from Controlling Office)		15. SECURITY CLASS. (of this report) UNCLASSIFIED 15a. DECLASSIFICATION/DOWNGRADING SCHEDULE

16. DISTRIBUTION STATEMENT (of this Report)

Approved for Public Release; Distribution Unlimited.

17. DISTRIBUTION STATEMENT (of the abstract entered in Block 20, if different from Report)

18. SUPPLEMENTARY NOTES

19. KEY WORDS (Continue on reverse side if necessary and identify by block number)

HEMP Code
Shaped-Charge Collapse
Shaped Charges
Jet Formation
Jet Characteristics
Radiographs

20. ABSTRACT (Continue on reverse side if necessary and identify by block number)

The HEMP code was used to model shaped-charge collapse and jet formation processes for several charge configurations. Jet characteristics were determined by coupling the HEMP code output to the jet formation theory of Birkhoff, MacDougall, Pugh and Taylor. A new feature of this study with HEMP is an explicit rule for determining when a liner segment collapses into the jet flow.

Radiographs of shaped charges tested at BRL were compared to HEMP simula-

DD FORM 1 JAN 73 1473 EDITION OF 1 NOV 65 IS OBSOLETE

UNCLASSIFIED
SECURITY CLASSIFICATION OF THIS PAGE (When Data Entered)

tions of the collapse process and the jet velocity/mass distributions calculated for each modelled configuration. An experimental data base of velocity/mass distributions was obtained and compared with the calculated distributions. A one-to-one mapping was done showing each liner segment's position in the initial HEMP grid versus its relative position in the jet.

TABLE OF CONTENTS

LIST OF ILLUSTRATIONS

LIST OF ILLUSTRATIONS (Continued)

LIST OF ILLUSTRATIONS (Continued)

LIST OF ILLUSTRATIONS (Continued)

LIST OF TABLES

I. INTRODUCTION

There is a constant need in the Warhead Mechanics Branch of the Terminal Ballistics Division, Ballistic Research Laboratory (BRL), to quantitatively describe a given shaped-charge's behavior. A computer modelling process is needed which will give quick approximations of jet characteristics and alleviate the need for extensively testing new shaped-charge designs.

The HEMP computer program uses Lagrangian formulation to solve the conservation equations of mass, momentum, and energy for two-dimensional elastic-plastic flow.[1] The many applications of the HEMP code are well documented; it is known to simulate the gross deformation of a shaped-charge liner under extreme pressures reasonably well.[2] In choosing the Lagrangian code HEMP instead of BRLSC, an Eulerian code available at BRL, reference is made to comparisons of the collapse velocities calculated by each with experimental values.[3-4] The collapse velocity distribution calculated using HEMP was shown to be more accurate. Furthermore, the accuracy of the final jet velocity calculated is sensitive to the accuracy of the collapse velocity distribution over the liner region.[3] Another reason for choosing a Lagrangian code is the extensive amount of computer time required to complete a problem of this type with an Eulerian code. The HEMP hydrocode is currently available on the CDC Cyber 170 computer system at BRL and hence was chosen for this study.

---

[1] *M.L. Wilkins, "Calculation of Elastic-Plastic Flow," UCRL-7322, January 1969.*

[2] *R.R. Karpp, "Accuracy of HEMP Code Solutions," BRL-MR-2268, January 1973. AD# 757 153.*

[3] *J.T. Harrison, R.R. Karpp, "Terminal Ballistic Application of Hydrodynamic Computer Code Calculations," BRL R 1984, April 1977. AD# 041 065.*

[4] *J.T. Harrison, "A Comparison Between The Eulerian Hydrodynamic Computer Code (BRLSC) and Experimental Collapse of a Shaped Charge Liner," ARBRL-MR-02841, June 1978. AD# 057 711.*

Shaped-charge jet characteristics were derived using the output from HEMP and the jet formation equations of Birkhoff, MacDougall, Pugh and Taylor.[5] For any given liner configuration, these equations predict the jet velocity and mass, and the slug velocity and mass for each liner segment designated in the initial grid, provided the collapse velocity and collapse angle are known for each segment.

The collapse process simulated using HEMP was compared to radiographs of an 81mm, 42°, Composition B (Comp. B) - loaded charge at various stages of collapse. Velocity/mass distributions were reduced from radiographs of experimental charges fired during tests conducted at BRL and compared to those distributions obtained by applying the theory of Birkhoff et al.,[5] to the HEMP code output.

II. HEMP CODE SIMULATIONS

The HEMP computer program (Hydrodynamic, Elastic, Magneto, and Plastic) was used to study the collapse process and jet characteristics of 42° and 60° shaped charges. The charges studied had conical, copper liners, 2mm thick and were loaded with either Comp. B* or Octol** explosive. The experimental charges were lightly confined with aluminum bodies and had cone diameters of 84mm. The charges modelled using HEMP were unconfined but used an additional 1.5mm of explosive as an approximation to the detonation effects resulting from the aluminum confinement. To model confinement around a shaped-charge with HEMP, a slide-line routine is necessary separating the metal and explosive. Due to the proximity of this metal confinement to the initiation point of the explosive, large distortions are induced early in the problem, and run times are shortened. The modelled charges also differed by having cone diameters of 81mm. The 81mm shaped charge is the BRL "lab standard" and the jet characteristics between the 81mm and the 84mm charges are virtually identical, with slightly more mass in the jet from the wider charge. The experimental shaped charges are shown in Figures 1 and 2. The basic HEMP configurations used to model these charges are shown in Figures 3 and 4. Alternate configurations will be discussed later.

---

[5] *G. Birkhoff, D.P. MacDougall, E.M. Pugh, G. Taylor, "Explosives with Lined Cavities," Journal of Applied Physics, Vol. 19, No. 6, June 1948.*

**Comp. B composed of 60% by weight RDX and 40% TNT.*

***Octol composed of 75% by weight HMX and 25% TNT.*

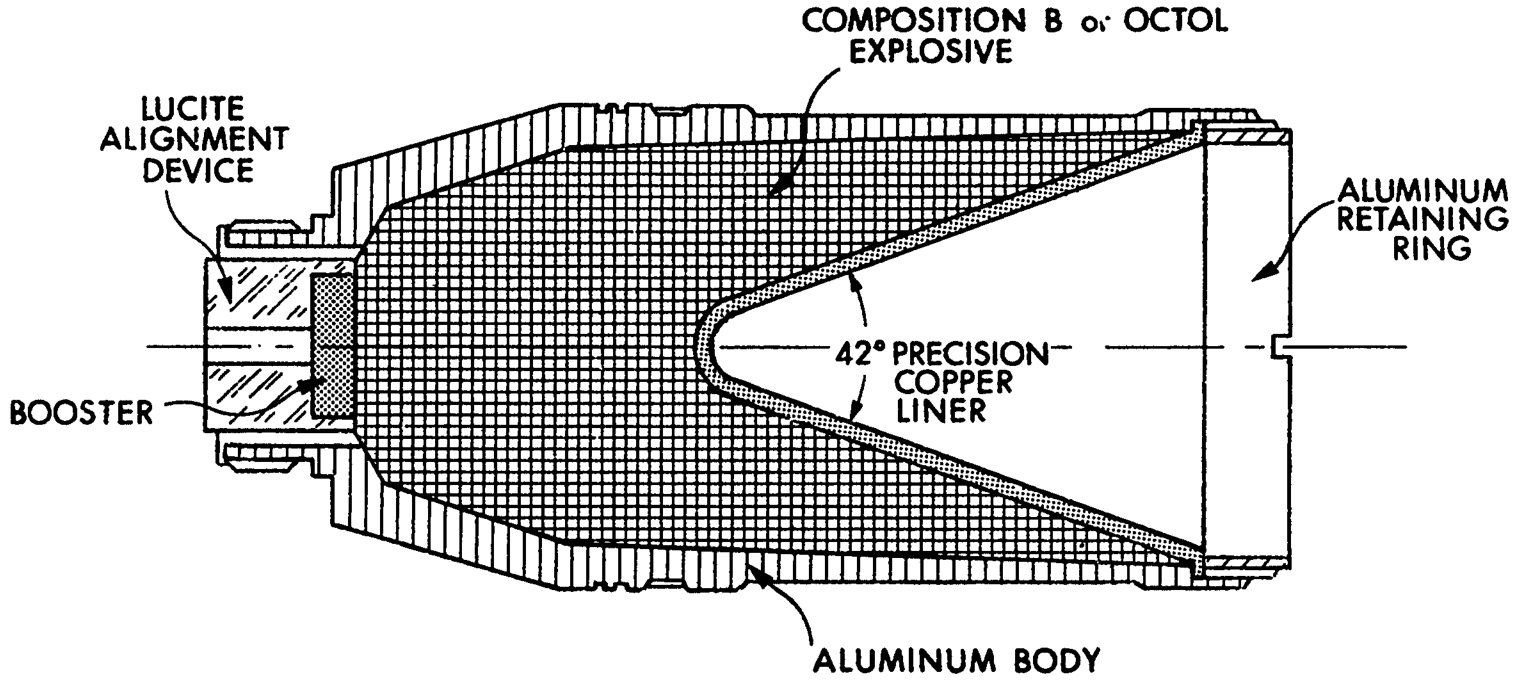

Figure 1. 42° Experimental Charge.

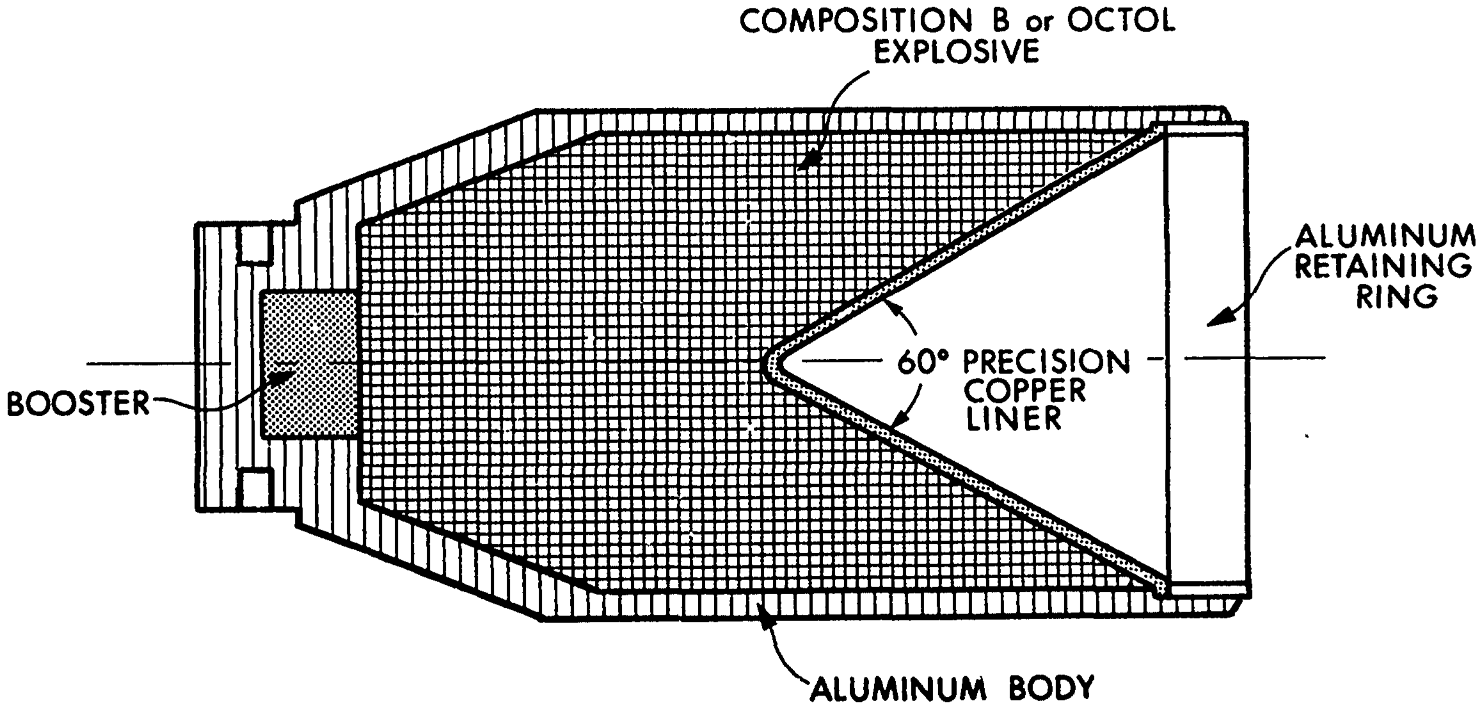

Figure 2. 60° Experimental Charge.

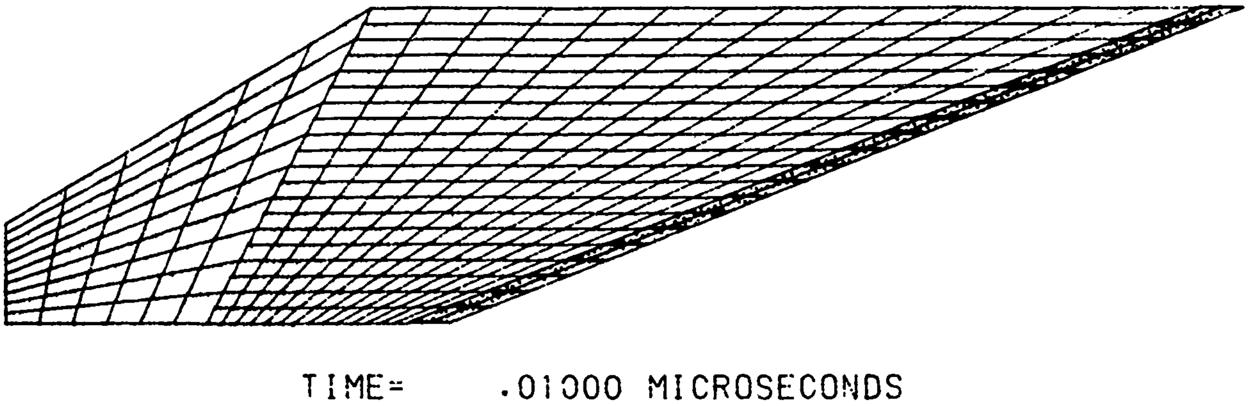

Figure 3. 42° Basic HEMP Configuration.

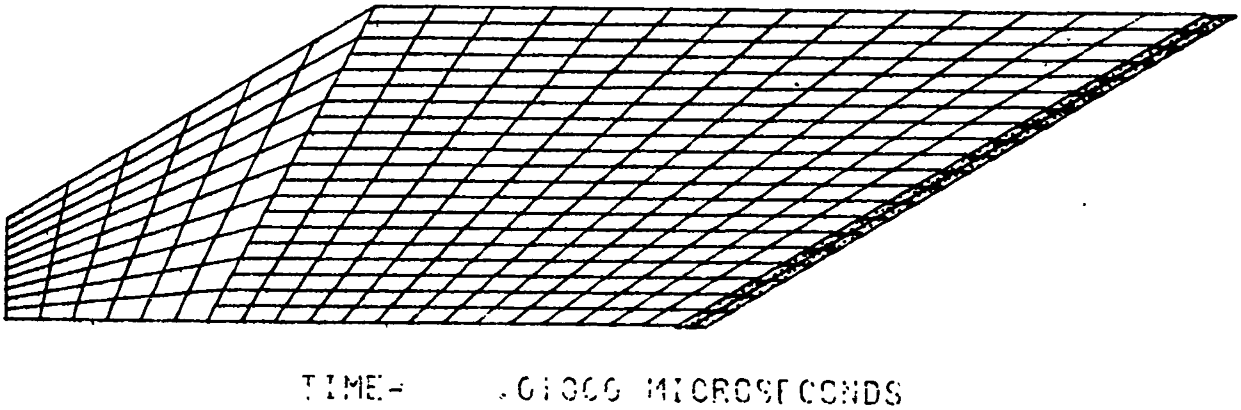

Figure 4. 60° Basic HEMP Configuration.

The initial HEMP configuration requires a grid structure composed of J and K lines. Our orientation of this grid is illustrated in Figure 5. The modelled charge configurations were divided into three blocks: Block 1, containing the liner material between the K_{MAX} and K_{MAX-2} lines; Block 2, containing the fine-zoned explosive adjacent to the liner; and Block 3, containing the coarse-zoned explosive at the tapered end of the charge. Slide-line routines were implemented at the explosive/metal interface (line $K_{MAX-2)}$ and along the K line separating blocks 2 and 3. Both slide-lines were extended vertically through the J_{MAX} surface and at opposite 45° angles through the J_{MIN} surface. The directions of these extensions are included in the HEMP slide-line routine and for the configurations studied approximate the physical expansion of the explosive gases. A stonewall routine (fixed, rigid boundary) was set up along the J_{MAX} surface to represent reflection about the axis of symmetry. Extended computations of HEMP were achieved using forced time steps, a standard input, which were sufficiently small to by-pass the automatic cut-off that halts the problem when the HEMP computed time step gets too small.

The explosive regions were detonated by single point initiation at $J=J_{MAX}$, $K=K_{MIN}$. JWL equations of state[6] were used for the Comp. B and Octol* explosives. An equation of state generated for the shaped-charge version of HEMP by Dr. Robert Karpp at BRL was used for the copper liners.[7]

A plotting package developed by Mr. John Harrison of BRL was included in the version of HEMP used in this study. Two plots are generated at each edit cycle. Both show new node point locations relative to the initial grid; however, one plot includes the velocity vectors associated with each node point.

---

[6] *B.M. Dobratz, "LLNL Explosives Handbook, Properties of Chemical Explosives and Explosive Simulants," UCRL-52997, March 1981.*

[7] *R.R. Karpp,* $P(\mu) = 1.19\mu + 4.435\mu^2$.

**Equations of state for Octol was for a 78% HMX/22% TNT mix.*

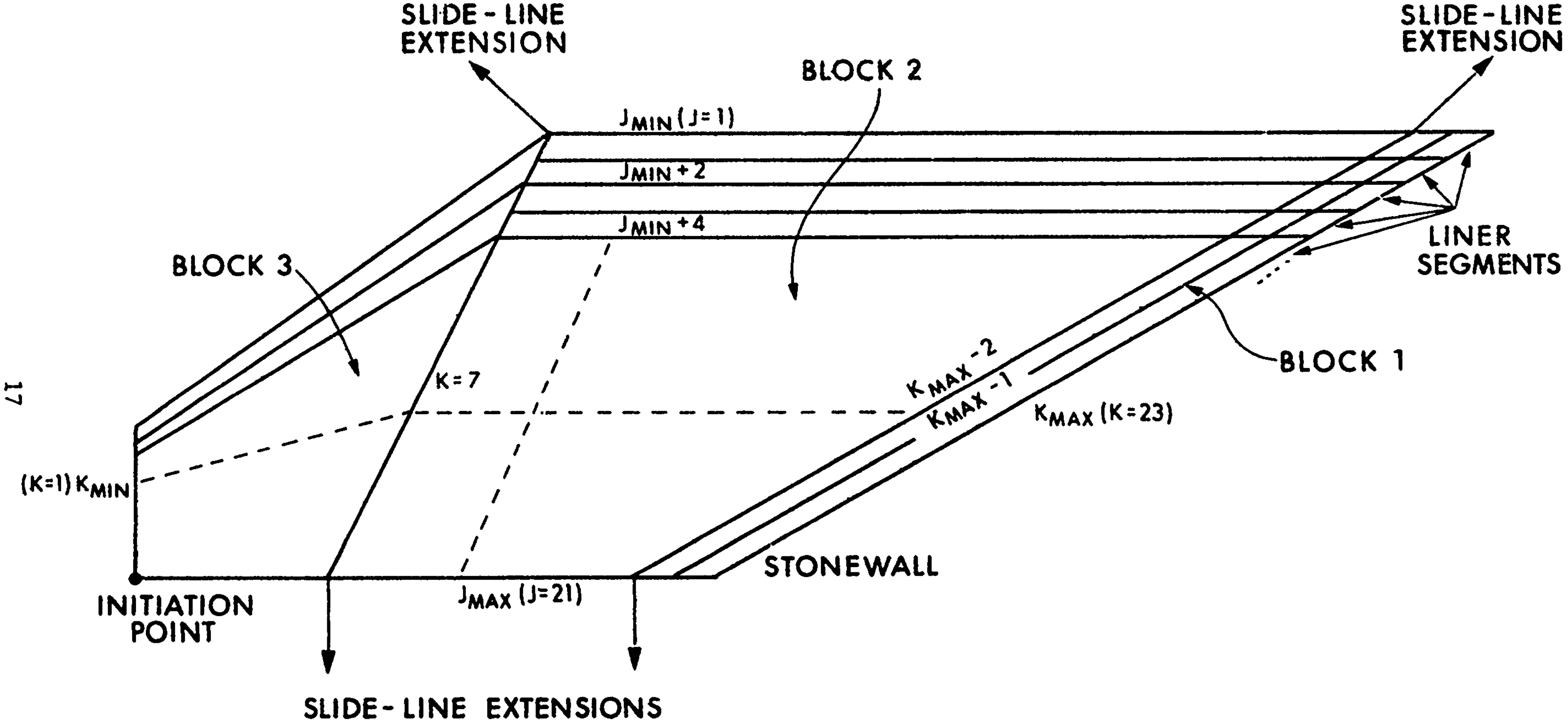

Figure 5. Orientation of the HEMP Grid.

III. DERIVATION OF SHAPED-CHARGE CHARACTERISTICS

In the study of jet formation with a Lagrangian computer program that cannot follow the jetting process without rezoning, it is essential for the proper application of the Birkhoff, MacDougall, Pugh and Taylor theory[5] to know, as accurately as possible, when a liner segment enters the jetting phase. Determination of the collapse angle and collapse velocity for each liner segment is derived from the HEMP code output at this time of collapse.

A method for determining when a liner segment collapses and enters the jet flow follows. When a detonation wave propagating through an explosive approaches a liner segment, the velocity of that segment in the axial direction steadily increases. As the detonation wave sweeps farther down the liner, the segment collapses into the jetting region and its axial velocity is suddenly and drastically accelerated. The collapse of a liner segment occurs immediately prior to its entering the jet flow; thus, the collapse time for any liner segment can be defined as the point in time when that segment's axial velocity changes from a gradually accelerating trend to a rapidly accelerating trend.

A similar approach was taken by Harrison and Karpp[3] for identifying the collapse times of the liner segments. In their study, the collapse velocities were calculated along the center line of the liner at the times when the radial velocity components reached maximum values. The radial components exhibit fluctuations in velocity with time indicating covergence towards the cone axis before jetting occurs due to the inward pressure from the detonation wave. By analyzing the axial velocity components, it becomes more apparent when the jetting process occurs.

At every edit cycle specified by the programmer, HEMP output lists all grid nodes in the problem describing their relative positions and corresponding axial and radial velocity components. Knowing the axial velocities, the collapse time of any liner segment* can be inferred from a plot showing axial velocity versus time. This concept is illustrated in Figure 6 for the K_{MAX} node points. When these nodes points "jet," the entire segment is assumed to jet. Figure 7 shows a "time-history" plot of the collapsing liner segments of a 42° shaped charge loaded with Comp. B explosive from the basic HEMP configuration.

**Note - Usually HEMP does not run to sufficient times to collapse the entire liner. The several zones that do not collapse are located at the base of the liner and hence, would be the rear, slower moving portion of the jet.*

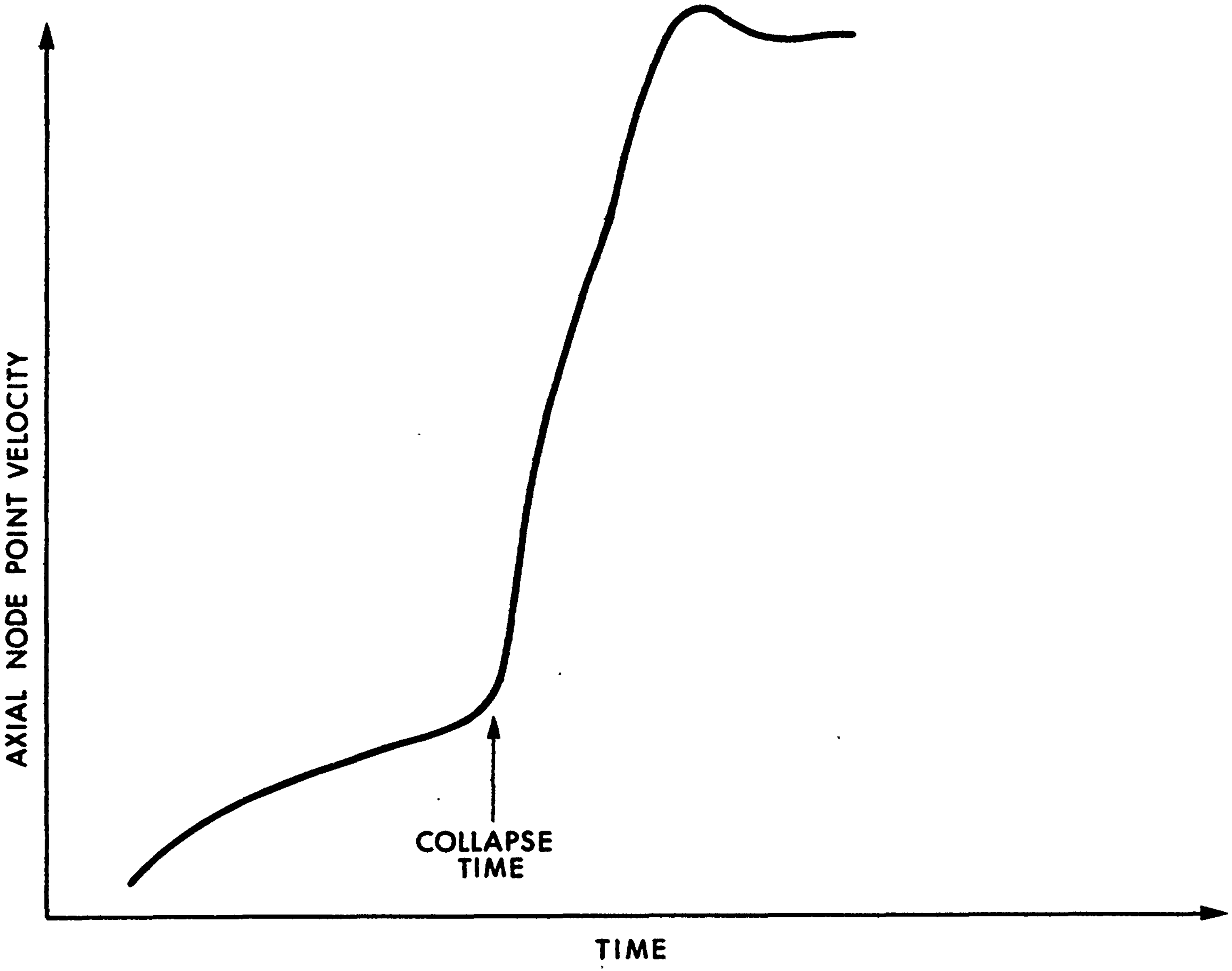

Figure 6. Axial Velocity/Time Plot used to Determine the Collapse Time of a Liner Segment.

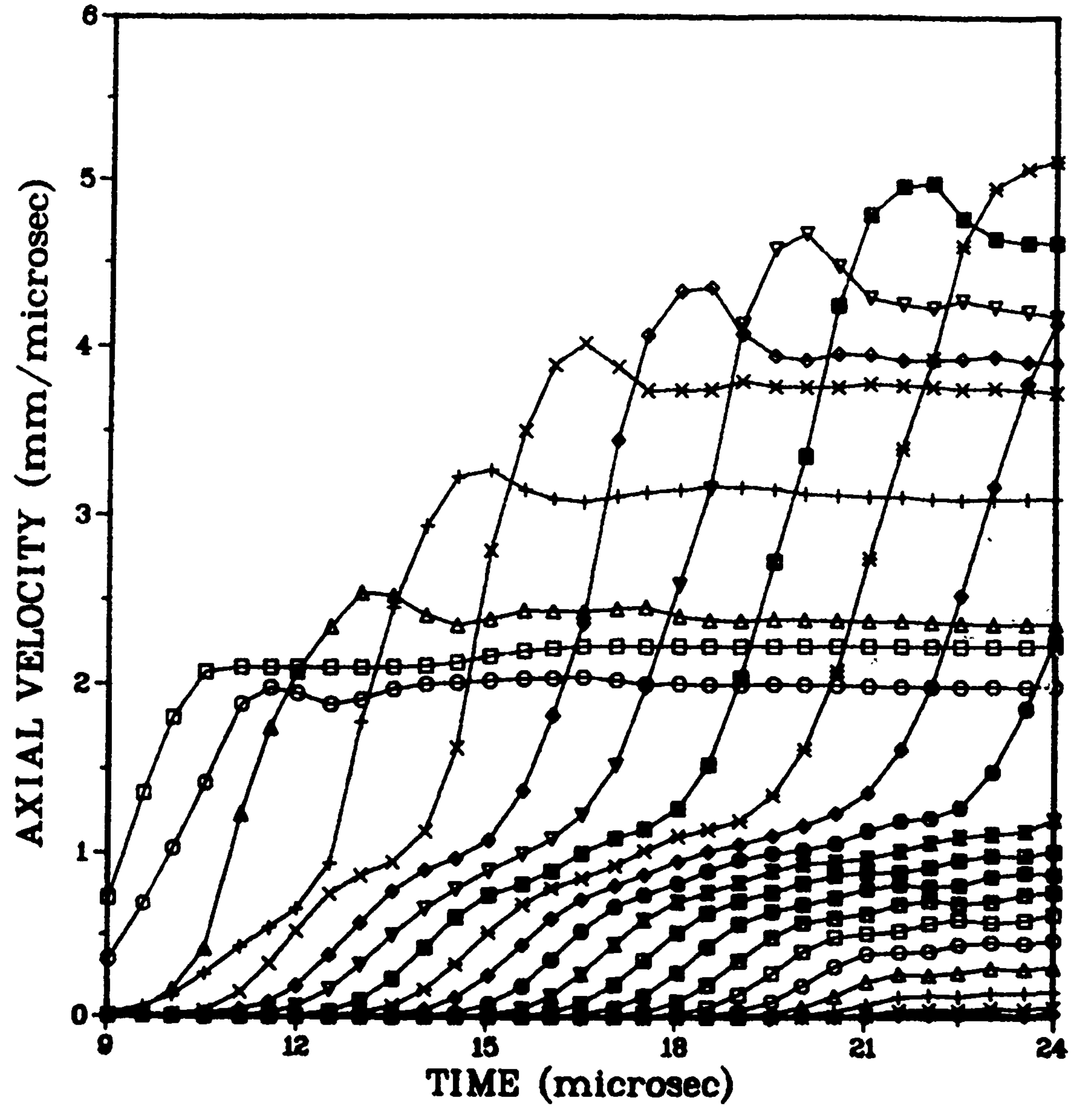

Figure 7. Axial Velocity/Time Plot for the Collapsing Liner Segments of a 42° Shaped Charge Loaded With Comp. B Explosive from the Basic HEMP Configuration.

The symbols plotted represent the modelled liner segments at each edit cycle. The first segments to collapse are at the apex region and those collapsing later in time are towards the base of the liner.

Once the time of collapse has been determined for each liner segment, the collapse angle, β, can be measured directly from the plots generated at the edit cycles corresponding to the observed collapse times. The collapse angle is the angle the collapsing liner wall makes with the cone axis. The portion of a liner segment's mass that divides into jet or slug is dependent on the angle β, as is the velocity that mass will acquire. Measurement of β was done by drawing a straight line through the collapsing zone along the line separating the two liner halves. The angle between this line and the axis of symmetry was recorded as β. This is illustrated in Figure 8 for liner segment #9 of the 42° Comp. B basic configuration. At best, this measurement can only be as accurate as the accuracy associated with the computer generated plot. A realistic estimate for the error in measuring β is ± 0.5°.

The collapse velocity, V_o, for any liner segment can be calculated directly from the HEMP output at the respective collapse time. The collapse velocity may be expressed in terms of a segment's axial and radial velocity components by the following relationship:

$$V_o = \sqrt{\left(V_{o_Z}\right)^2 + \left(V_{o_R}\right)^2}\,, \tag{1}$$

where V_o is the collapse velocity of the segment, and V_{o_Z} and V_{o_R} are its respective axial and radial velocity components. In vector form, the relationship is:

$$\vec{V}_o = \vec{V}_{o_Z} + \vec{V}_{o_R}\,, \tag{2}$$

where the collapse velocity vector, $\vec{V}_o$, is the resultant of the addition of the axial and radial velocity vectors, $\vec{V}_{o_Z}$ and $\vec{V}_{o_R}$.

The direction of the collapse velocity vector, θ, may be

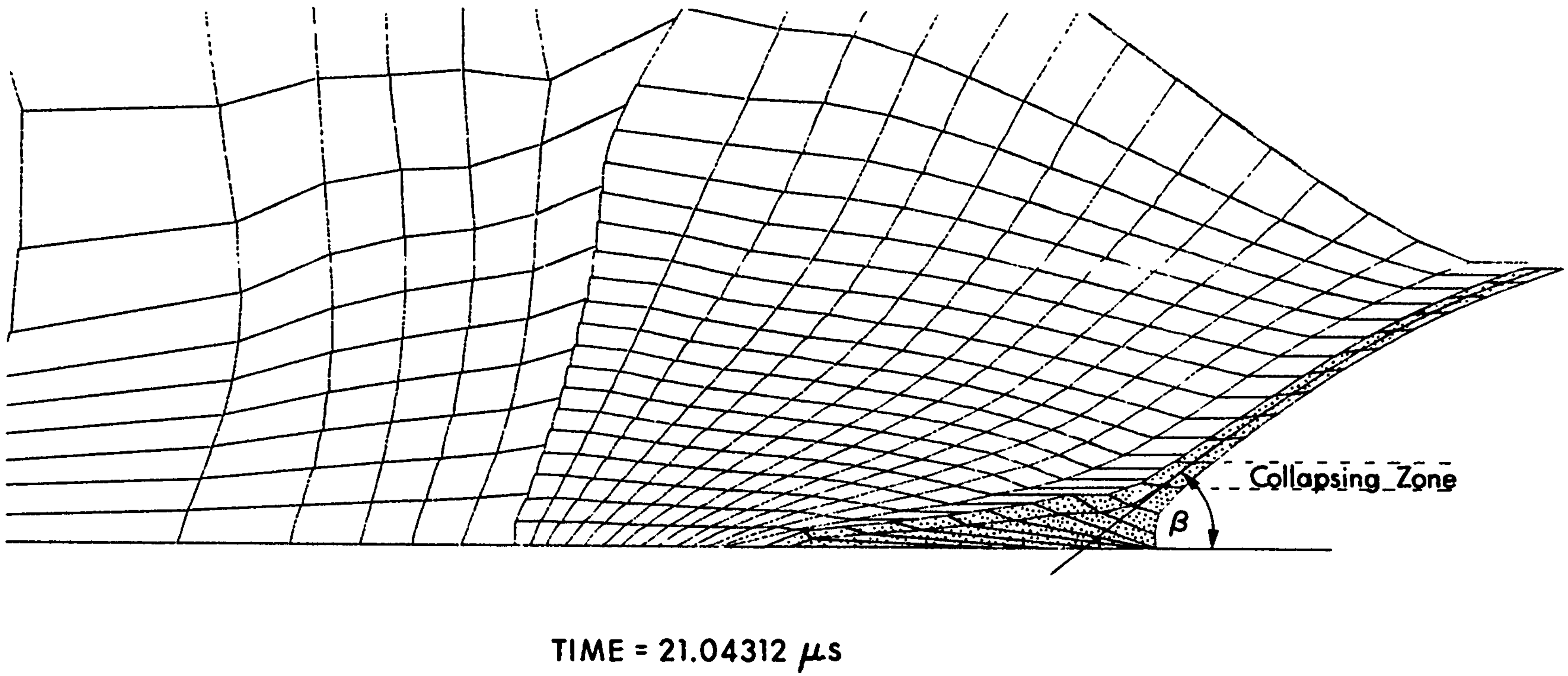

Figure 8. Measurement of the Collapse Angle, β.

determined by using the following equation:

$$\theta = \tan^{-1}\left(\frac{|\vec{V}_{o_Z}|}{|\vec{V}_{o_R}|}\right) . \qquad (3)$$

This is shown in Figure 9.

Collapse velocities and their directions were calculated along the K_{MAX} and K_{MAX-1} lines at every J line. The K_{MAX} line (K-outer) is the inside surface of the liner material and the K_{MAX-1} line (K-middle) is the center line between the liner halves (see Figure 5). Output from HEMP indicated a velocity gradient existed across the entire liner (lines K_{MAX} to K_{MAX-2}), however, our area of interest for collapse velocities was limited to the K-outer and K-middle lines. According to the theory of Birkhoff et al.,[5] the liner material divides into two parts during the collapse process, the inside portion of the liner forming the fast-moving jet and the outside portion forming the slower-moving slug. The division of liner mass occurs at the stagnation point. Since the slug contains much more of the original liner mass than the jet, we can deduce that the jet is formed from the innermost region of the liner at some line between the K-outer and K-middle lines. Figure 10 shows this division of liner mass into jet and slug.

The collapse velocities calculated for the 42°, Comp. B-loaded charge using the basic HEMP configuration are plotted in Figure 11 as a function of liner position. The velocity gradient between the K-outer and K-middle lines is evident, the K-outer line collapsing faster throughout most of the distribution. The symbols on the graph are actual values calculated by HEMP; the curves are fifth degree polynomial fits to these values. This "data-smoothing" technique was applied to compensate for the discontinuity in the collapse process as calculated by HEMP. If the strength of the liner material is negligible due to the tremendous pressures exerted on it during collapse, the liner material may be treated as a perfect fluid.[5] This assumption made by Birkhoff et al.,[5] causes an intuitive feeling that the collapse process is indeed a smooth, continuous process. The smoothed collapse velocity values were used in subsequent calculations involving collapse velocities.

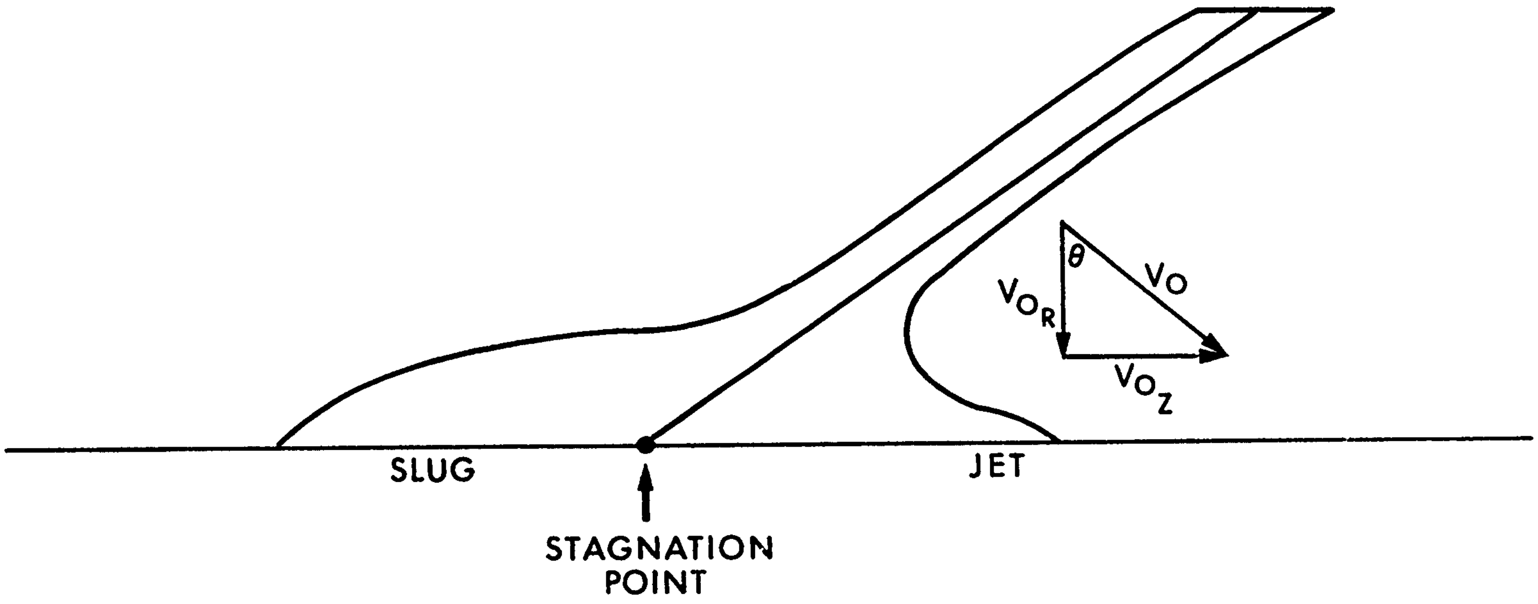

$$V_O = \sqrt{(V_{O_Z})^2 + (V_{O_R})^2}$$

Figure 9. Relationship of the Collapse Velocity Vector, $\vec{V}_o$, to the Axial Velocity Vector, $\vec{V}_{o_Z}$, and the Radial Velocity Vector, $\vec{V}_{o_R}$.

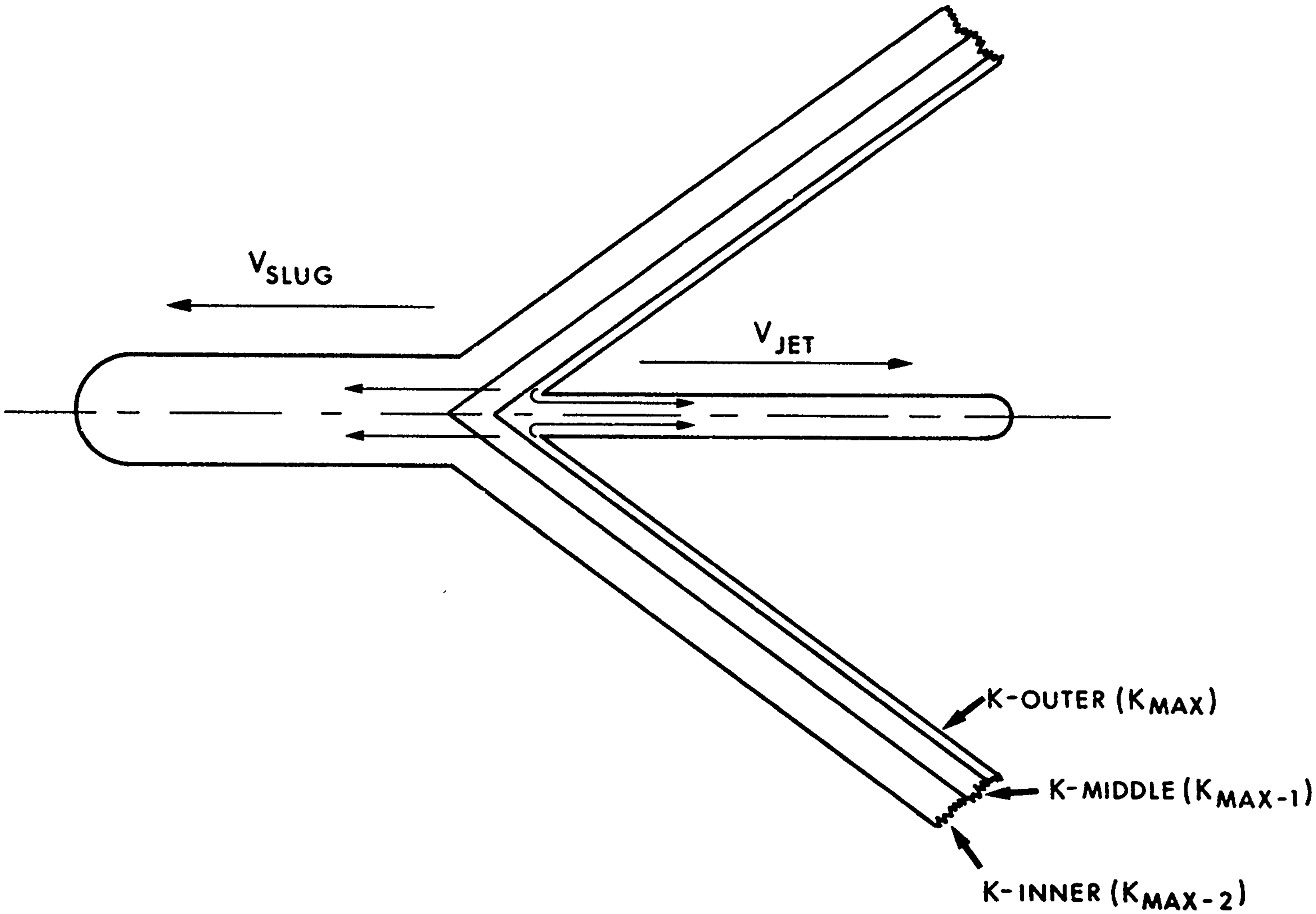

Figure 10. Division of Liner Mass into Jet and Slug.

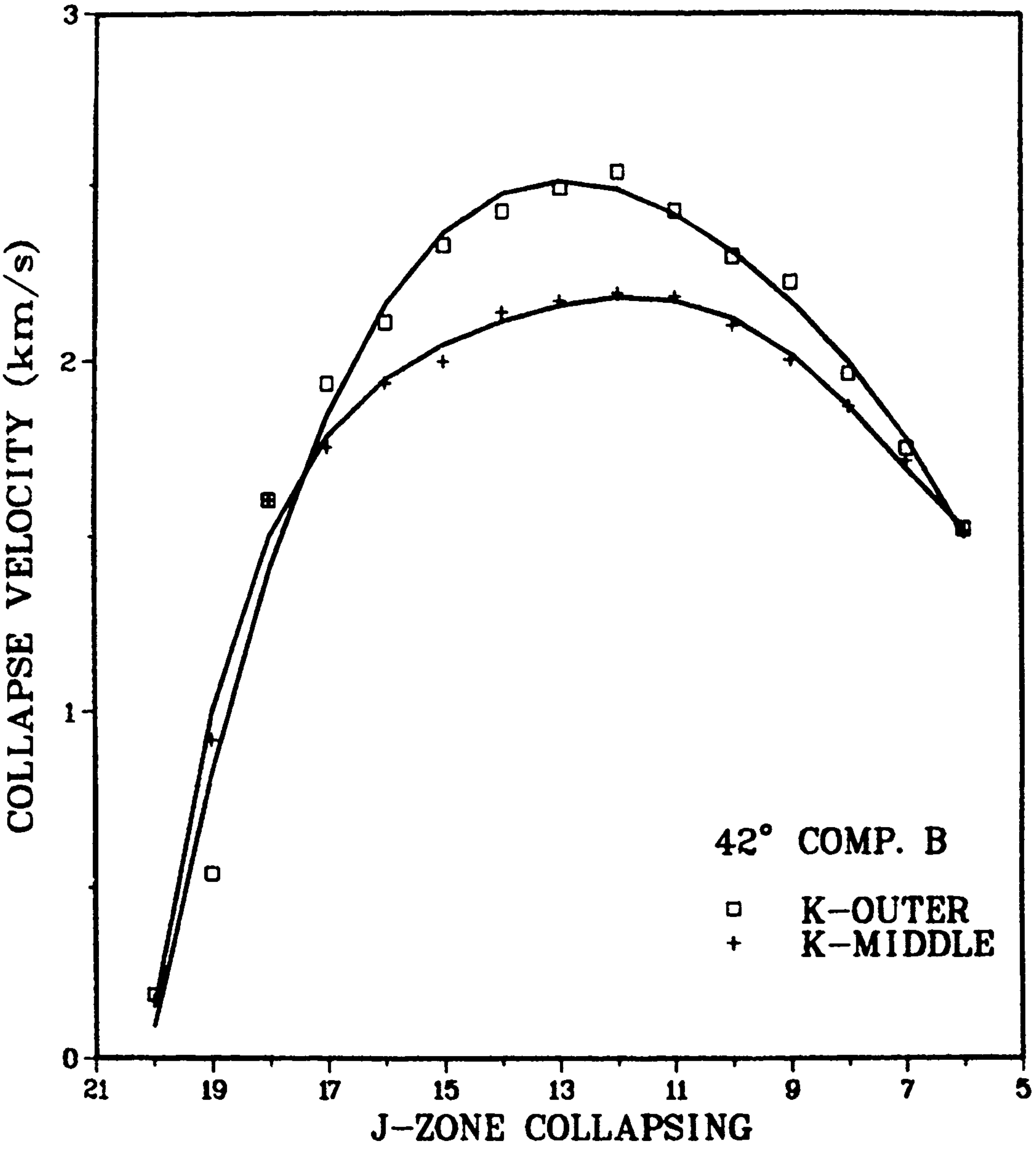

Figure 11. Collapse Velocities Calculated for the 42°, Comp. B Charge Modelled with the Basic HEMP Configuration.

It is important to note that even though a velocity gradient across the liner thickness has been calculated by the HEMP code, the jet formation equations derived by Birkhoff et al.,[5] and used in this report assumed the collapse process occurred within a constant velocity coordinate system. The smoothed collapse velocity values along the K-middle line, an approximate average between the K-outer and K-inner lines, were used in determining the final jet velocities.

The mass of each liner segment designated in the initial grid is printed in the problem set-up portion of the HEMP output. Liner mass calculations were broken down into those regions between each J line. The mass of each region was found by adding the segment masses on either side of the K-middle line and multiplying this result by π since the problem is two-dimensional axisymmetric. The total mass of the liner is equal to the sum of these regions. Because momentum is conserved, the liner mass of each segment may be expressed as:

$$M_L = M_j + M_s \,, \qquad (4)$$

where M_L is the liner mass of the segment and M_j and M_s are the segment's jet and slug masses respectively.[5] For no velocity gradient across the liner, the amount of liner mass in a given region that flows into either jet or slug mass can be solved by the equations:[5]

$$M_j = \frac{M_L}{2}\left(1 - \cos\beta\right) \text{ and} \qquad (5)$$

$$M_s = \frac{M_L}{2}\left(1 + \cos\beta\right). \qquad (6)$$

The difference between the mass division occurring in a liner without a velocity gradient through its thickness and in a liner with such a gradient depends upon the strength or intensity of the gradient. In an analysis made by Dr. Miles Lampson of BRL using the shaped charges modelled with HEMP for this study, the observed gradients were small enough that the error in the mass division was only a few percent; that is, the jet tip mass was overestimated by using the Birkhoff, MacDougall, Pugh and Taylor equations[5] by less than 10%.[8]

At this point, the classical jet formation equations may be applied. Let $\vec{V}_o^{\,\text{Final}}$ denote the smoothed collapse velocity of each liner segment along the K-middle line used in calculating the final jet velocity. Knowing the direction of collapse, θ, new collapse velocity components may be solved using the following relationships:

$$\left|\vec{V}_{o_Z}^{\,\text{Final}}\right| = \left|\vec{V}_{o}^{\,\text{Final}}\right| \sin\theta , \tag{7}$$

where $\left|\vec{V}_{o_Z}^{\,\text{Final}}\right|$ is the axial component of $\left|\vec{V}_{o}^{\,\text{Final}}\right|$ and

$$\left|\vec{V}_{o_R}^{\,\text{Final}}\right| = \left|\vec{V}_{o}^{\,\text{Final}}\right| \cos\theta , \tag{8}$$

where $\left|\vec{V}_{o_R}^{\,\text{Final}}\right|$ is the radial component of $\left|\vec{V}_{o}^{\,\text{Final}}\right|$. This trigonometric relationship between collapse velocities and their axial and radial components was previously illustrated in Figure 9. New axial and radial velocities were calculated for each liner segment along the K-middle line.

The final collapse velocity vector may also be expressed as a function of flow velocity and stagnation point velocity.[9] Flow velocity, $\vec{V}_f$, is the velocity of the liner segments flowing towards the stagnation point. Stagnation point velocity, $\vec{V}_{sp}$, is the velocity of a coordinate system at the stagnation point relative to a laboratory reference point. The final collapse velocity vector is equal to the vector addition of the flow and

---

[8] *Miles L. Lampson, "The Influence of Convergence - Velocity Gradients on the Formation of Shaped-Charge Jets," BRL Report in preparation.*

[9] *John T. Harrison, "Improved Analytical Shaped Charge Code: BASC," ARBRL-TR-02300, March 1981.*

stagnation point velocities and may be expressed as:

$$\vec{V}_o^{\,\text{Final}} = \vec{V}_f + \vec{V}_{sp}. \tag{9}$$

This relationship is illustrated in Figure 12.

The flow velocity for a given liner segment may be calculated by the following equation:

$$|\vec{V}_f| = \frac{|\vec{V}_{o_R}^{\,\text{Final}}|}{\sin\beta}, \tag{10}$$

where β is the angle between the collapsing liner segment and the cone axis. The angle between the flow velocity vector and the cone axis is identically equal to β for each liner segment. When a liner segment collapses towards the stagnation point, its associated velocity is divided equally into jet and slug velocities. The flow velocity calculated using equation 10 represents the velocity a segment contributes towards the jet. The negative of the flow velocity calculated with equation 10 represents the velocity contributed towards the slug.

The stagnation point velocity was calculated using:

$$|\vec{V}_{sp}| = |\vec{V}_f|\cos\beta + |\vec{V}_{o_Z}^{\,\text{Final}}| . \tag{11}$$

The stagnation point velocity adds the velocity of the entire coordinate system moving in the direction of the jet to the axial component of the final collapse velocity vector for each liner segment.

The final jet velocity as predicted via HEMP calculations and the theory of Birkhoff, MacDougall, Pugh and Taylor[5] can now be expressed in terms of flow and stagnation point velocities by the relationship[5]:

$$|\vec{V}_j| = |\vec{V}_f| + |\vec{V}_{sp}|, \tag{12}$$

where $|\vec{V}_j|$ is the jet velocity contribution from each liner segment. Similarly, the velocity of the slug may be given by:[5]

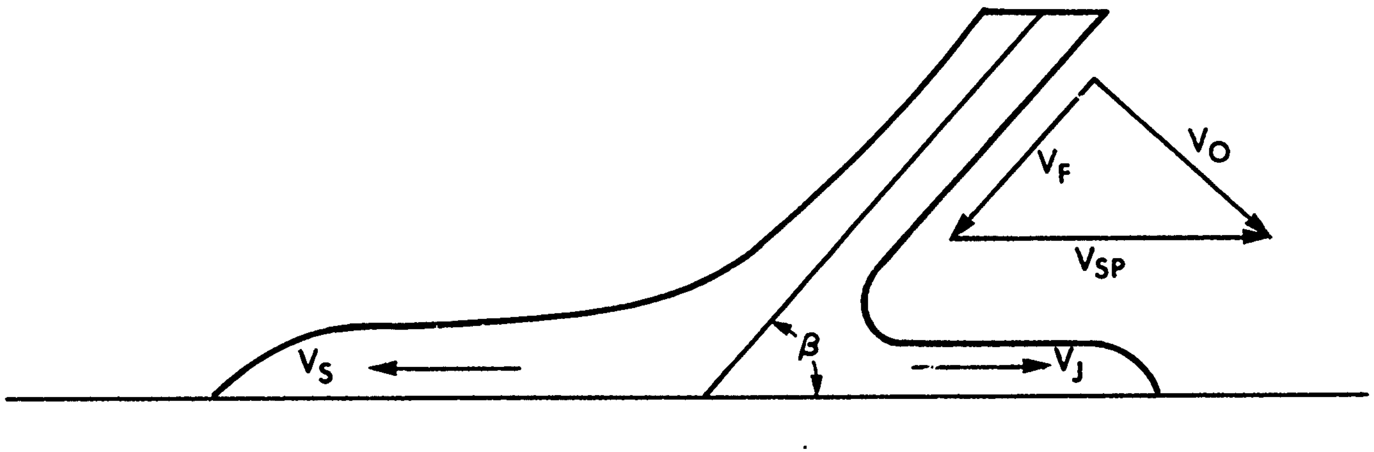

Figure 12. Relationship of the Collapse Velocity Vector, $\vec{V}_o$, to the Flow Velocity Vector, $\vec{V}_f$, and the Stagnation Point Velocity Vector, $\vec{V}_{sp}$.

$$|\vec{V}_s| = -|\vec{V}_f| + |\vec{V}_{sp}|, \tag{13}$$

where $\left|\vec{V}_s\right|$ is the slug velocity contribution from each liner segment.

The jet tip velocity, V_j^o, was calculated by weighting the liner segments' jet velocities with their respective jet masses in the direction from liner apex to base. The equation used was:

$$V_j^o = \frac{\Sigma M_j V_j}{\Sigma M_j} \quad \text{with} \quad V_j^o \leq V_j. \tag{14}$$

This averaging was carried out only under the condition that the trailing jet elements overtook the jet tip as it formed. The jet velocities calculated for the individual liner segments gradually increased for those segments from the apex to approximately one-third the distance down the liner. At this point, a maximum jet velocity was attained, and for the remainder of the segments approaching the liner base, the jet velocities gradually decreased. Using equation 14, the jet tip velocity calculated for the individual liner segments also gradually increased reaching a maximum value two to three liner segments farther down the liner than the point where the maximum jet velocity value was attained. The jet tip velocity was equal to the maximum mass weighted velocity. The jet tip mass was equal to the summation of the individual jet masses from those liner segments forming the jet tip (i.e., those segments from the apex to the segment having the maximum mass-weighted velocity inclusively). The associated jet velocities and masses of the remaining liner segments represent the trailing jet elements. Both velocity and mass are dependent on the collapse angle β, which has an associated error of $\pm 0.5^o$. Applying the upper and lower estimates for β into the jet formation equations for the 42^o Comp. B, basic configuration charge resulted in a change of the jet tip and jet element velocities of approximately $\pm$ 0.05km/s.

A previous note indicated that not all liner segments could be collapsed into the jetting process using the HEMP code. Approximately one-fifth of the total number of liner segments had collapse times later than the run time capability of HEMP. These segments, located towards the base of the liner, are the last segments to collapse and hence, comprise the rear, slower-moving portion of the jet. Jet characteristics can still be obtained for these segments based on earlier output from HEMP and the assumption that the detonation velocity of the explosive is constant throughout the collapse of the entire liner. The assumption of a "frozen in" velocity distribution is dependent on another assumption, that at late times, the pressure accelerating the liner is negligible. This implies that the axial and radial velocity components of these segments collapsing at late times may be assumed to equal previously computed values.

At the collapse time of the last liner segment that could be collapsed normally with HEMP, the grid locations and the axial and radial velocities of those segments not yet collapsed were recorded along the K-outer and K-middle lines. This data was taken directly from the output generated at the corresponding edit cycle. The recorded velocity values were assumed to remain constant until that segment reached the collapse phase. Since the location of each liner segment is known, as is its velocity towards the cone axis, the collapse time could be solved if the segment's location at the time of collapse was also known. An attempt was made to define the distance above the cone axis where liner separation into jet or slug occurs. This distance, δ, between the "shoulder" of the liner as it becomes jet and the cone axis was measured from the plots generated at late edit times when the region of liner division is more evident. The stagnation region was assumed to be the same height for all of the uncollapsed liner segments. Measurement of δ using the basic HEMP configuration for the 42°, Comp. B-loaded charge is shown in Figure 13. The collapse time for each remaining segment can be solved using:

$$T = \frac{Y(R) - \delta}{V_{o_R}} + t, \qquad (15)$$

where T is the collapse time of the segment in question, Y(R) is the distance of the segment above the cone axis, V_{o_R} is the velocity in the radial direction, and t is the collapse time of the last segment that was collapsed normally by HEMP. Collapse times for the one or two segments at the extreme base of the liner were on the order of hundreds of microseconds. This was considered to be too late in time for the segment to become an integral part of the jet, thus, these segments were not considered in further calculations.

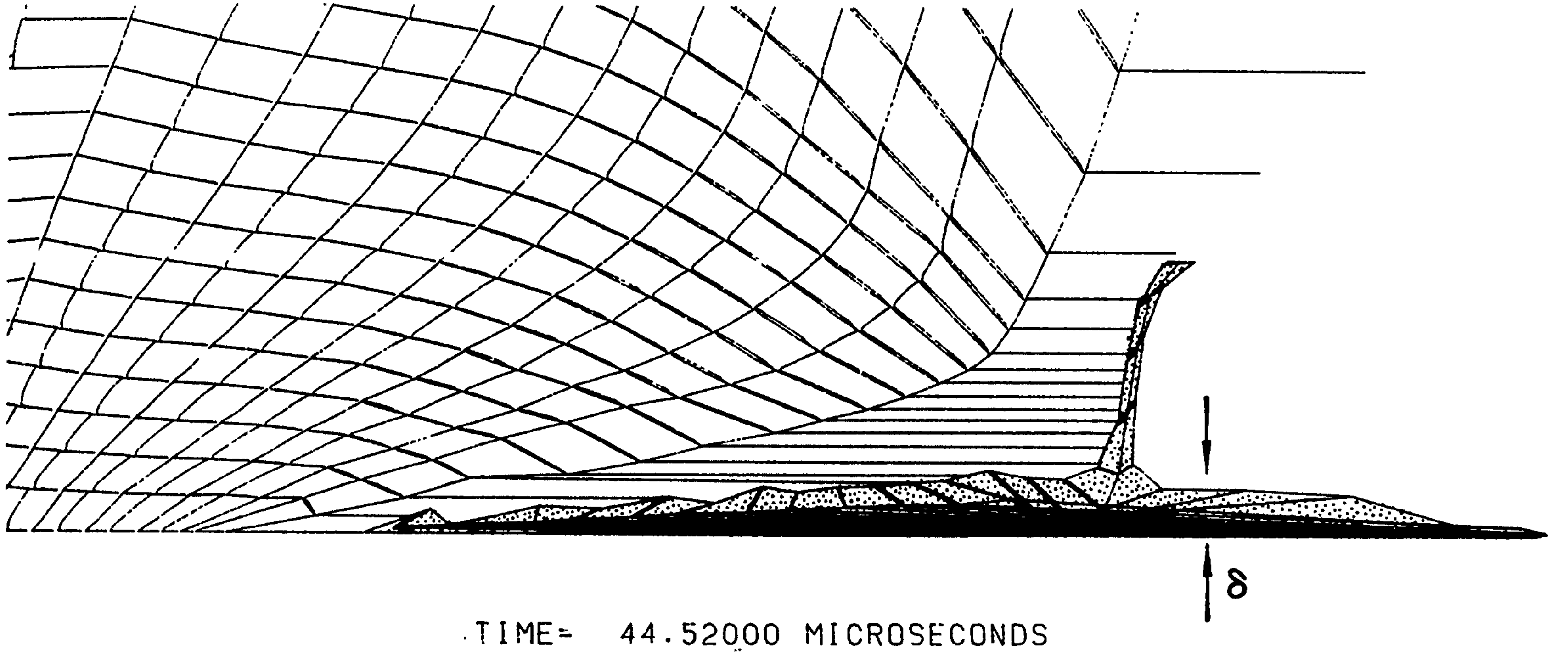

Figure 13. Measurement of the Distance Between the Stagnation Point and the Axis of Symmetry, δ.

New grid locations at the time of collapse may be calculated for each of the remaining liner segments using:

$$x(Z)' = x(Z) + V_{o_Z} \Delta t \qquad \text{and} \tag{16}$$

$$Y(R)' = Y(R) - V_{o_R} \Delta t , \tag{17}$$

where X(Z)' and Y(R)' are the coordinates of the node points surrounding the segment at its time of collapse, X(Z) and Y(R) are these same coordinates at the collapse time of the last segment collapse normally by HEMP, V_{o_Z} and V_{o_R} are the axial and radial velocities at the collapse time of the last segment collapsed normally by HEMP, and Δt is the time difference between the two collapse times. Equations 16 and 17 were used along the J-lines above and beneath each segment. The collapse angle, β, for these segments could therefore be solved by:

$$\beta = \tan^{-1} \left(\frac{\Delta Y(R)'}{\Delta x(Z)'} \right) + 180°, \tag{18}$$

where $\Delta X(Z)'$ and $\Delta Y(R)'$ are the differences in the axial and radial positions respectively, between the J-lines at the collapse time of the segment.

Having solved for the variables otherwise calculated by HEMP, the collapse velocity, direction of collapse, mass, and jet velocity calculations were solved using equations 1-13 in the manner previously described. At this point a one-to-one mapping may be done showing the liner segments' original positions in the HEMP grid versus the segments' relative velocity position in the jet. This is illustrated in Figure 14 for the 42°, Comp. B-loaded charge modelled with the basic HEMP configuration. Appendix A summarizes the jet characteristics obtained using the equations presented herein and output from HEMP for the shaped-charge configurations shown in Figures 3 and 4. Slug characteristics were not calculated in this study.

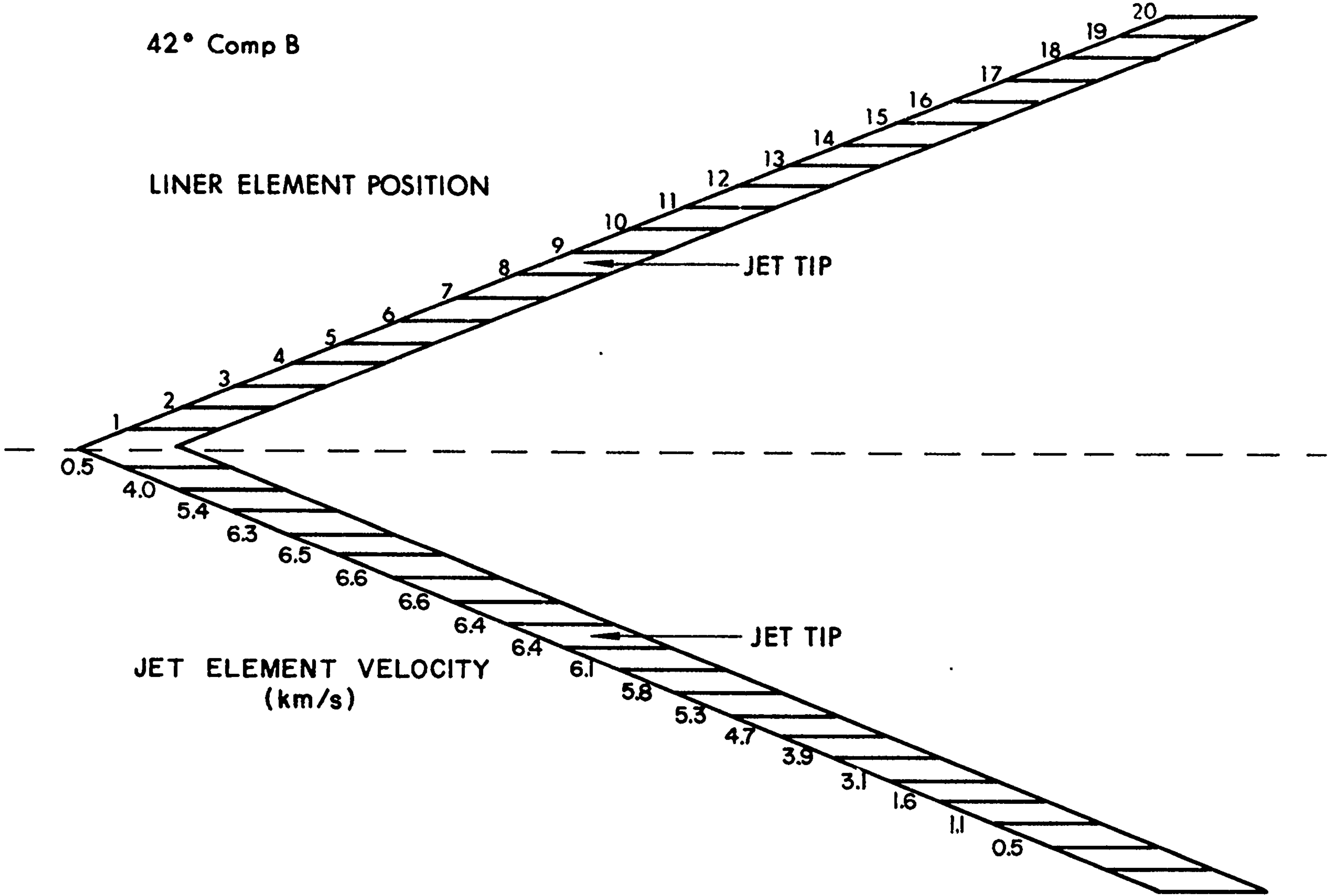

Figure 14. Mapping of the Liner Segments' Original Positions in the HEMP Grid Versus their Relative Positions in the Jet for the 42°, Comp. B Charge Modelled with the Basic Configuration.

IV. ALTERNATE GRID SCHEMES

In addition to the basic HEMP configurations shown previously in Figures 3 and 4, four other grid schemes were used to model the experimental charges. The intent of these alternate grid schemes was to determine if relatively small changes to the original grid could result in better agreement with the experimental data.

Of particular interest was the apex region of the liner in the 42° experimental charges. As shown in Figure 1, this region is curved and not straight, as originally modelled. Two different zoning configurations were used to model the 42° charges having curved apex regions. The first of these configurations, shown in Figure 15, had identical zoning to the original modelled charge except for the liner apex where the region of curvature was inputted as individual coordinates. This configuration was modelled using both Comp. B and Octol explosives. The second configuration, shown in Figure 16, used a polar coordinate system to generate the curved region and required rezoning throughout the explosive and the liner. This configuration was modelled using Comp. B explosive only. There was no attempt to model a curved apex for the 60° experimental charge. As illustrated in Figure 2, the radius of curvature at the liner apex is small enough so that the straight liner wall originally modelled remains a good approximation.

The other grid schemes modelled using HEMP were duplicates of the original configurations except the number of zones in the grids was doubled. The double-zoning was done for both the 42° and the 60° modelled charges and was analyzed using Comp. B explosive only. These configurations are illustrated in Figures 17 and 18 respectively. Unfortunately, doubling the number of zones in both the 42° and 60° models proved to be too fine a grid structure for the HEMP code to run effectively without rezoning. Early in the problem, the double-zoned grids became distorted to a greater extent than that observed for the original grids. The run times of HEMP were substantially shortened for the double-zoned problems. In the case of the double-zoned 42° model, the run time of HEMP was long enough that only the jet tip and a few trailing segments could be formed using the equations of Birkhoff et al.[5] For the 60° model, the HEMP run time was too short to allow more than a jet tip to be formed. A summary of the jet characteristics obtained for each of these alternate grid schemes is presented in Appendix B. No liner segments were collapsed based on the constant detonation velocity assumption.

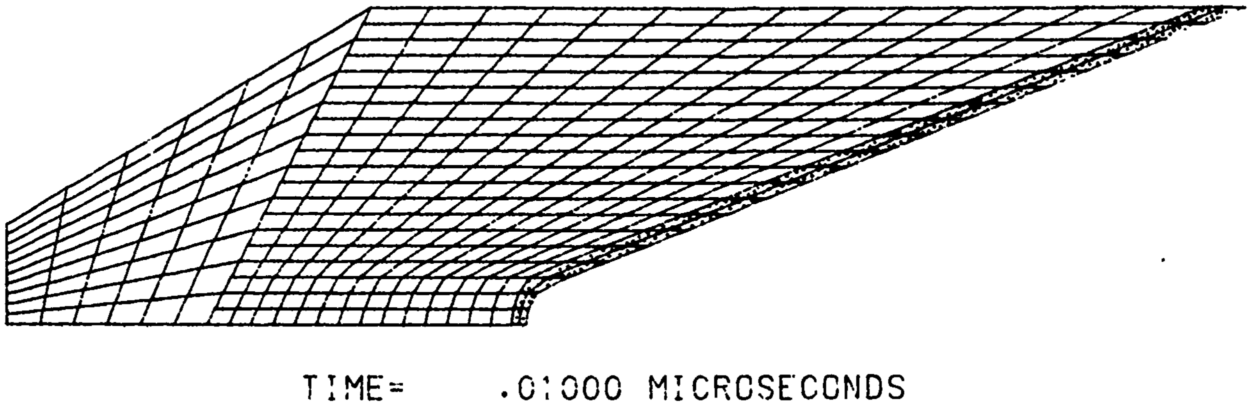

Figure 15. 42° Curved Apex Configuration.

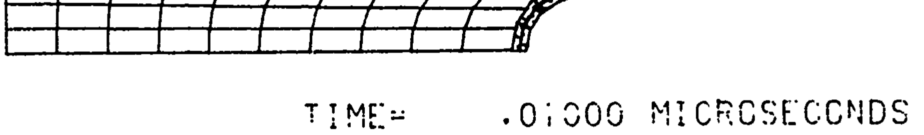

Figure 16. 42° Curved Apex Configuration, Polar Zoning.

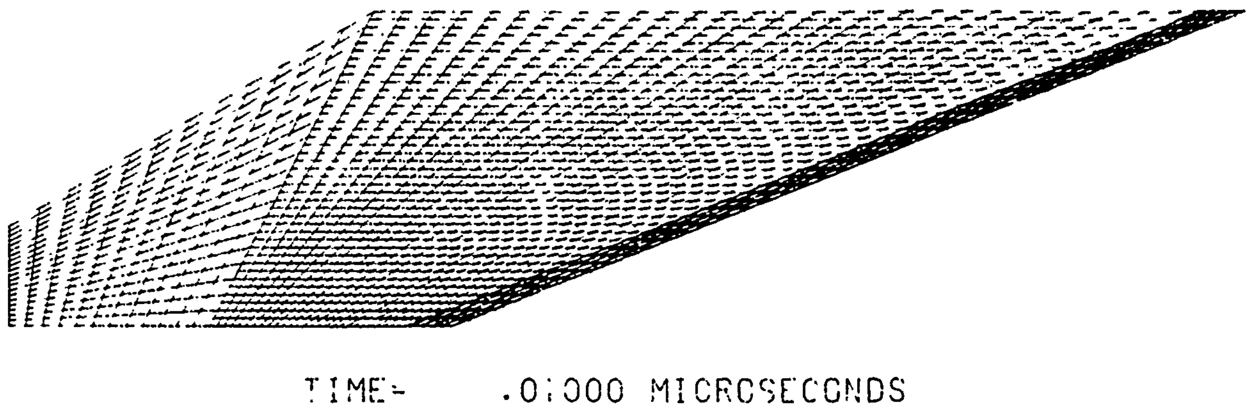

Figure 17. 42° Double-Zoning Configuration.

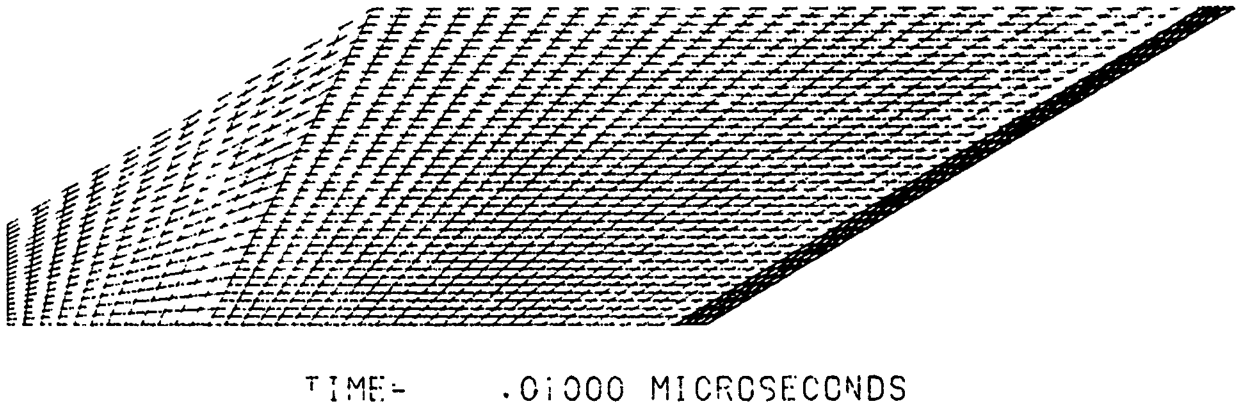

Figure 18. 60° Double-Zoning Configuration.

V. COMPARISON WITH EXPERIMENTAL DATA

The shaped-charge collapse process, as modelled with the HEMP code, was compared to radiographs of an 81mm, 42°, Comp. B-loaded charge at various stages of collapse from a test conducted by Mr. Stanley Golaski at BRL. The radiographs were compared to the plots generated at each edit cycle of the HEMP output for the basic 42° charge configuration illustrated in Figure 3. The measurements recorded were the collapse angles along the inside and outside surfaces of the liner wall, β^{in} and β^{out} respectively, and the distance, D, from the stagnation point to the rear of the slug. The position of the stagnation point (a common reference point between the radiographs and the plots) was defined to be the intersection of the lines extended through the center of the uncollapsed portion of the liner wall and along the axis of symmetry.

The radiographs of the collapse process were taken at delay times of 25, 31, and 37 microseconds following detonation of the charge. The strategy used in comparing the radiographs to the HEMP plots was to locate the plot having identical inner and outer collapse angles as the radiograph taken at the earliest delay time. The plot generated at 15.5 microseconds matched these requirements. Since the time interval between radiographs was six microseconds, the interval between the corresponding plots was kept equal to six microseconds. Therefore, the HEMP plots generated at 15.5, 21.5 and 27.5 microseconds corresponded to the radiographs taken at the specified delay times. The first two radiographs of this sequence are shown in Figures 19 and 20; the corresponding HEMP plots are shown in Figures 21 and 22.

Notice that the time differential between the radiographs and the HEMP plots is 9.5 microseconds at all three delay times. This difference may be accounted for, realizing that with the test charge, time zero occurred as an electrical current was passed to a detonator/booster assembly required to ensure detonation of the explosive. In the HEMP model, this assembly was not included and time zero occurred when the explosive was detonated. During the 12 microsecond time span studied, the inner and outer collapse angles measured from the HEMP plots remained in close agreement with those values measured from the radiographs. A discrepancy did exist between the plots and the radiographs regarding the distance from the stagnation point to the rear of the slug. At each of the first two comparative times, the HEMP plots indicated this distance, D, to be 6mm longer than the distance measured from the radiographs. Although this is an over-estimation by the HEMP code of the actual slug length, the difference between the

Figure 19. X-Ray of the Collapse Sequence of a 42°, Comp. B Charge 25 Microseconds after Detonation.

Figure 20. X-Ray of the Collapse Sequence of a 42°, Comp. B Charge 31 Microseconds after Detonation.

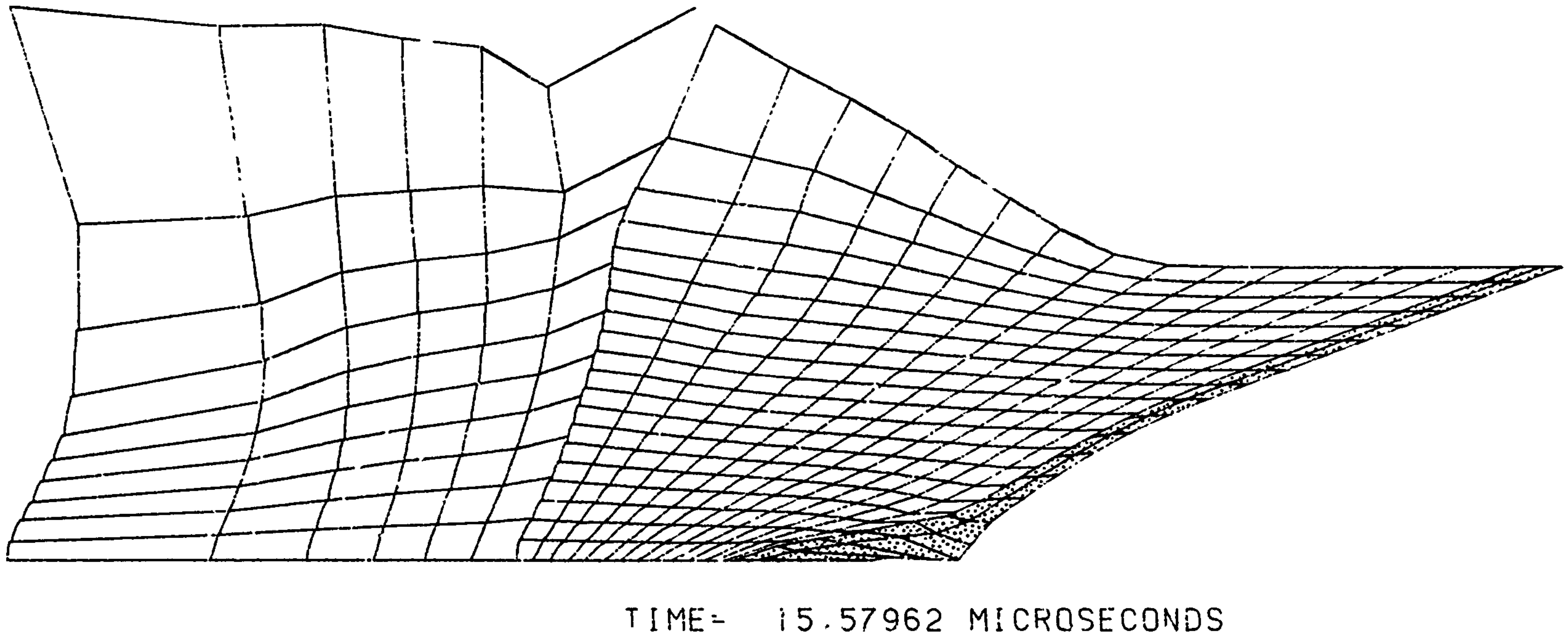

Figure 21. HEMP Calculation of the Collapse Process at 15.5 Microseconds Matching that Observed in Figure 19.

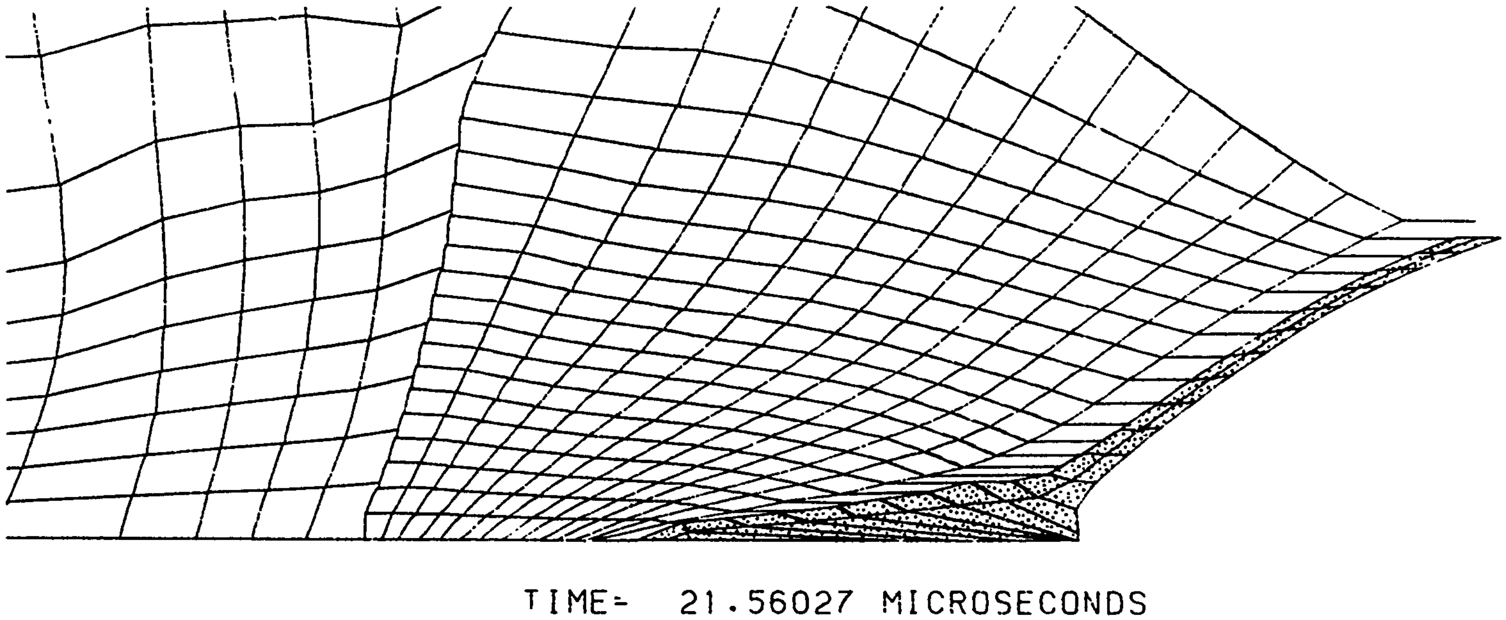

Figure 22. HEMP Calculation of the Collapse Process at 21.5 Microseconds Matching that Observed in Figure 20.

plot and radiograph measurements did not change. By the third comparative time, this over-estimation of the slug length had increased to 18mm. A possible explanation for this discrepancy is that since HEMP is a Lagrangian code, it cannot properly form a jet and in an effort to conserve momentum, redistributes both mass and velocity in the direction of the slug. This is reflected on the plots generated by HEMP, especially at late edit times when most of the liner has collapsed. This is not reflected on any of the jet characteristics derived from the equations presented in this report. The slug length may also be affected by the way the apex is modelled. When a straight apex liner collapses (as in this comparison), jetting immediately begins, creating a slug with a low velocity tail. A rounded apex, however, would be pushed forward as it begins collapsing, thereby reducing the overall slug length. A noticeable difference was observed on the plots at the same edit times between the lengths of the slugs from the two differently modelled apexes. A comparative table between the HEMP plots and the radiographs is presented in Table 1.

There was another type of comparison made to determine the accuracy of the HEMP code simulations. The jet characteristics obtained using output from HEMP and the theory of Birkhoff et al.,[5] were compared to the jet characteristics observed on radiographs of experimental shaped-charge jets in flight. All data reduced from the radiographs was obtained using the Jojet computer program,[10] which calculates velocity, mass, and related properties for each observed jet particle. Velocity data from the Jojet program is relatively accurate; the measurements taken are simply the jet particles' change in position with time. The mass data is less accurate, especially for irregularly shaped particles whose appearance may change drastically when viewed from a different angle.

The radiographs of the experimental charges were provided by Mr. Julius Simon and Mr. Wilbur Jones from separate tests conducted at BRL during the 1960's. The experimental charges used in both tests had copper liners with 84mm cone diameters and included both 42° and 60° apex angles. The charges were loaded with Comp. B and Octol explosive for the different liners tested. In Simon's experiment, the shaped charges were fired while rotating at speeds of 0, 15, 20, 30, 45, and 60 revolutions per second (rps). A radiograph from this test of a 42°, Comp. B-loaded charge fired at the 0rps spin rate is shown in Figure 23. Data is presented only for those charges that had rotational velocities less than or equal to 30rps. The collapse process is

---

[10] *H. Blische, B. Simmons, "A Method for Reducing Data from Radiographs of Shaped Charge Jets," ARBRL-TR-02330, June 1981. AD# 102 770.*

TABLE 1.

COLLAPSE SEQUENCE FOR A 42° COMP. B CHARGE - X-RAY OBSERVATIONS VS. HEMP CALCULATIONS

	Elapsed Time	Collapse Angle	D*
1) X-Rays	25.0μs	$\beta^{in} = 35^\circ$, $\beta^{out} = 32^\circ$	20mm
HEMP	15.5μs	$\beta^{in} = 35^\circ$, $\beta^{out} = 32^\circ$	26mm
2) X-Rays	31.0μs	$\beta^{in} = 42^\circ$, $\beta^{out} = 39^\circ$	44mm
HEMP	21.5μs	$\beta^{in} = 42^\circ$, $\beta^{out} = 36^\circ$	50mm
3) X-Rays	37.0μs	$\beta^{in} = 53^\circ$, $\beta^{out} = 49^\circ$	58mm
HEMP	27.5μs	$\beta^{in} = 54^\circ$, $\beta^{out} = 47^\circ$	76mm

$\Delta t = 9.5\mu s$

*D is the distance from the stagnation point to the rear of the slug.

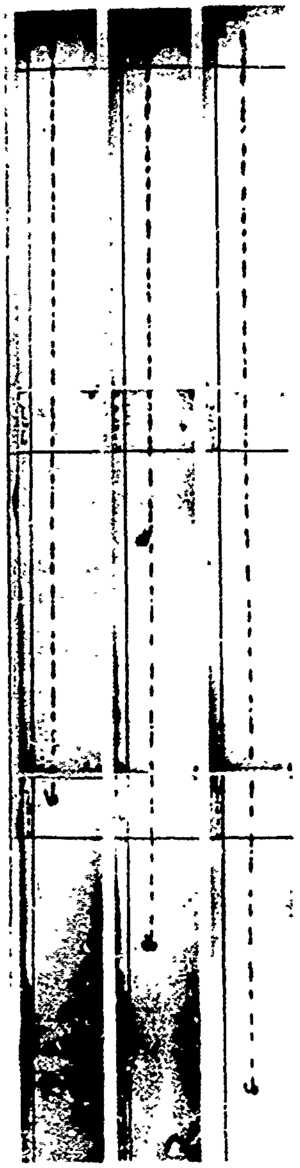

Figure 23. Radiograph of a 42°, Comp. B Charge Fired at Orps.

relatively unaffected at these low spin rates as evidenced by the apparent reproducibility of the jet velocity/mass distributions observed from the radiographs. As the spin increases, the break-up time for the jet is shortened and particles are split radially into chunks or fragments. The cut-off value of 30rps was chosen because at the higher rotational velocities, data reduction was virtually impossible due to the large number of fragments observed on the radiographs. All of the charges fired in the test performed by Jones were non-rotated.

The velocity/mass distribution of the experimental charges can be plotted against the distributions calculated using the HEMP code. The distribution for the 42°, Comp. B-loaded charge from the non-rotated test is compared in Figure 24 to the distribution calculated using HEMP for the basic grid configuration. The symbols plotted represent the individual jet particles observed on the radiographs. Different symbols imply similar shaped charges fired within the same test. The mass position plotted for each jet particle is the summation of the masses of all particles travelling at faster velocities. The solid line is the velocity/mass distribution of the liner segments as calculated using HEMP, while the dotted line is the extension to this distribution based on the assumption of a "frozen in" detonation velocity. Appendix C contains the velocity/mass plots comparing the distributions obtained using the HEMP code for all the grid schemes and the distributions reduced from radiographs from the test involving the rotated shaped charges. Appendix D compares these same distributions calculated using HEMP with the observed distributions from the test involving the non-rotated charges.

In general, the trend observed for the velocity/mass distribution comparisons indicates that the HEMP code input to the jet formation equations predicts a lower jet tip velocity and a larger tip mass than that observed experimentally. This trend is more obvious for the charges modelled with Octol explosive, and this discrepancy may be due to the equation-of-state accuracy inputted for the particular problem. The jet formation equations used to determine the jet velocity assumed no velocity gradient existed within the liner. Thus, the collapse velocity values, taken as an average over the liner thickness, are lower than those values for the inner section which produces the jet. These lower values are reflected in the final jet velocity calculations. The over-prediction of the jet tip mass may not be quite as severe as first expected. The experimental mass values, against which the HEMP values are plotted, have error inherently associated with them. As previously mentioned, the mass values obtained from data reduction of radiographs are relatively

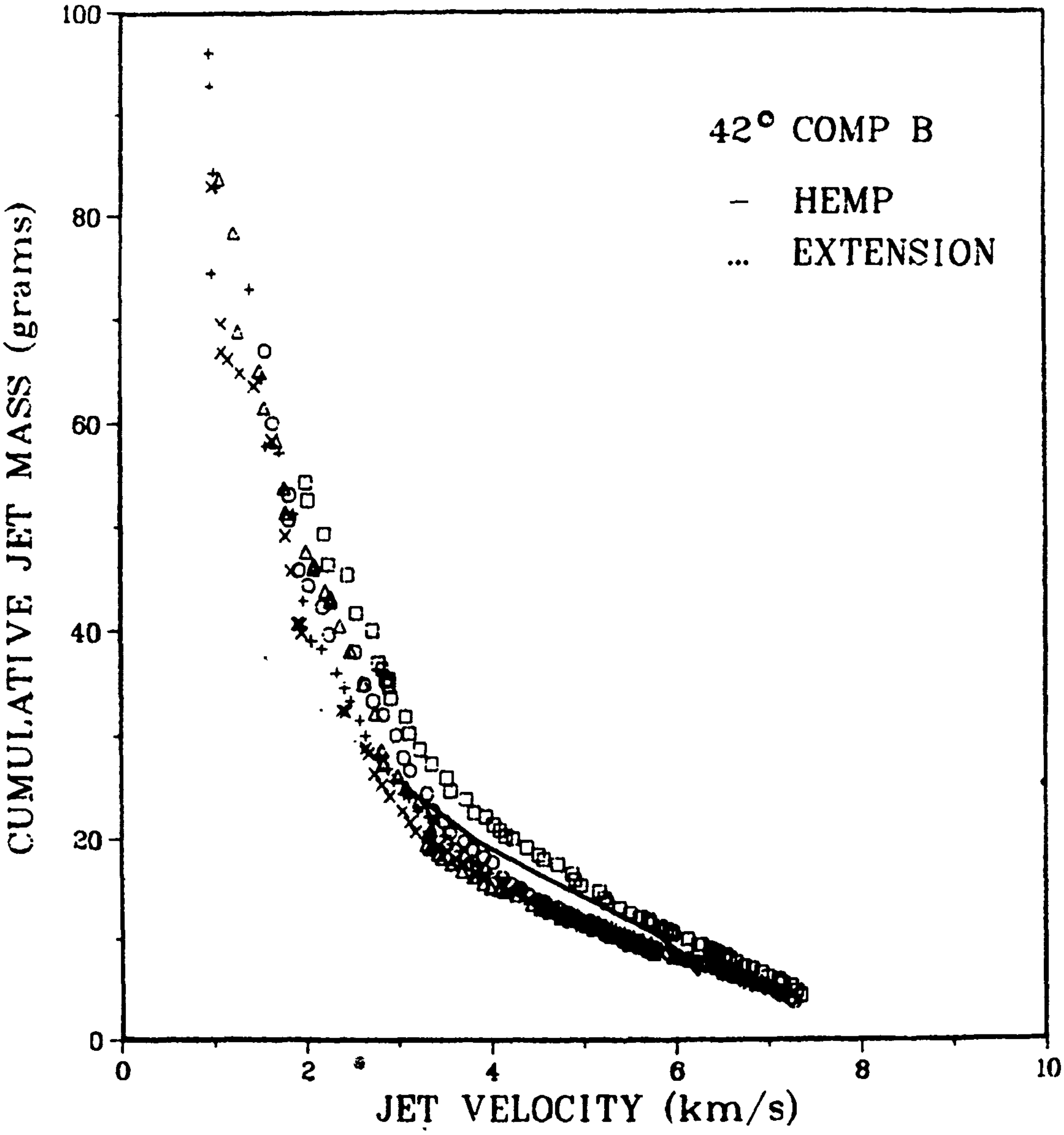

Figure 24. Comparison of the Velocity/Mass Distribution Calculated by HEMP using the Basic Configuration and the Data Observed Radiographically for the Non-Rotated 42°, Comp. B Charges.

inaccurate. Jet tip masses may also appear less on a radiograph if a portion of the total tip mass has been eroded during flight. Short-time radiographs of the jets from the rotated rounds indicate that jet tip ablation often occurs. Variations of the jet tip masses were quite evident among the experimental charges used in both tests. In the test involving the non-rotated charges, two of the 60°, Octol-loaded rounds were observed to have tip masses of 3.40 grams and 7.14 grams. This represents a 210% difference between two similar charges.

Beyond the jet tip region, the characteristics obtained using HEMP for those liner segments comprising the trailing jet show reasonable agreement with the experimental data. Both velocity and mass, as calculated for these segments, follow the distribution pattern exhibited by the individual jet particles observed radiographically in both tests. On the plots contained in Appendices C and D, this is shown by the relative slopes of the predicted distributions and the distributions of the experimental jet particles. The calculated velocity/mass distributions may be divided into linear sections with different slopes. At most, three linear sections were observed for the modelled charge configurations having long HEMP run times and utilizing the extension process based on the constant detonation velocity assumption (Figure 24 is one such example). In most cases, the first linear section containing the jet tip and the higher velocity liner segments had a slope nearly matching that of the respective jet particles. The slope of the second linear section containing the intermediate velocity segments tended to be less than that observed for the corresponding jet particles. The third linear section representing the massive, slow, rear of the jet has a slope very close to that of the jet particles for those rounds whose radiographs showed these slow-moving particles. The round-to-round variability within the experimental data must be assessed before the accuracy of the velocity/mass distributions calculated using HEMP can be determined.

VI. SUMMARY

A method has been presented to determine shape-charge jet characteristics using the finite difference Lagrangian code HEMP and the jet formation equations of Birkhoff et al.[5] An extension to the HEMP code output based on the assumption of a constant detonation velocity has been included to demonstrate one method of collapsing the liner segments at the base of the liner where the collapse times are often greater than the run-time capability of HEMP. The HEMP code was used to model 42° and 60°, 81mm cone diameter charges with both Comp. B and Octol explosives for several different grid configurations.

The HEMP code is presented as a useful tool for modelling shaped-charge collapse and jet formation processes. A new feature incorporated into this study is an explicit rule for determining the "time of collapse" of a liner segment into the jet flow.

Data was reduced from radiographs of shaped charges tested at BRL during various stages of collapse and compared to the collapse process calculated using HEMP. Over a 12 microsecond time span, the collapse process simulated by HEMP showed close agreement with experiment regarding collapse angles; however, the length of the slug being formed was over-predicted. An experimental data base of velocity/mass distributions has been established and compared to the distributions predicted using HEMP. On average, for the configurations from which jet characteristics could be determined, jet tip velocity calculations were 18% less than that experimentally observed and jet tip mass calculations were 110% greater. This large error in the jet tip mass calculations is partially due to the data reduction technique used, jet tip ablation, and the variation in the experimental data between similar charges. The calculated characteristics for the trailing jet particles closely reflect the pattern of the trailing particles observed on the radiographs.

ACKNOWLEDGEMENT

The author is deeply indebted to Dr. Miles L. Lampson for his technical guidance throughout this project.

LIST OF REFERENCES

1. M.L. Wilkins, "Calculation of Elastic-Plastic Flow," UCRL-7322, January 1969.

2. R.R. Karpp, "Accuracy of HEMP Code Solutions," BRL-MR-2268, January 1973. AD# 757 153.

3. J.T. Harrison, R.R. Karpp, "Terminal Ballistic Application of Hydrodynamic Computer Code Calculations," BRL-R-1984, April 1977. AD# A041065.

4. J.T. Harrison, "A Comparison Between The Eulerian Hydrodynamic Computer Code (BRLSC), and Experimental Collapse of a Shaped Charge Liner," ARBRL-MR-02841, June 1978. AD# 059 711.

5. G. Birkhoff, D.P. MacDougall, E.M. Pugh, G. Taylor, "Explosives with Lined Cavities," Journal of Applied Physics, Vol. 19, No. 6, June 1948.

6. B.M. Dobratz, "LLNL Explosives Handbook, Properties of Chemical Explosives and Explosive Simulants," UCRL-52997, March 1981.

7. R.R. Karpp, $P(\mu) = 1.19\mu + 4.435\mu^2$.

8. Miles L. Lampson, "The Influence of Convergence - Velocity Gradients on the Formation of Shaped-Charge Jets," BRL Report in preparation.

9. John T. Harrison, "Improved Analytical Shaped Charge Code: BASC," ARBRL-TR-02300, March 1981.

10. H. Blische, B. Simmons, "A Method for Reducing Data from Radiographs of Shaped Charge Jets," ARBRL-TR-02330, June 1981. AD# 102 770.

LEGEND OF SYMBOLS
USED IN APPENDICES A AND B

T - Collapse time (μs) of the liner segment.

β - Collapse angle (degrees).

$\vec{V}_o$ - Collapse velocity vector (km/s) along the K-middle line as calculated by the HEMP code.

θ - Collapse direction (degrees - measured with respect to the radial collapse velocity vector) along the K-middle line.

M_j - Mass (grams) which becomes part of the jet upon collapse.

$\vec{V}_o^{\text{Final}}$ - Smoothed collapse velocity vector (km/s). This was the collapse velocity value used in the jet velocity calculations.

$\vec{V}_{o_Z}^{\text{Final}}$ - Axial collapse velocity component (km/s) of $\vec{V}_o^{\text{Final}}$.

$\vec{V}_{o_R}^{\text{Final}}$ - Radial collapse velocity component (km/s) of $\vec{V}_o^{\text{Final}}$.

$\vec{V}_f$ - Flow velocity vector (km/s) that contributes to the jet.

$\vec{V}_{sp}$ - Stagnation point velocity vector (km/s).

V_j - Jet velocity (km/s).

V_j^0 - Jet tip velocity (km/s); calculations were done for every liner segment beginning at the apex until a maximum value was reached.

APPENDIX A

JET CHARACTERISTICS DERIVED FROM THE BASIC HEMP CONFIGURATIONS

A-1. 42°, Comp. B Simulation
A-2. 42°, Octol Simulation
A-3. 60°, Comp. B Simulation
A-4. 60°, Octol Simulation

TABLE A-1

42° COMP. B SIMULATION

Liner Segment	T	β	$\vec{V}_o$	θ	M_j	$\vec{V}_o$ Final
apex1	8.5	22.0°	0.169	62.49°	.0774	0.152
2	10.0	28.0°	0.922	29.56°	.2073	0.997
3	12.0	31.0°	1.604	32.61°	.3541	1.498
4	13.5	32.0°	1.755	30.76°	.4843	1.784
5	15.0	34.0°	1.936	31.20°	.6661	1.946
6	16.5	35.0°	1.996	30.83°	.8327	2.043
7	18.0	36.0°	2.135	31.54°	1.0146	2.108
8	19.5	38.0°	2.167	32.47°	1.2764	2.153
9	21.0	39.0°	2.188	32.29°	1.4997	2.177
10	22.5	41.0°	2.179	31.85°	1.8244	2.170
11	24.0	42.0°	2.101	31.29°	2.0923	2.121
12	26.0	44.0°	2.003	32.21°	2.4850	2.022
13	27.5	47.0°	1.879	30.61°	3.0410	1.874
14	30.0	52.0°	1.717	31.39°	3.9476	1.696
15	33.0	60.0°	1.516	31.95°	5.4896	1.526
16*	48.6	92.6°	1.141	29.94°	12.2178	1.174
17*	65.2	92.7°	0.874	32.21°	12.9800	0.836
18*	116.0	111.6°	0.473	31.42°	17.9287	0.491

*These segments were collapsed using the constant detonation velocity assumption. δ = 7.0mm

TABLE A-1

42^{c} COMP. B SIMULATION

(Continuation)

Liner Segment	$\vec{V}_{o_Z}$ Final	$\vec{V}_{o_R}$ Final	$\vec{V}_f$	$\vec{V}_{sp}$	V_j	V_j^o
apex1	0.135	0.070	0.187	0.308	0.495	0.495
2	0.492	0.867	1.847	2.123	3.970	3.025
3	0.807	1.262	2.450	2.907	5.357	4.318
4	0.912	1.533	2.893	3.365	6.258	5.154
5	1.008	1.665	2.978	3.476	6.454	5.638
6	1.047	1.754	3.058	3.552	6.610	5.947
7	1.103	1.797	3.057	3.576	6.633	6.138
8	1.156	1.816	2.950	[illegible].480	6.430	6.214
9	1.163	1.840	2.924	3.435	6.359	6.248
10	1.145	1.843	2.809	3.265	6.074	
11	1.102	1.812	2.708	3.114	5.822	
12	1.078	1.711	2.463	2.850	5.313	
13	0.954	1.613	2.205	2.458	4.663	
14	0.883	1.448	1.838	2.014	3.852	
15	0.808	1.295	1.495	1.556	3.051	
16*	0.586	1.017	1.018	0.540	1.558	
17*	0.446	0.707	0.708	0.413	1.121	
18*	0.256	0.419	0.451	0.090	0.541	

TABLE A-2

42° OCTOL SIMULATION

Liner Segment	T	β	$\vec{V}_o$	θ	M_j	$\vec{V}_o$ Final
apex1	8.5	22.0°	0.373	63.81°	.0774	0.406
2	10.0	24.0°	1.361	30.02°	.1531	1.300
3	11.5	27.0°	1.797	33.25°	.2702	1.769
4	13.0	30.0°	1.945	32.29°	.4270	1.999
5	14.0	33.0°	2.067	30.40°	.6285	2.113
6	15.5	34.0°	2.163	31.31°	.7872	2.186
7	17.0	35.0°	2.313	32.36°	.9607	2.255
8	18.0	37.0°	2.361	31.12°	1.2124	2.323
9	19.5	38.0°	2.391	31.66°	1.4265	2.376
10	21.0	39.0°	2.382	31.80°	1.6575	2.392
11	22.5	41.0°	2.309	31.92°	1.9981	2.346
12	24.5	43.0°	2.176	33.59°	2.3787	2.228
13	26.0	46.0°	2.075	32.14°	2.9199	2.046
14	28.0	52.0°	1.895	31.93°	3.9476	1.841
15	30.5	59.0°	1.667	31.65°	5.3245	1.697
16*	44.4	91.5°	1.271	30.33°	11.9936	1.283
17*	59.7	96.7°	0.960	31.82°	13.8424	0.909
18*	109.3	111.2°	0.520	32.54°	17.8435	0.552

*These segments were collapsed using the constant detonation velocity assumption. δ =7.0mm.

TABLE A-2

42^{o} OCTOL SIMULATION

(Continuation)

Liner Segment	$\vec{V}_{o_Z}$ Final	$\vec{V}_{o_R}$ Final	$\vec{V}_f$	$\vec{V}_{sp}$	V_j	V_j^{o}
apex1	0.364	0.179	0.478	0.807	1.285	1.285
2	0.650	1.126	2.768	3.179	5.947	4.382
3	0.970	1.479	3.258	3.873	7.131	5.865
4	1.068	1.690	3.380	3.995	7.375	6.560
5	1.069	1.822	3.345	3.875	7.220	6.827
6	1.136	1.868	3.341	3.905	7.246	6.968
7	1.207	1.905	3.321	3.928	7.249	7.049
8	1.201	1.989	3.305	3.840	7.145	7.075
9	1.247	2.022	3.284	3.835	7.119	7.086
10	1.260	2.033	3.230	3.771	7.001	
11	1.240	1.991	3.035	3.530	6.565	
12	1.233	1.856	2.721	3.223	5.944	
13	1.088	1.732	2.408	2.761	5.169	
14	0.974	1.562	1.982	2.194	4.176	
15	0.890	1.445	1.686	1.758	3.444	
16*	0.648	1.107	1.107	0.619	1.726	
17*	0.479	0.772	0.777	0.388	1.165	
18*	0.297	0.465	0.499	0.117	0.616	

TABLE A-3

60° COMP. B SIMULATION

Liner Segment	T	β	$\vec{V}_o$	θ	M_j	$\vec{V}_o$ Final
apex1	13.5	32.0°	0.632	65.96°	.1154	0.662
2	14.5	34.0°	1.366	39.35°	.2164	1.317
3	16.0	40.0°	1.749	45.21°	.4146	1.696
4	17.0	41.0°	1.821	40.72°	.5589	1.913
5	18.0	43.0°	2.017	39.43°	.7481	2.045
6	19.0	44.0°	2.128	38.95°	.9237	2.136
7	20.5	45.0°	2.263	40.75°	1.1122	2.208
8	22.0	47.0°	2.307	42.42°	1.3786	2.263
9	23.0	49.0°	2.288	41.07°	1.6544	2.292
10	24.5	51.0°	2.259	41.48°	1.9706	2.282
11	26.0	54.0°	2.187	42.16°	2.4002	2.219
12	27.5	58.0°	2.089	41.93°	2.9752	2.100
13	29.0	62.0°	1.943	41.12°	3.6262	1.934
14	32.0	72.0°	1.793	43.33°	5.0729	1.753
15	35.0	83.0°	1.592	43.22°	6.8913	1.614
16*	51.4	110.3°	1.282	42.40°	11.2524	1.276
17*	68.9	115.0°	0.968	46.51°	12.6052	0.938
18*	119.0	131.9°	0.545	47.60°	15.6220	0.568

*These segments were collapsed using the constant detonation velocity assumption. δ =6.0mm.

TABLE A-3

60° COMP. B SIMULATION

(Continuation)

Liner Segment	$\vec{V}_{o_Z}$ Final	$\vec{V}_{o_R}$ Final	$\vec{V}_f$	$\vec{V}_{sp}$	V_j	V_j^o
apex1	0.605	0.270	0.510	1.037	1.547	1.547
2	0.835	1.018	1.820	2.344	4.164	3.254
3	1.204	1.195	1.859	2.628	4.487	3.939
4	1.248	1.450	2.210	2.916	5.126	4.447
5	1.299	1.580	2.317	2.993	5.310	4.761
6	1.343	1.661	2.391	3.063	5.454	4.976
7	1.441	1.673	2.366	3.114	5.480	5.113
8	1.527	1.671	2.285	3.085	5.370	5.178
9	1.506	1.728	2.290	3.008	5.298	5.206
10	1.512	1.710	2.260	2.897	5.097	
11	1.489	1.645	2.033	2.684	4.717	
12	1.403	1.562	1.842	2.379	4.221	
13	1.272	1.457	1.650	2.047	3.697	
14	1.203	1.275	1.341	1.617	2.958	
15	1.105	1.176	1.185	1.249	2.434	
16*	0.860	0.942	1.004	0.512	1.516	
17*	0.681	0.646	0.713	0.380	1.093	
18*	0.419	0.383	0.515	0.075	0.590	

TABLE A-4

60° OCTOL SIMULATION

Liner Segment	T	β	$\vec{V}_o$	θ	M_j	$\vec{V}_o$ Final
apex1	12.5	32.0°	0.606	64.89°	.1154	0.625
2	13.5	34.0°	1.421	39.01°	.2164	1.395
3	15.0	37.0°	1.889	44.89°	.3568	1.828
4	16.0	41.0°	1.973	40.99°	.5589	2.071
5	17.0	43.0°	2.202	40.32°	.7481	2.219
6	18.0	45.0°	2.341	39.97°	.9640	2.325
7	19.5	46.0°	2.456	42.34°	1.1595	2.412
8	20.5	47.0°	2.509	41.33°	1.3786	2.478
9	21.5	48.0°	2.485	41.13°	1.5915	2.510
10	23.0	51.0°	2.461	42.32°	1.9706	2.490
11	24.5	53.0°	2.396	43.12°	2.3185	2.409
12	25.5	57.0°	2.275	41.56°	2.8820	2.272
13	27.5	62.0°	2.146	42.72°	3.6262	2.110
14	29.5	69.0°	1.972	42.76°	4.7106	1.990
15*	38.7	97.5°	1.695	41.15°	8.8720	1.699
16*	46.2	106.6°	1.402	42.22°	10.7408	1.372
17*	62.5	117.0°	1.006	43.60°	12.8832	1.000
18*	105.6	123.4°	0.594	47.50°	14.5228	0.607

*These segments were collapsed using the constant detonation velocity assumption. δ = 7.0mm.

TABLE A-4

60° OCTOL SIMULATION

(Continuation)

Liner Segment	$\vec{V}_{o_Z}$ Final	$\vec{V}_{o_R}$ Final	$\vec{V}_f$	$\vec{V}_{sp}$	V_j	V_j^o
apex1	0.566	0.265	0.500	0.990	1.490	1.490
2	0.878	1.084	1.939	2.485	4.424	3.404
3	1.290	1.295	2.152	3.009	5.161	4.314
4	1.358	1.563	2.382	3.156	5.538	4.862
5	1.436	1.692	2.481	3.250	5.731	5.188
6	1.494	1.782	2.520	3.276	5.796	5.386
7	1.625	1.783	2.479	3.347	5.826	5.510
8	1.636	1.861	2.545	3.371	5.916	5.612
9	1.651	1.891	2.545	3.354	5.899	5.676
10	1.676	1.841	2.369	3.167	5.536	
11	1.647	1.758	2.201	2.972	5.173	
12	1.507	1.700	2.027	2.611	4.638	
13	1.431	1.550	1.755	2.255	4.010	
14	1.351	1.461	1.565	1.912	3.477	
15*	1.118	1.279	1.290	0.950	2.240	
16*	0.922	1.016	1.060	0.619	1.679	
17*	0.690	0.724	0.813	0.321	1.134	
18*	0.448	0.410	0.491	0.178	0.669	

APPENDIX B

JET CHARACTERISTICS DERIVED FROM THE ALTERNATE HEMP CONFIGURATIONS

B-1. 42° Curved Apex, Comp. B Simulation
B-2. 42° Curved Apex, Octol Simulation
B-3. 42° Curved Apex (Polar Zoning), Comp. B Simulation
B-4. 42° (Double-Zoning), Comp. B Simulation
B-5. 60° (Double-Zoning), Comp. B Simulation

TABLE B-1

42° CURVED APEX, COMP. B SIMULATION

Liner Segment*	T	β	$\vec{V}_o$	θ	M_j	$\vec{V}_o$ Final
apex3	12.5	50.0°	1.320	45.54°	.8516	1.316
4	13.5	25.0°	1.596	32.73°	.2987	1.615
5	15.0	30.0°	1.869	31.98°	.5218	1.842
6	16.5	33.0°	1.999	31.39°	.7430	2.005
7	18.0	34.0°	2.100	31.94°	.9079	2.112
8	19.5	35.0°	2.170	32.50°	1.0890	2.170
9	21.0	36.0°	2.183	32.47°	1.2849	2.185
10	22.5	38.0°	2.174	32.03°	1.5771	2.161
11	24.0	40.0°	2.101	31.51°	1.9053	2.102
12	26.0	42.0°	2.003	32.23°	2.2748	2.008
13	27.5	44.0°	1.877	30.60°	2.6833	1.880
14	30.0	55.0°	1.717	31.37°	3.6699	1.716
15	33.0	[illegible]°	1.514	31.91°	5.1599	1.510
16	38.5	73.0°	1.255	34.12°	8.2725	1.257

*Liner segments 1 and 2 do not collapse into the jetting process with this curved apex configuration.

TABLE B-1

42^o CURVED APEX, COMP. B SIMULATION

(Continuation)

Liner Segment	$\vec{V}_{o_Z}$ Final	$\vec{V}_{o_R}$ Final	$\vec{V}_f$	$\vec{V}_{sp}$	V_j	V_j^o
apex3	0.939	0.922	1.204	1.713	2.917	2.917
4	0.873	1.359	3.216	3.787	7.003	3.978
5	0.976	1.562	3.124	3.681	6.805	4.860
6	1.044	1.712	3.143	3.680	6.823	5.464
7	1.117	1.792	3.205	3.774	6.979	5.878
8	1.166	1.830	3.191	3.780	6.971	6.148
9	1.173	1.843	3.135	3.710	6.845	6.305
10	1.146	1.832	2.976	3.491	6.467	6.340
11	1.099	1.792	2.788	3.235	6.023	
12	1.071	1.699	2.539	2.958	5.497	
13	0.957	1.618	2.329	2.632	4.961	
14	0.893	1.465	1.912	2.122	4.034	
15	0.798	1.282	1.512	1.599	3.111	
16	0.705	1.041	1.089	1.023	2.112	

TABLE B-2

42° CURVED APEX, OCTOL SIMULATION

Liner Segment*	T	β	$\vec{V}_o$	θ	M_j	$\vec{V}_o$ Final
apex3	10.5	47.0°	1.068	43.36°	.7582	1.080
4	12.0	30.0°	1.655	29.56°	.4272	1.623
5	13.5	33.0°	1.946	29.73°	.6284	1.964
6	15.5	34.0°	2.168	31.78°	.7874	2.170
7	17.0	35.0°	2.271	32.89°	.9604	2.290
8	18.0	37.0°	2.363	31.45°	1.2125	2.354
9	19.5	38.0°	2.388	31.91°	1.4262	2.376
10	21.0	39.0°	2.378	31.85°	1.6579	2.363
11	22.5	42.0°	2.309	32.01°	2.0918	2.313
12	24.0	43.0°	2.200	31.45°	2.3793	2.219
13	26.0	46.0°	2.074	32.13°	2.9192	2.078
14	28.0	51.0°	1.894	31.90°	3.8082	1.888
15	30.5	57.0°	1.664	31.62°	4.9984	1.654
16	36.5	68.0°	1.386	34.98°	7.3112	1.392

*Liner segments 1 and 2 do not collapse into the jetting process with this curved apex configuration.

TABLE B-2

42^{o} CURVED APEX, OCTOL SIMULATION

(Continuation)

Liner Segment	$\vec{V}_{o_Z}$ Final	$\vec{V}_{o_R}$ Final	$\vec{V}_f$	$\vec{V}_{sp}$	V_j	V_j^o
apex3	0.742	0.785	1.073	1.474	2.547	2.547
4	0.801	1.412	2.824	3.247	6.071	3.817
5	0.974	1.705	3.131	3.599	6.730	4.826
6	1.143	1.845	3.299	3.878	7.177	5.538
7	1.244	1.923	3.353	3.990	7.343	6.025
8	1.228	2.008	3.337	3.893	7.230	6.331
9	1.256	2.017	3.276	3.838	7.114	6.511
10	1.247	2.007	3.189	3.725	6.914	6.596
11	1.226	1.961	2.931	3.404	6.335	
12	1.158	1.893	2.776	3.188	5.961	
13	1.105	1.760	2.447	2.805	5.252	
14	0.998	1.603	2.063	2.296	4.359	
15	0.867	1.408	1.679	1.781	3.460	
16	0.798	1.141	1.231	1.259	2.490	

TABLE B-3

42° CURVED APEX (POLAR ZONING), COMP. B SIMULATION

Liner Segment	T	β	$\vec{V}_o$	θ	M_j	$\vec{V}_o$ Final
apex1	11.0	65.0°	1.228	51.16°	.7386	1.213
2	12.0	40.0°	1.378	36.22°	.5750	1.410
3	13.0	31.0°	1.628	29.05°	.4263	1.647
4	14.5	33.0°	1.934	28.35°	.5664	1.871
5	16.0	35.0°	2.064	29.01°	.7299	2.049
6	17.0	36.0°	2.119	30.27°	.8710	2.167
7	18.5	37.0°	2.196	30.91°	1.0238	2.222
8	20.0	38.0°	2.241	31.09°	1.1886	2.223
9	21.0	39.0°	2.209	30.64°	1.3659	2.184
10	22.5	40.0°	2.116	31.16°	1.5559	2.119
11	24.0	41.0°	2.027	30.45°	1.7589	2.041
12	25.5	43.0°	1.964	29.90°	2.0660	1.956
13	27.5	46.0°	1.860	30.34°	2.5066	1.858
14	29.5	50.0°	1.721	30.25°	3.1175	1.729
15	31.5	55.0°	1.533	29.81°	3.9421	1.529

TABLE B-3

42° CURVED APEX (POLAR ZONING), COMP. B SIMULATION

(Continuation)

Liner Segment	$\vec{V}_{o_Z}$ Final	$\vec{V}_{o_R}$ Final	$\vec{V}_f$	$\vec{V}_{sp}$	V_j	V_j^o
apex1	0.945	0.761	0.840	1.300	2.140	2.140
2	0.833	1.138	1.770	2.189	3.959	2.936
3	0.800	1.440	2.796	3.197	5.993	3.685
4	0.888	1.647	3.024	3.424	6.448	4.364
5	0.994	1.792	3.124	3.553	6.677	4.920
6	1.092	1.872	3.185	3.669	6.854	5.351
7	1.141	1.906	3.167	3.670	6.837	5.660
8	1.148	1.904	3.093	3.585	6.678	5.857
9	1.113	1.879	2.986	3.433	6.419	5.960
10	1.096	1.813	2.821	3.257	6.078	5.980
11	1.034	1.759	2.681	3.057	5.738	
12	0.975	1.696	2.487	2.794	5.281	
13	0.939	1.604	2.230	2.488	4.718	
14	0.871	1.494	1.950	2.125	4.075	
15	0.760	1.327	1.620	1.689	3.309	

TABLE B-4

42° (DOUBLE-ZONING), COMP. B SIMULATION

Liner Segment	T	β	$\vec{V}_o$	ϑ	M_j	$\vec{V}_o$ Final
apex1	8.25	22.0°	0.219	77.18°	.0193	0.209
2	9.25	25.0°	0.657	65.52°	.0415	0.626
3	10.00	30.0°	0.811	55.34°	.0830	0.947
4	10.75	31.0°	1.253	38.60°	.1138	1.194
5	11.50	31.5°	1.479	34.07°	.1435	1.385
6	12.25	32.0°	1.545	32.77°	.1749	1.536
7	13.00	32.5°	1.593	32.94°	.2080	1.656
8	13.75	33.5°	1.742	32.82°	.2500	1.756
9	14.50	34.0°	1.829	34.89°	.2876	1.841
10	15.25	34.5°	1.918	34.57°	.3270	1.915
11	16.00	35.0°	1.984	33.78°	.3683	1.982
12	16.75	35.5°	2.046	34.20°	.4115	2.041
13	17.50	36.0°	2.112	35.36°	.4566	2.094
14	18.25	36.5°	2.149	35.57°	.5036	2.138
15	19.00	37.0°	2.167	35.61°	.5527	2.173
16	19.75	37.5°	2.195	36.09°	.6038	2.198
17	20.50	38.0°	2.205	36.54°	.6570	2.210
18	21.25	39.0°	2.199	36.44°	.7301	2.209
19	22.00	40.0°	2.189	36.34°	.8079	2.196
20	22.75	40.5°	2.178	35.73°	.8698	2.172
21	23.50	41.5°	2.161	34.75°	.9558	2.139
22	24.50	42.0°	2.086	36.75°	1.0234	2.103
23	25.25	42.5°	2.074	35.36°	1.0933	2.071

TABLE B-4

42^{o} (DOUBLE-ZONING), COMP. B SIMULATION

(Continuation)

Liner Segment	$\vec{V}_{o_Z}$ Final	$\vec{V}_{o_R}$ Final	$\vec{V}_f$	$\vec{V}_{sp}$	V_j	V_j^{o}
apex1	0.204	0.046	0.123	0.318	0.441	0.441
2	0.570	0.259	0.613	1.125	1.738	1.326
3	0.779	0.539	1.078	1.713	2.791	2.172
4	0.745	0.933	1.812	2.298	4.110	3.028
5	0.776	1.147	2.195	2.648	4.843	3.677
6	0.831	1.292	2.438	2.899	5.337	4.181
7	0.900	1.390	2.587	3.082	5.669	4.576
8	0.952	1.476	2.674	3.182	5.856	4.885
9	1.053	1.510	2.700	3.292	5.992	5.126
10	1.087	1.577	2.784	3.382	6.166	5.332
11	1.102	1.647	2.871	3.454	6.325	5.514
12	1.147	1.688	2.907	3.513	6.420	5.667
13	1.212	1.708	2.906	3.563	6.469	5.794
14	1.244	1.739	2.924	3.594	6.518	5.902
15	1.265	1.767	2.936	3.610	6.546	5.992
16	1.295	1.776	2.917	3.610	6.527	6.063
17	1.316	1.776	2.885	3.589	6.474	6.115
18	1.312	1.777	2.824	3.506	6.330	6.142
19	1.301	1.769	2.752	3.409	6.161	6.144
20	1.268	1.763	2.715	3.332	6.047	
21	1.219	1.758	2.653	3.206	5.859	
22	1.258	1.685	2.518	3.129	5.647	
23	1.199	1.689	2.500	3.042	5.542	

TABLE B-5

60° (DOUBLE-ZONING), COMP. B SIMULATION

Liner Segment	T	β	$\vec{V}_o$	θ	M_j	$\vec{V}_o$ Final
apexi	12.50	33.0°	0.252	76.62°	.0306	0.213
2	13.00	33.5°	0.578	60.83°	.0526	0.679
3	14.00	35.0°	1.055	52.13°	.0801	1.037
4	14.50	40.0°	1.428	43.89°	.1333	1.311
5	15.00	41.0°	1.476	39.59°	.1708	1.524
6	16.00	44.0°	1.649	46.45°	.2309	1.689
7	16.50	44.5°	1.821	43.22°	.2722	1.822
8	17.00	45.0°	1.946	42.56°	.3151	1.931
9	17.75	46.0°	2.024	43.64°	.3672	2.025
10	18.50	46.5°	2.098	45.06°	.4142	2.107
11	19.00	48.5°	2.192	44.33°	.4911	2.181
12	19.50	49.0°	2.255	43.45°	.5442	2.247
13	20.25	49.5°	2.297	44.08°	.5990	2.305
14	21.00	50.0°	2.348	45.41°	.6556	2.353
15	21.50	51.0°	2.398	44.44°	.7273	2.388
16	22.25	51.5°	2.406	45.34°	.7884	2.407
17	23.00	53.0°	2.395	46.00°	.8820	2.406
18	23.75	54.5°	2.387	46.77°	.9819	2.382

TABLE B-5

60° (DOUBLE-ZONING), COMP. B SIMULATION

(Continuation)

Liner Segment	$\vec{V}_{o_Z}$ Final	$\vec{V}_{o_R}$ Final	$\vec{V}_f$	$\vec{V}_{sp}$	V_j	V_j^o
apex1	0.207	0.049	0.090	0.282	0.372	0.372
2	0.593	0.331	0.600	1.093	1.693	1.207
3	0.819	0.637	1.111	1.729	2.840	2.008
4	0.909	0.945	1.470	2.035	3.505	2.681
5	0.971	1.174	1.789	2.322	4.111	3.203
6	1.224	1.164	1.676	2.429	4.105	3.502
7	1.248	1.328	1.895	2.599	4.494	3.780
8	1.306	1.422	2.011	2.728	4.739	4.015
9	1.398	1.465	2.037	2.813	4.850	4.200
10	1.491	1.488	2.051	2.903	4.954	4.351
11	1.524	1.560	2.083	2.904	4.987	4.473
12	1.545	1.631	2.161	2.963	5.124	4.588
13	1.604	1.656	2.178	3.018	5.196	4.686
14	1.676	1.652	2.157	3.062	5.219	4.766
15	1.672	1.705	2.194	3.053	5.247	4.835
16	1.712	1.692	2.162	3.058	5.220	4.887
17	1.731	1.671	2.092	2.990	5.082	4.912
18	1.736	1.632	2.005	2.900	4.905	

APPENDIX C

GRAPHICAL COMPARISONS OF THE VELOCITY/MASS DISTRIBUTIONS OBTAINED USING HEMP AND DATA FROM THE TEST INVOLVING ROTATED SHAPED CHARGES.

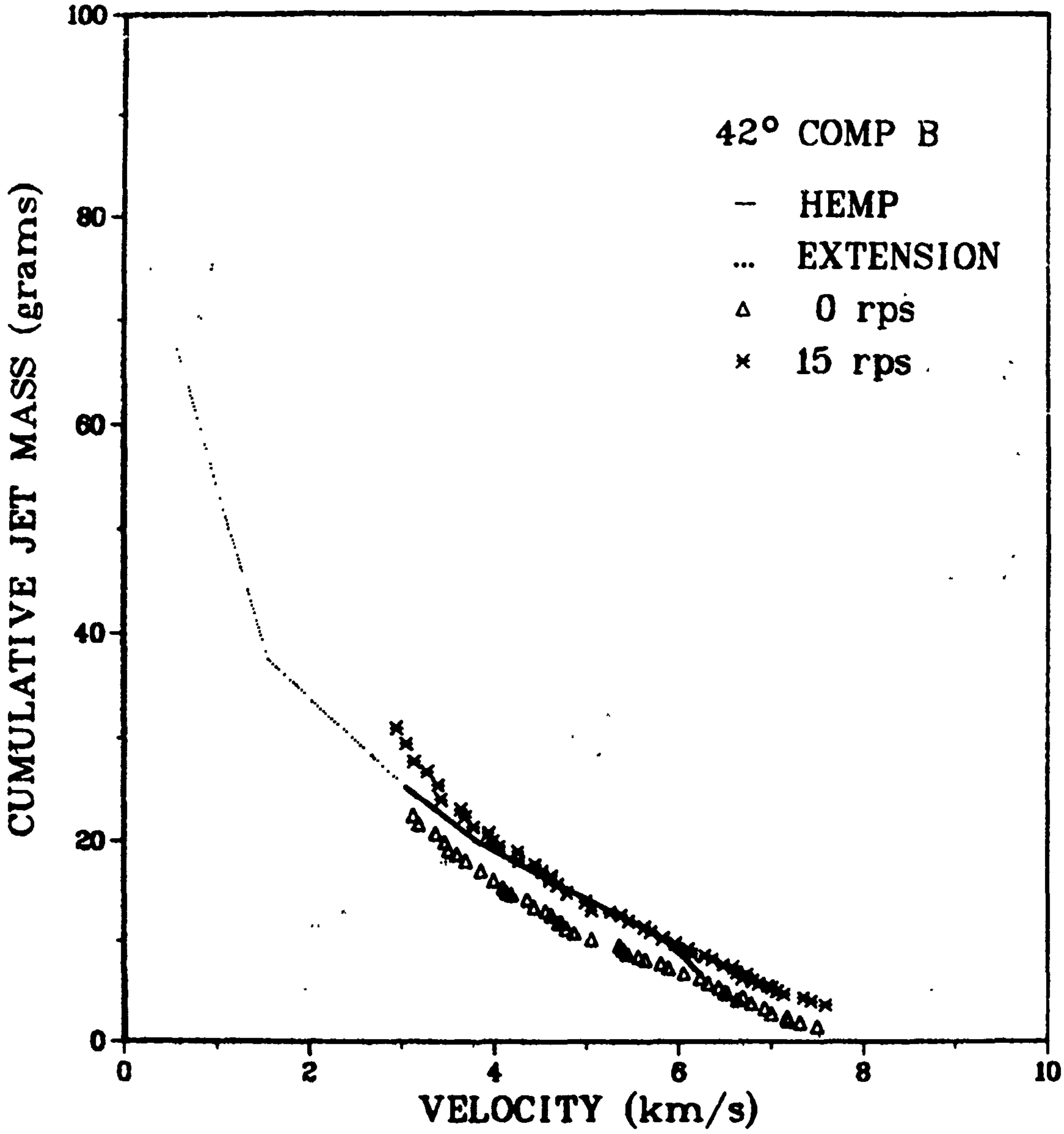

C-1. 42°, Comp. B Simulation, Basic Configuration. (0 and 15rps)

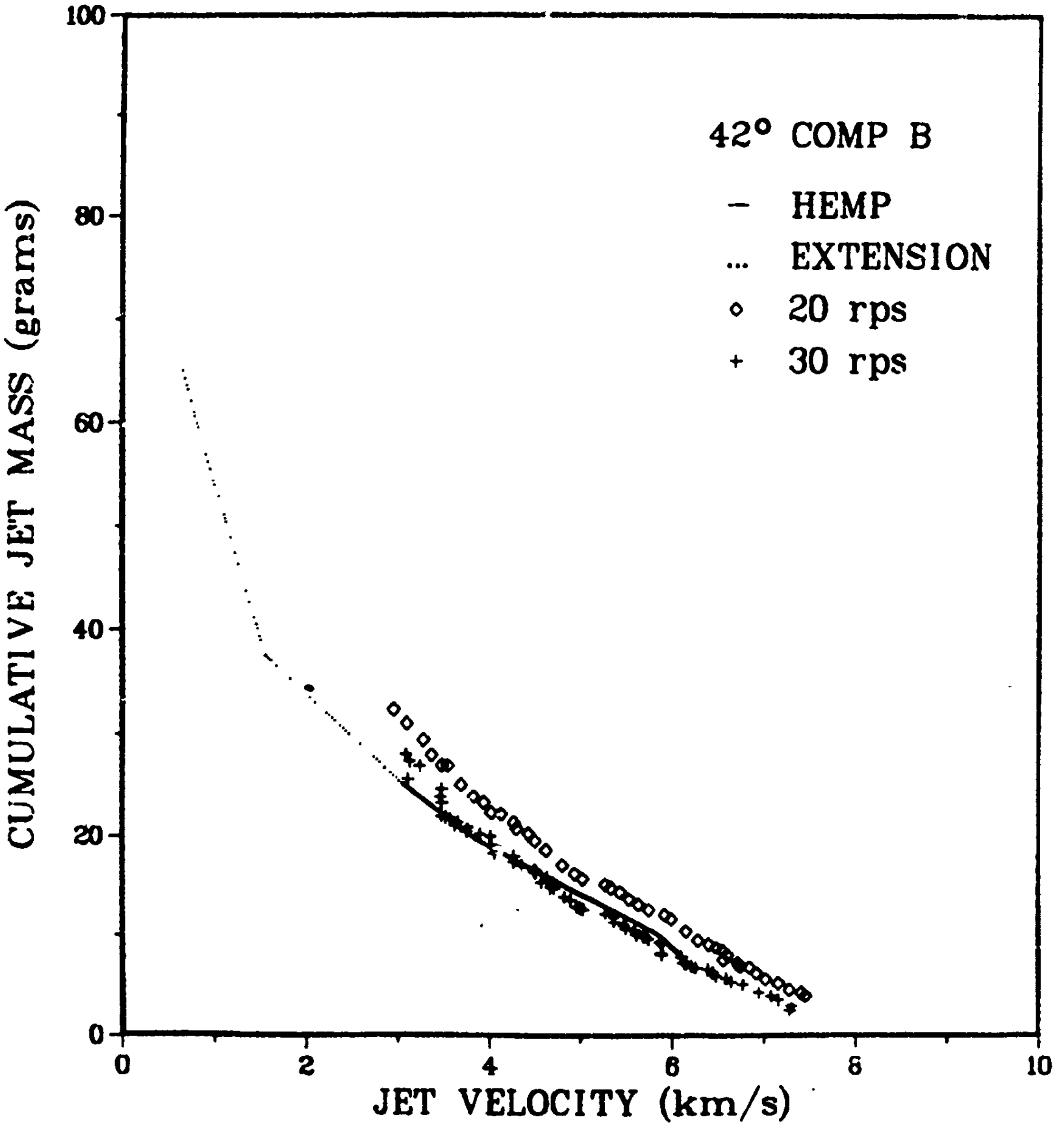

C-2. 42°, Comp. B Simulation, Basic Configuration. (20 and 30rps)

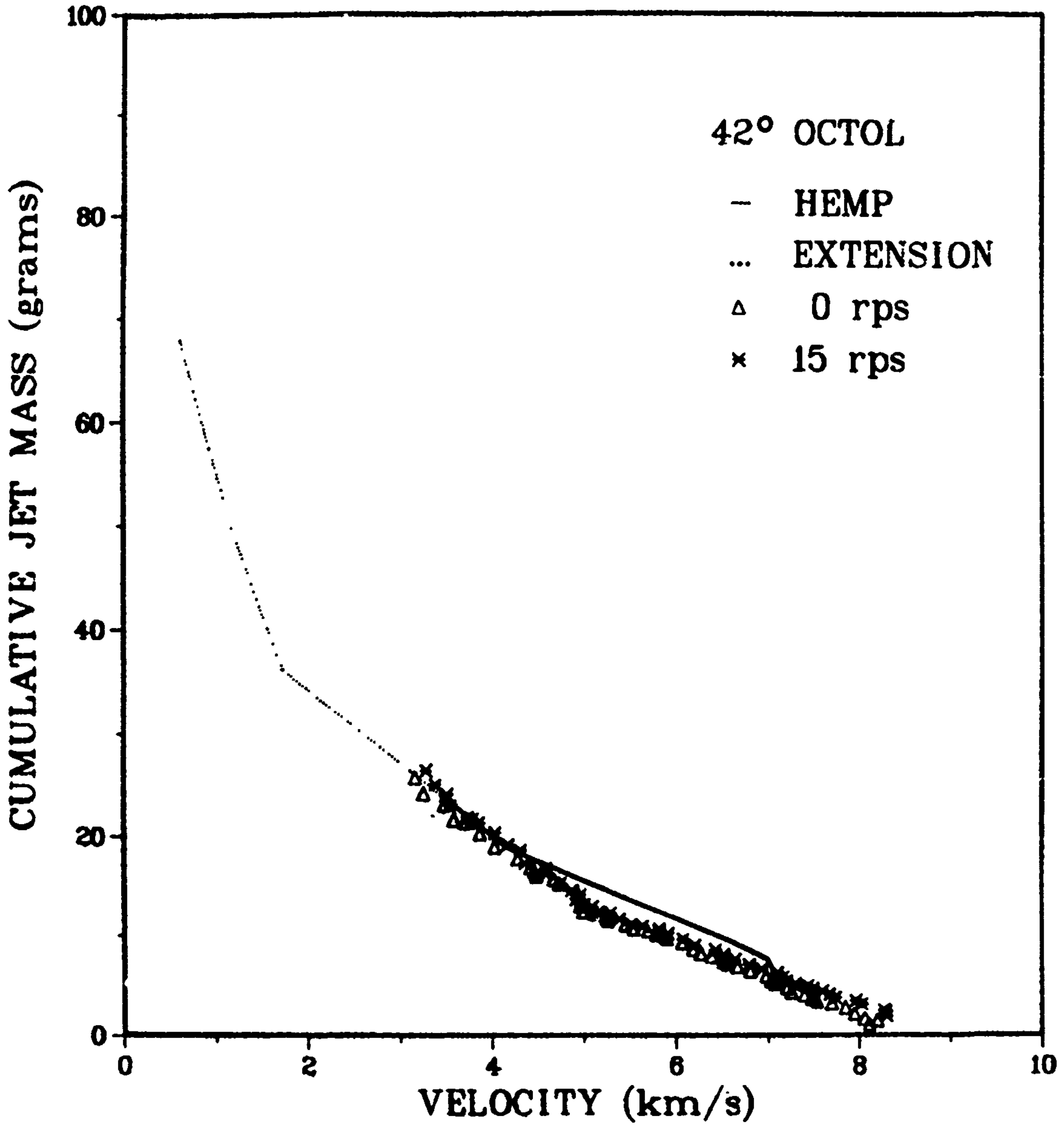

C-3. 42°, Octol Simulation, Basic Configuration. (0 and 15rps)

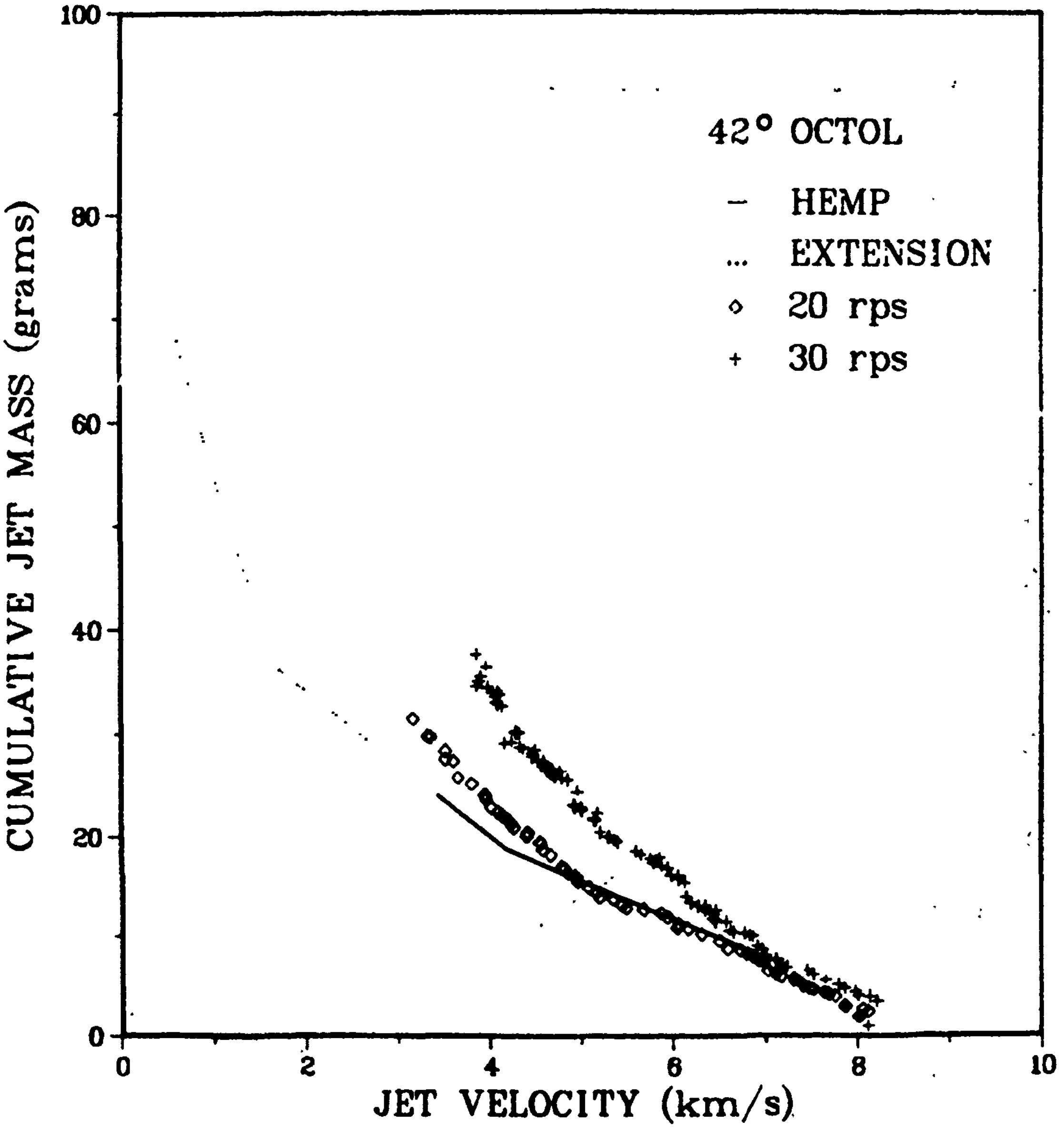

C-4. 42°, Octol Simulation, Basic Configuration. (20 and 30rps)

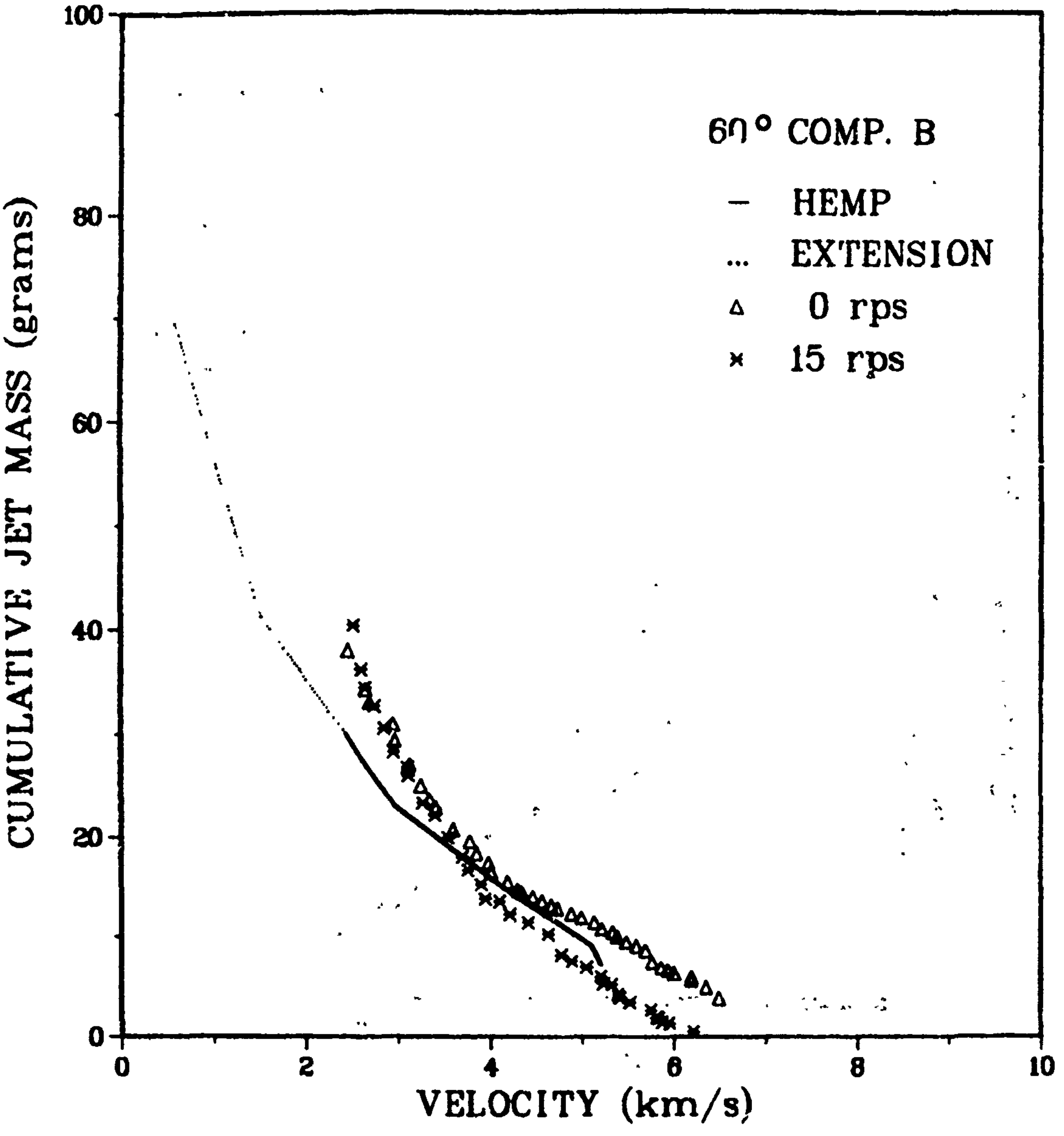

C-5. 60°, Comp. B Simulation, Basic Configuration. (0 and 15rps)

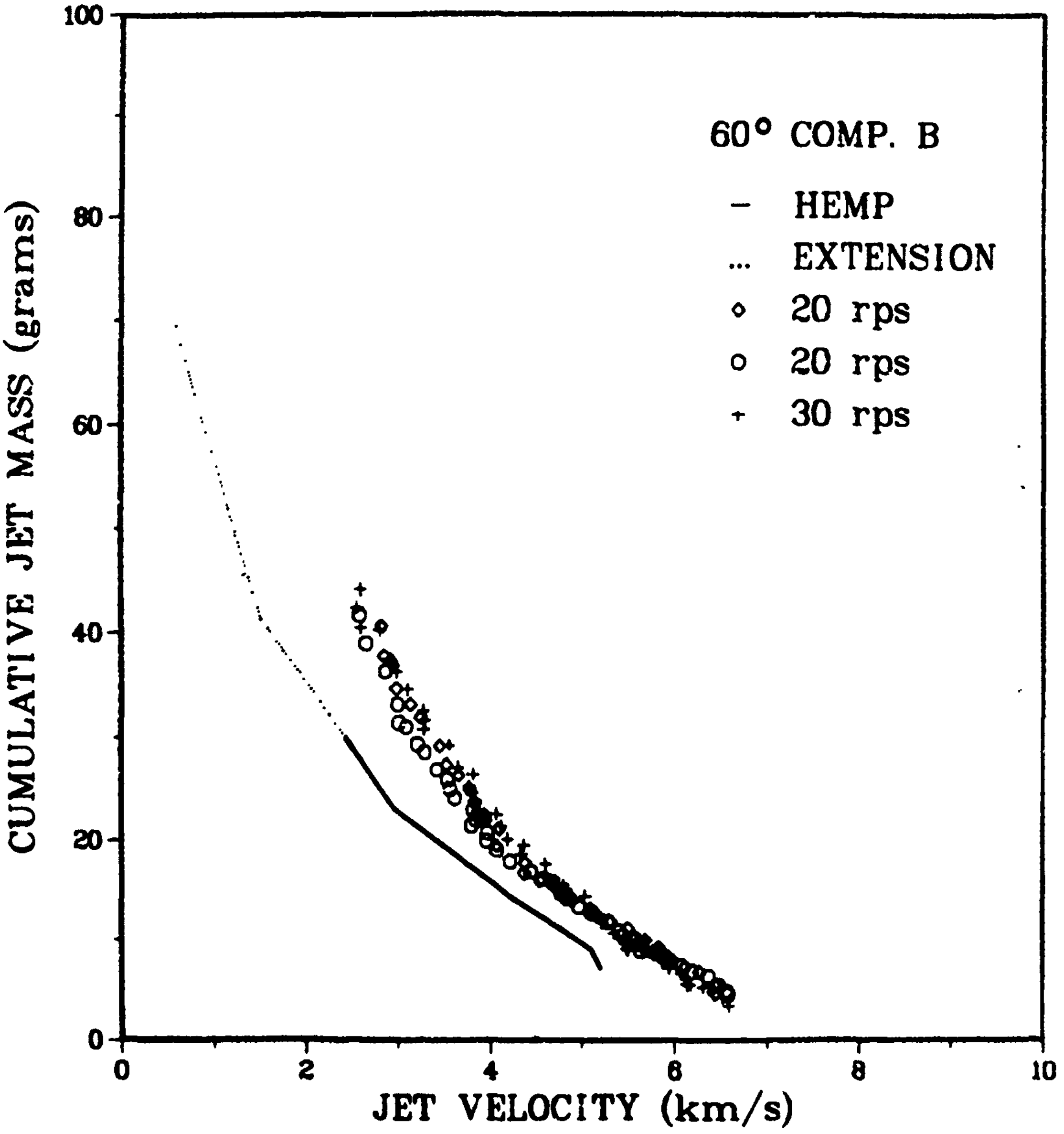

C-6. 60°, Comp. B Simulation, Basic Configuration. (20 and 30rps)

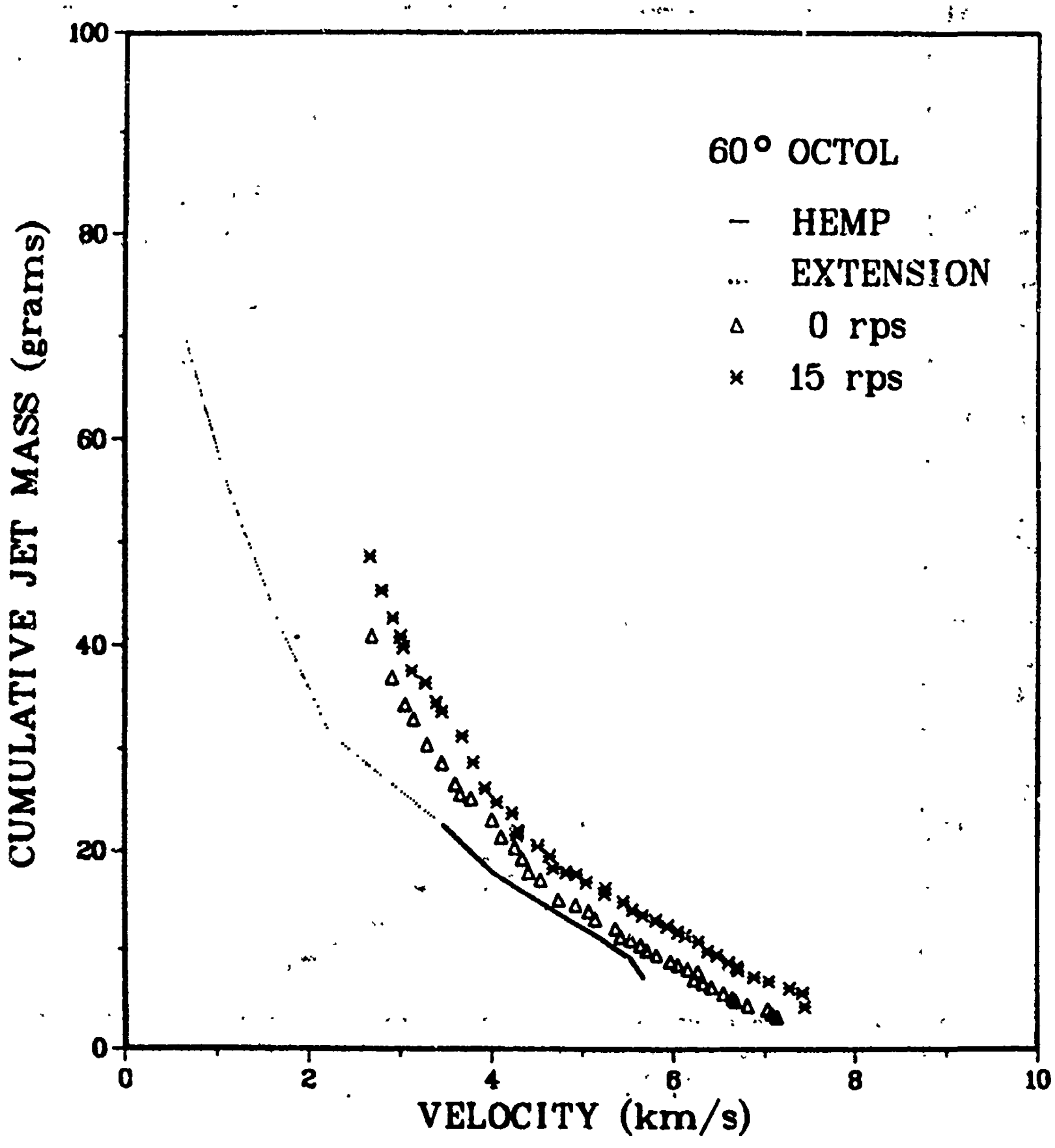

C-7. 60°, Octol Simulation, Basic Configuration. (0 and 15rps)

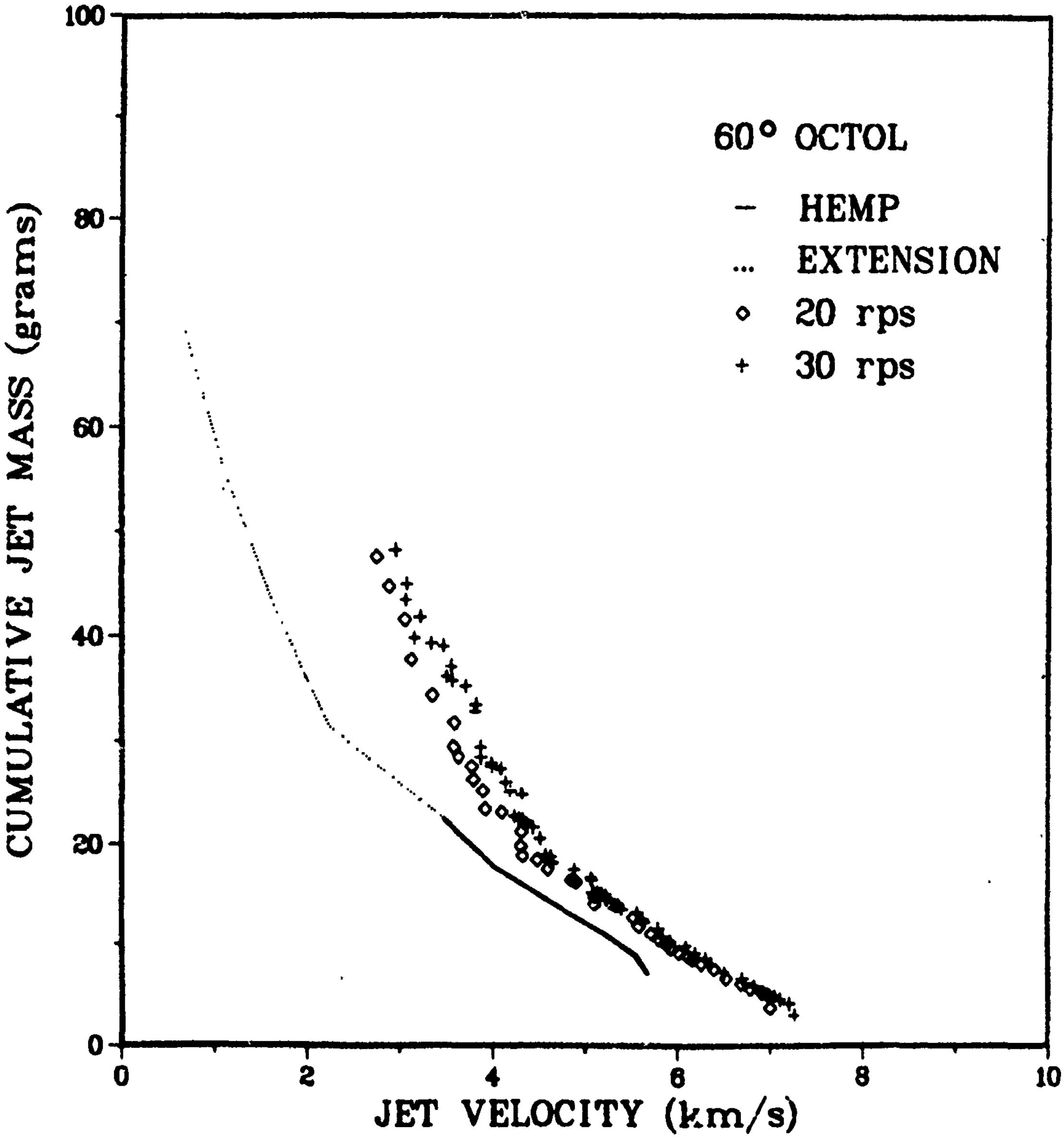

C-8. 60°, Octol Simulation, Basic Configuration. (20 and 30rps)

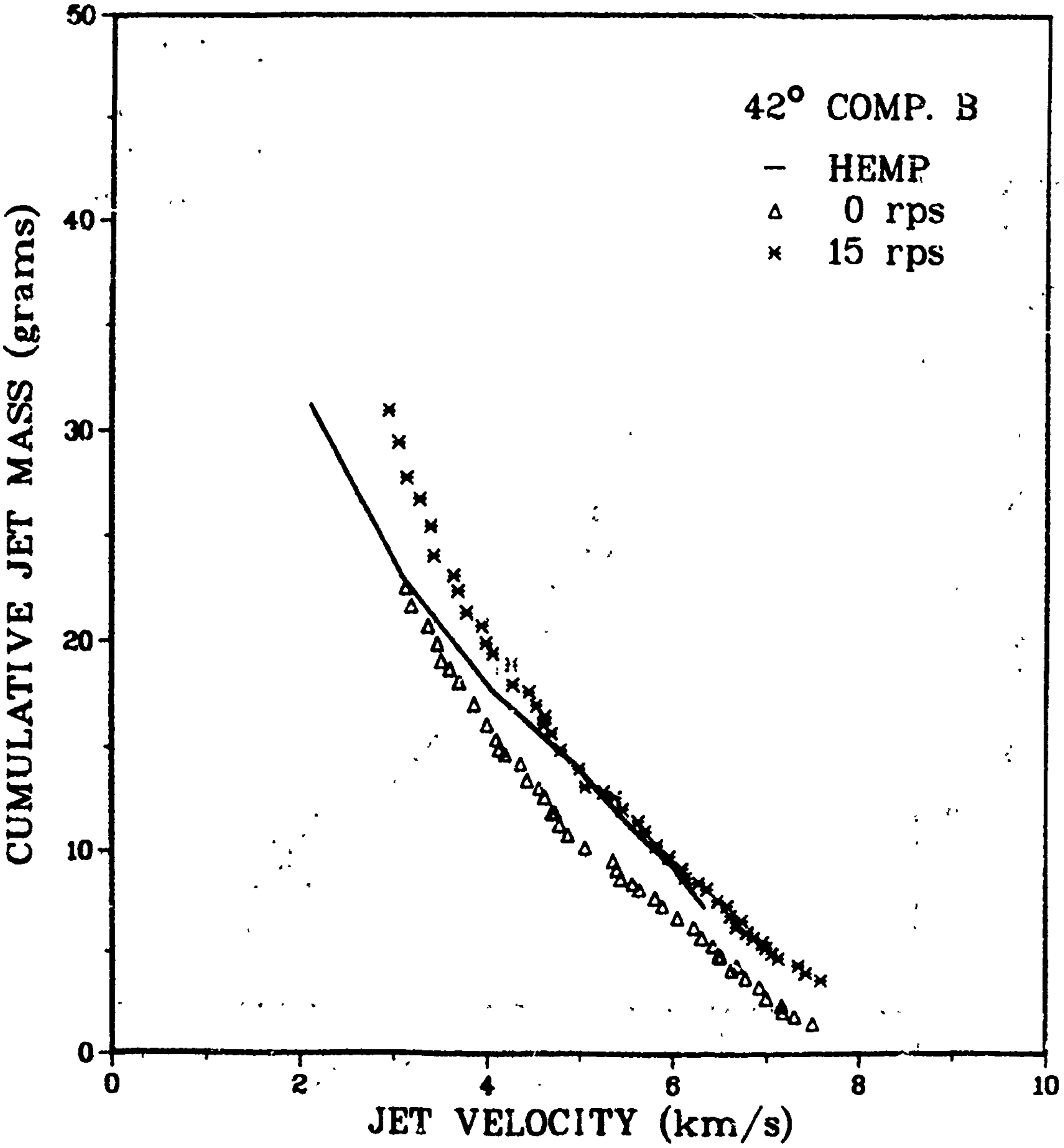

C-9. 42°, Comp. B Simulation, Curved Apex Configuration. (0 and 15rps)

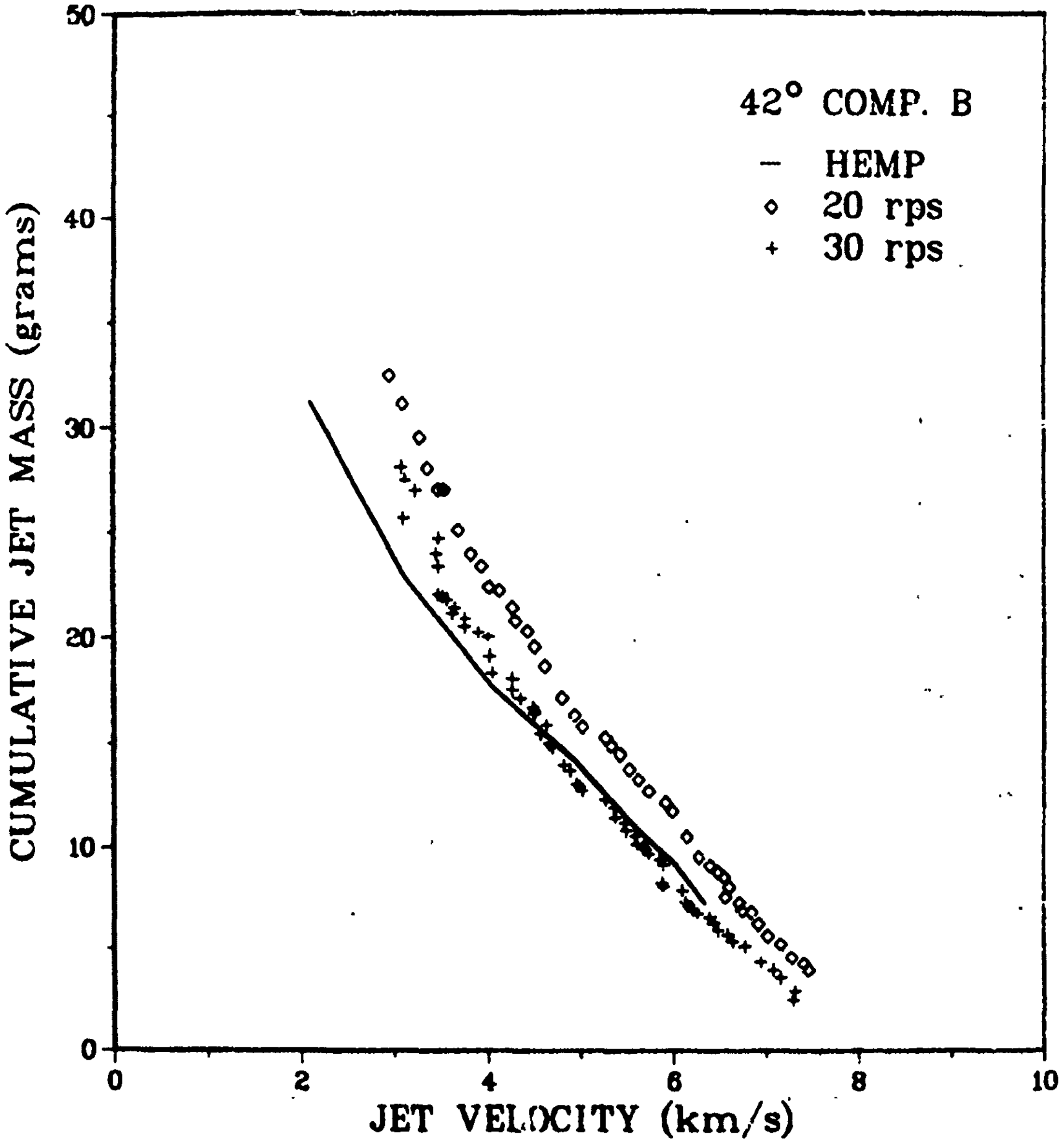

C-10. 42°, Comp. B Simulation, Curved Apex Configuration. (20 and30rps)

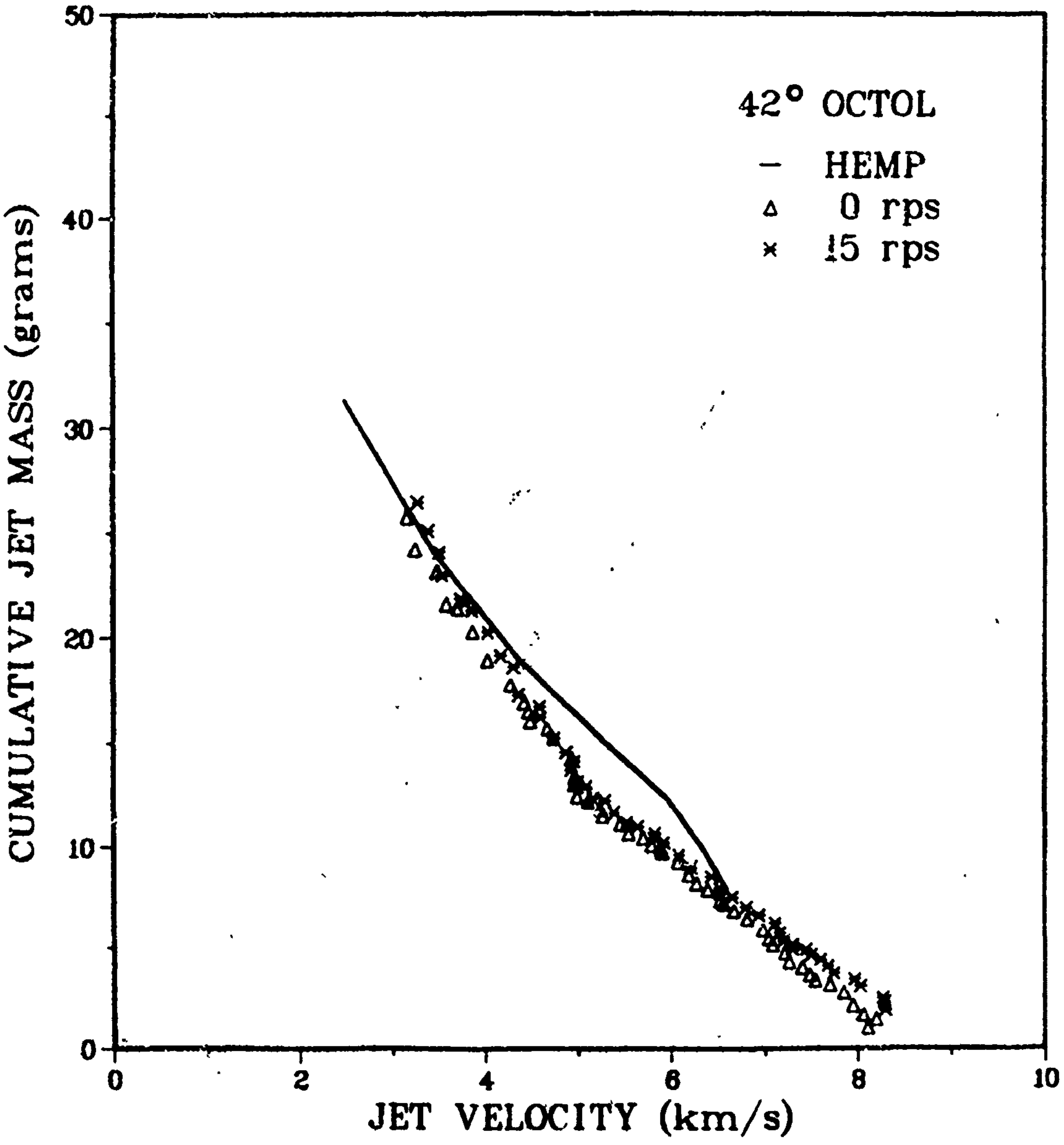

C-11. 42°, Octol Simulation, Curved Apex Configuration. (0 and 15rps)

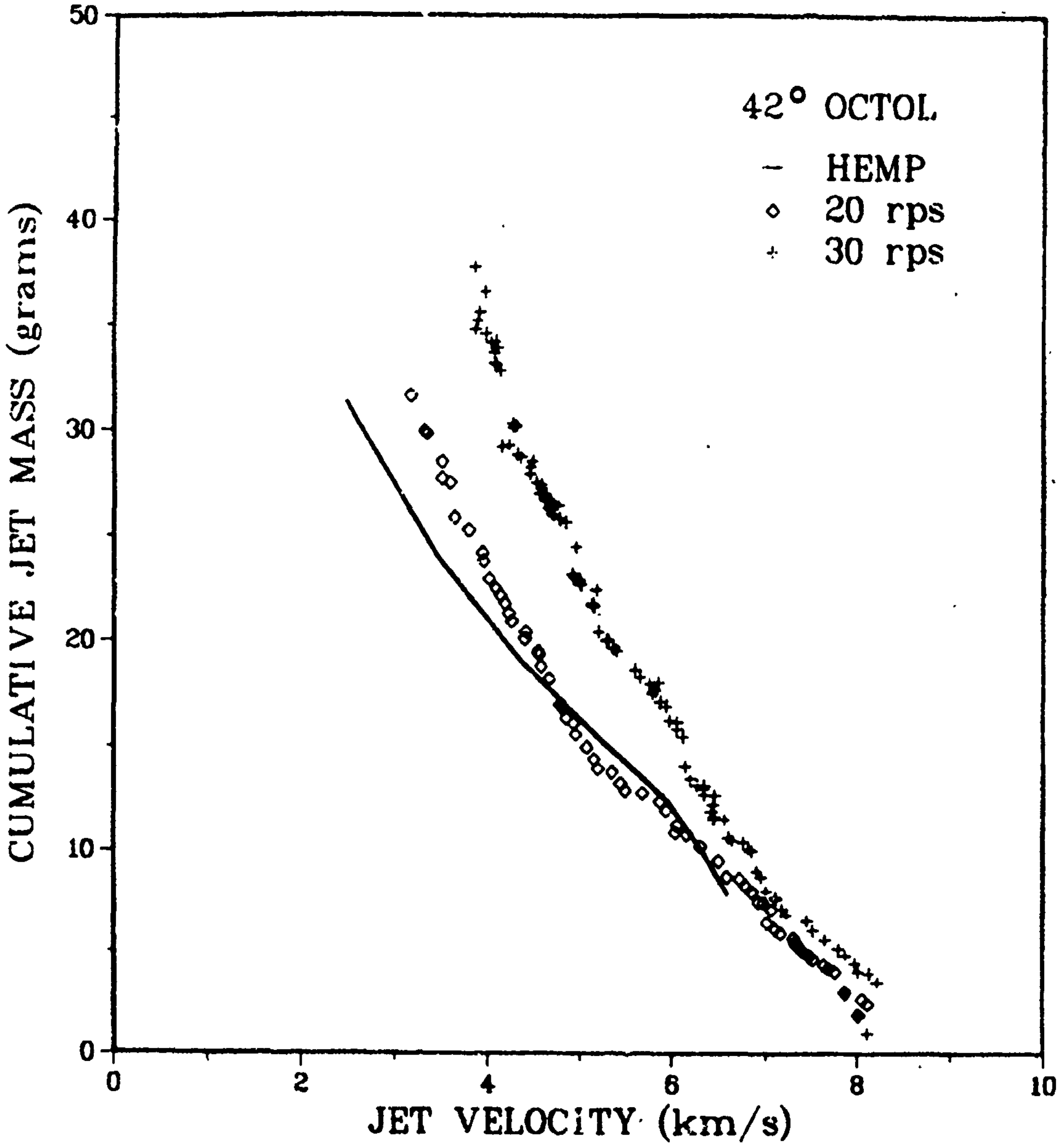

C-12. 42°, Octol Simulation, Curved Apex Configuration. (20 and 30rps)

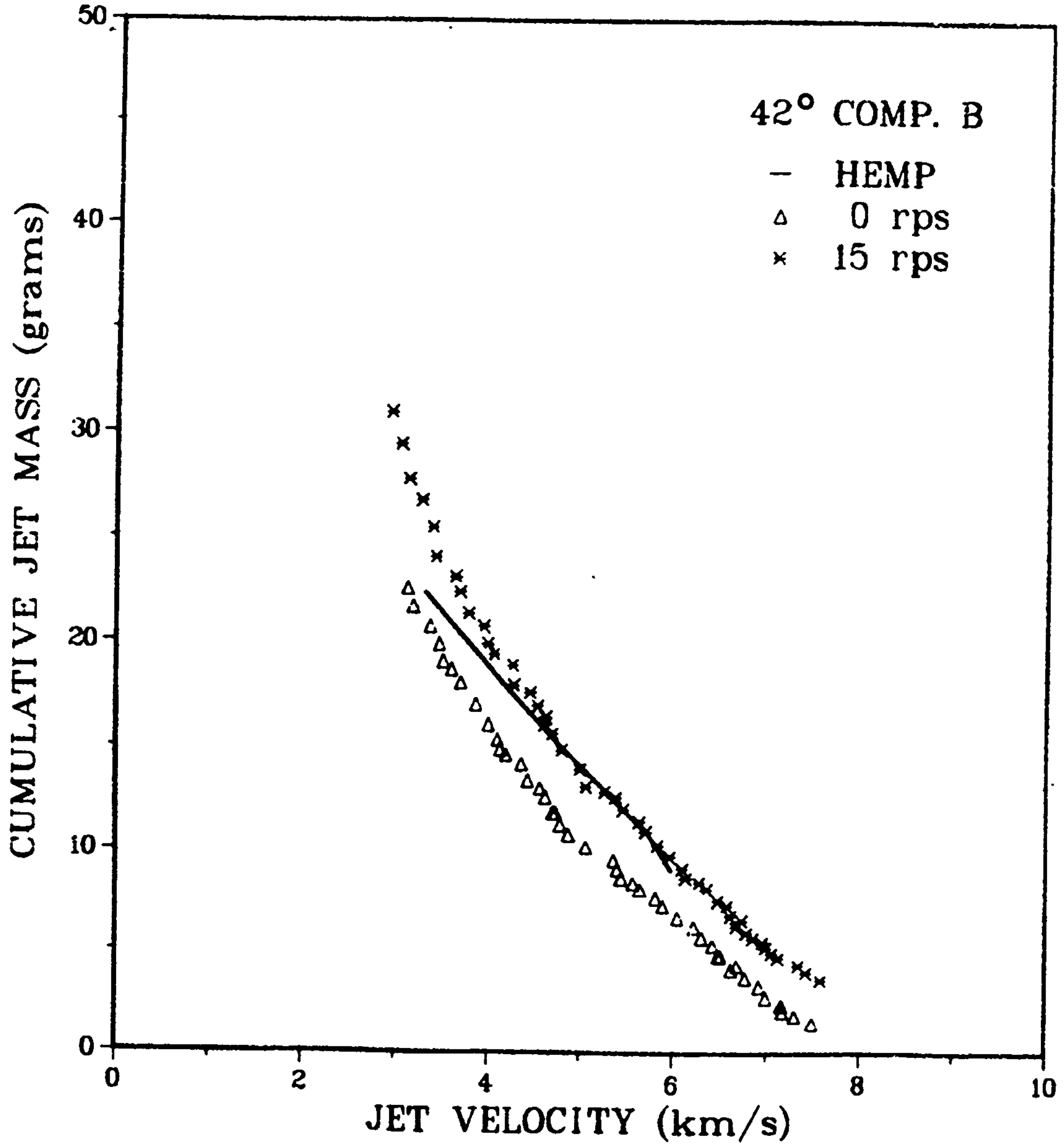

C-13. 42°, Comp. B Simulation, Curved Apex Configuration, Polar Zoning (0 and 15rps)

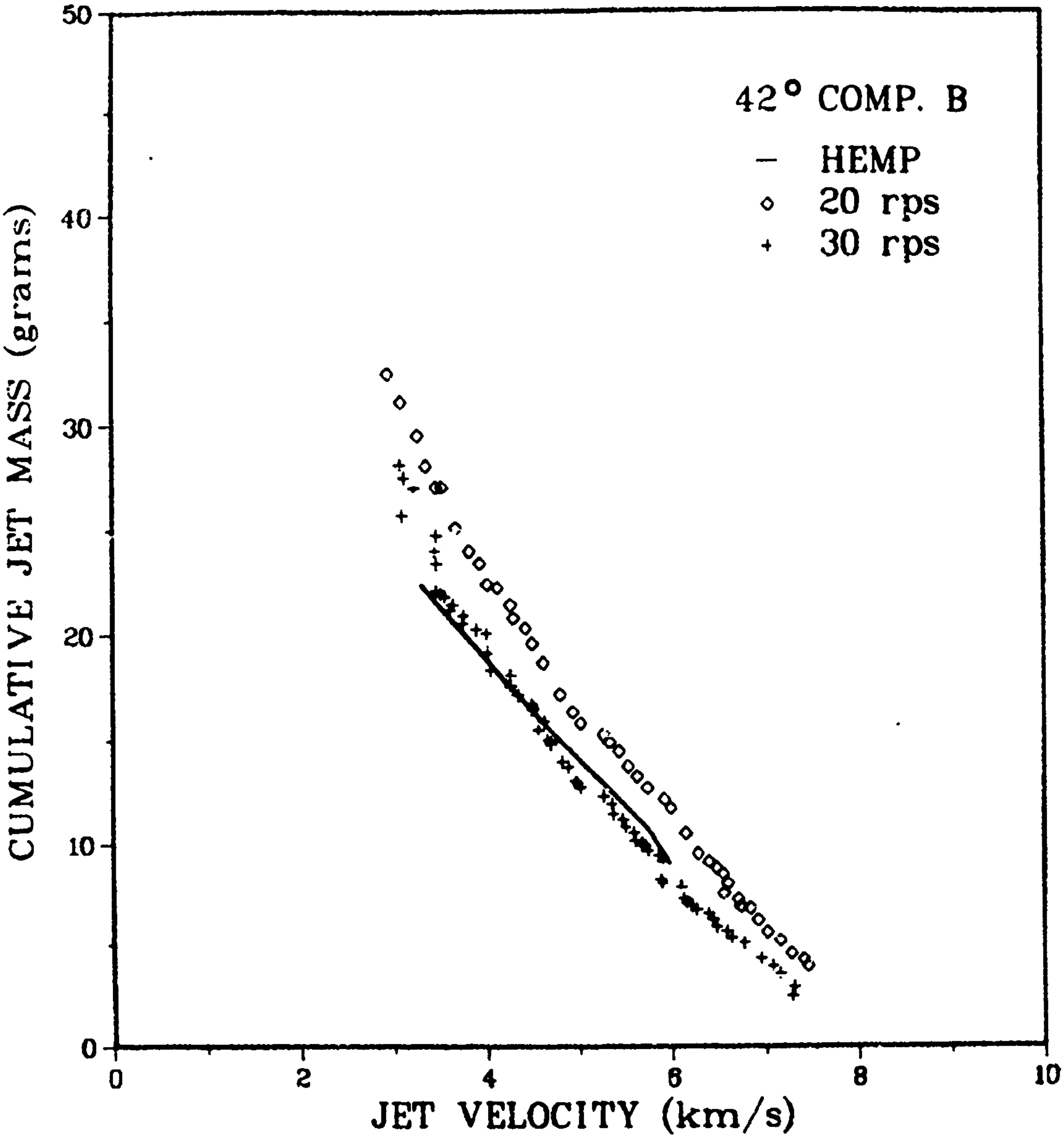

C-14. 42°, Comp. B Simulation, Curved Apex Configuration, Polar Zoning (20 and 30rps)

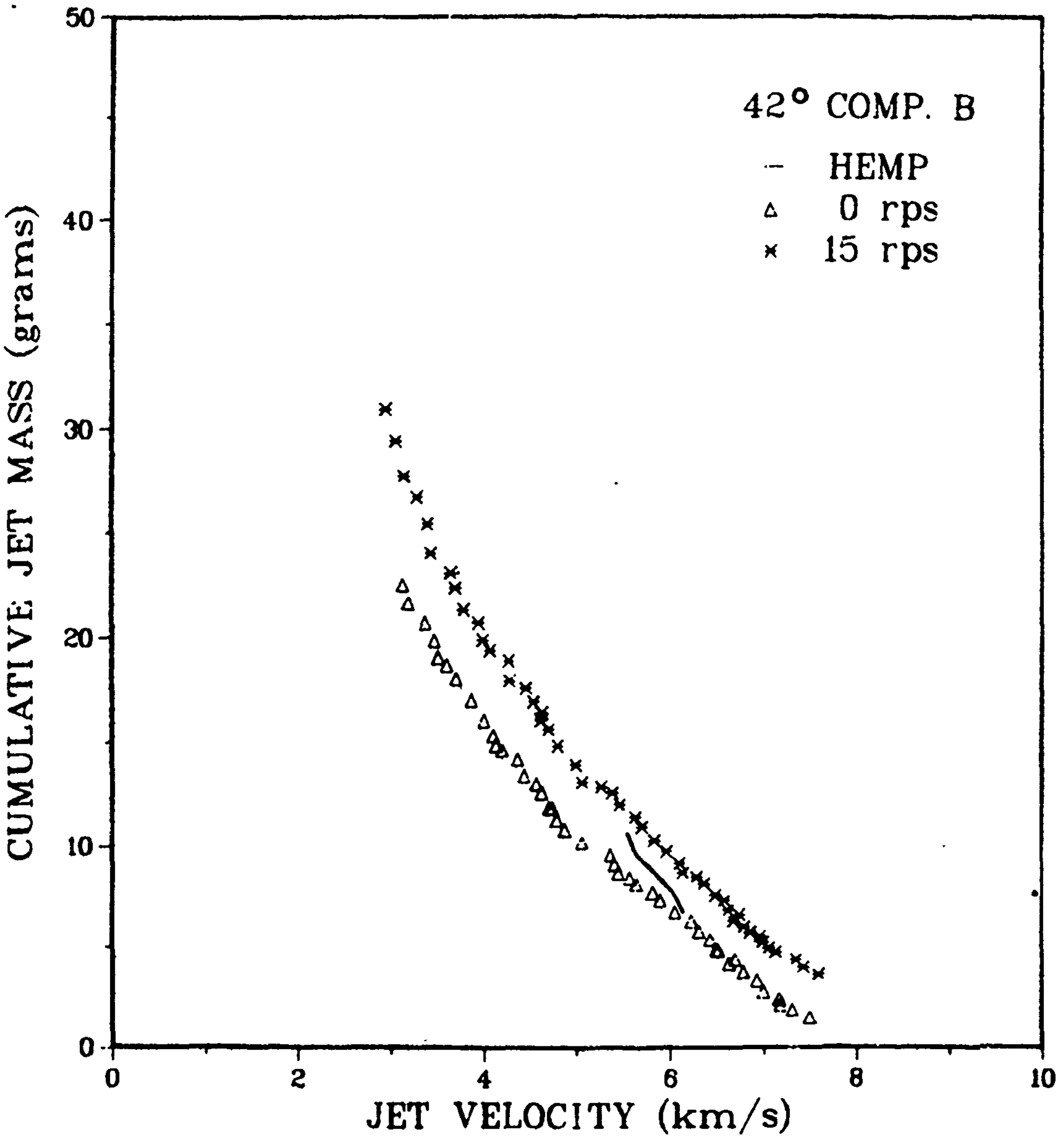

C-15. 42°, Comp. B Simulation, Double-Zoning Configuration. (0 and 15rps)

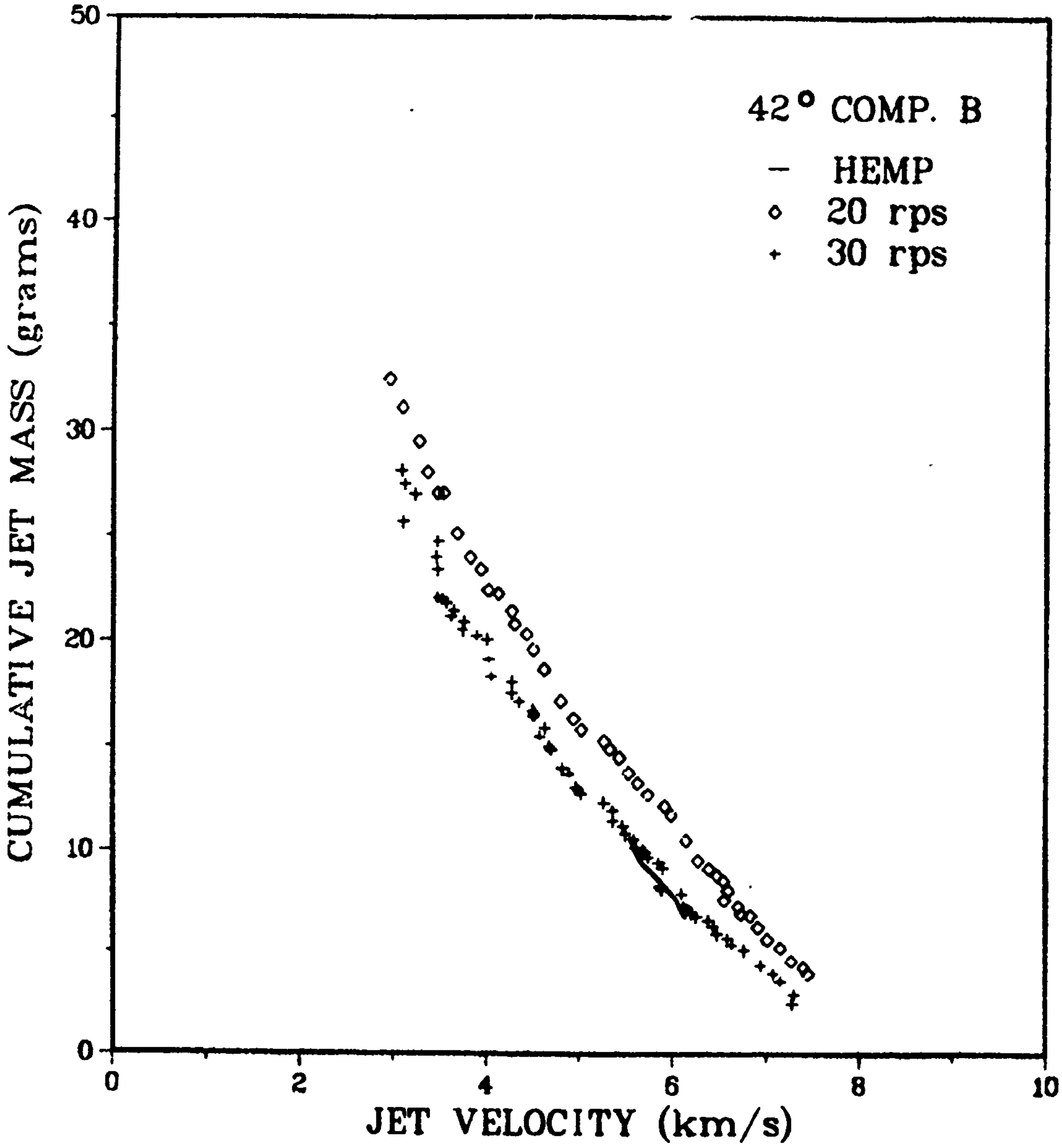

C-16. 42°, Comp. B Simulation, Double-Zoning Configuration. (20 and 30rps)

APPENDIX D

GRAPHICAL COMPARISONS OF THE VELOCITY/MASS DISTRIBUTIONS OBTAINED USING HEMP AND DATA FROM THE TEST INVOLVING NON-ROTATED SHAPED CHARGES.

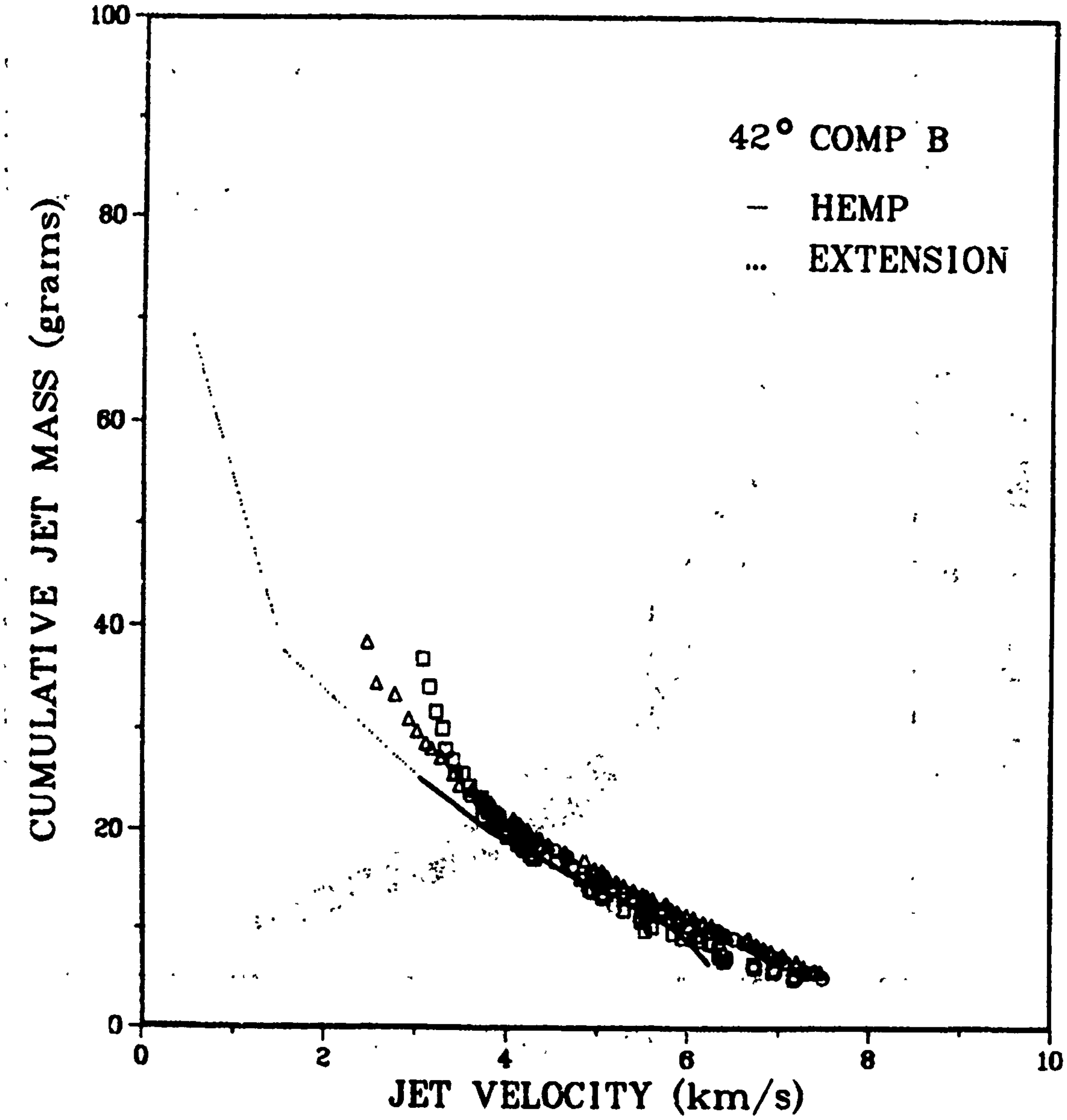

D-1-a. 42°, Comp. B Simulation, Basic Configuration.

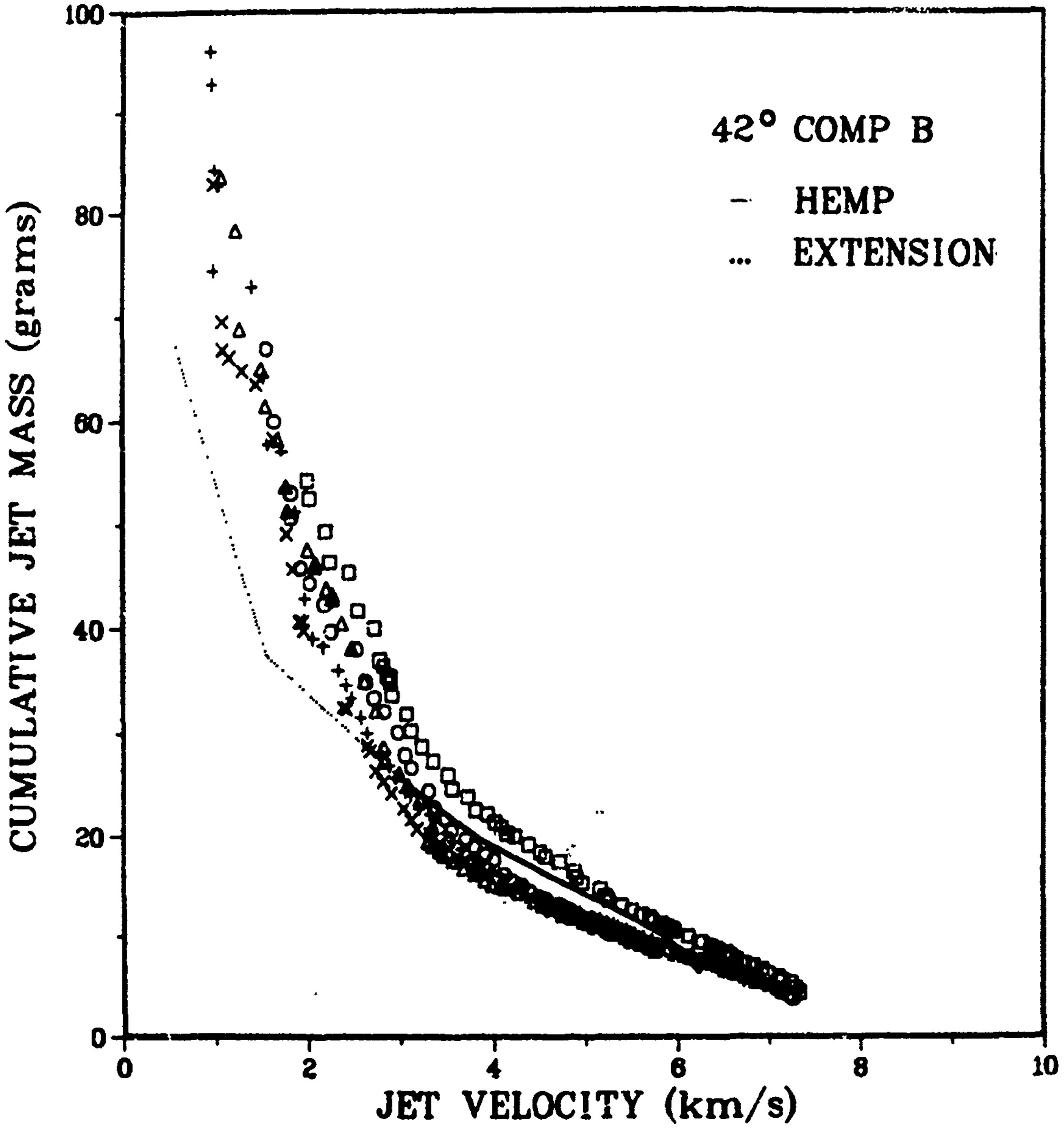

D-1-b. 42°, Comp. B Simulation, Basic Configuration.

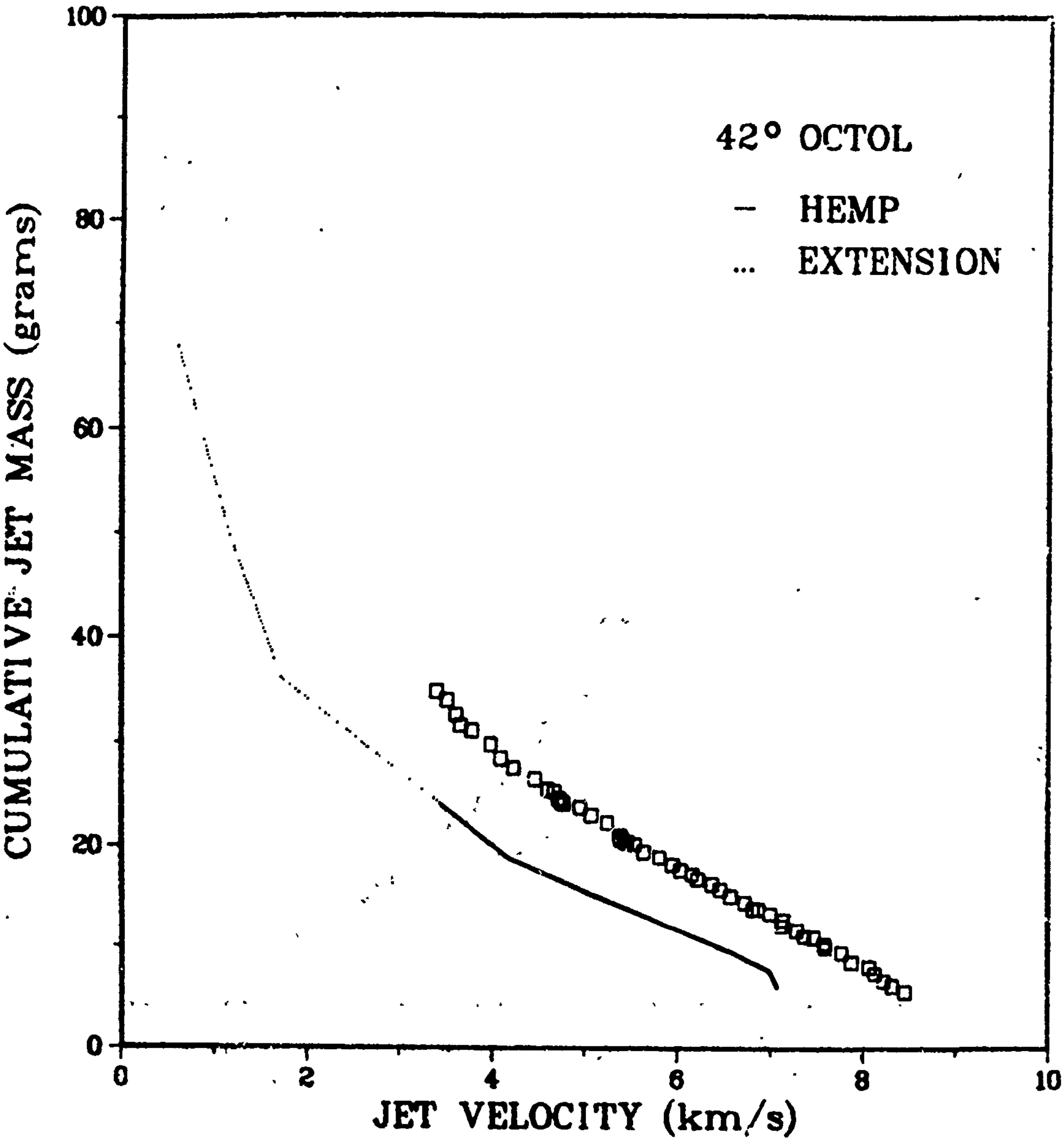

D-2. 42°, Octol Simulation, Basic Configuration.

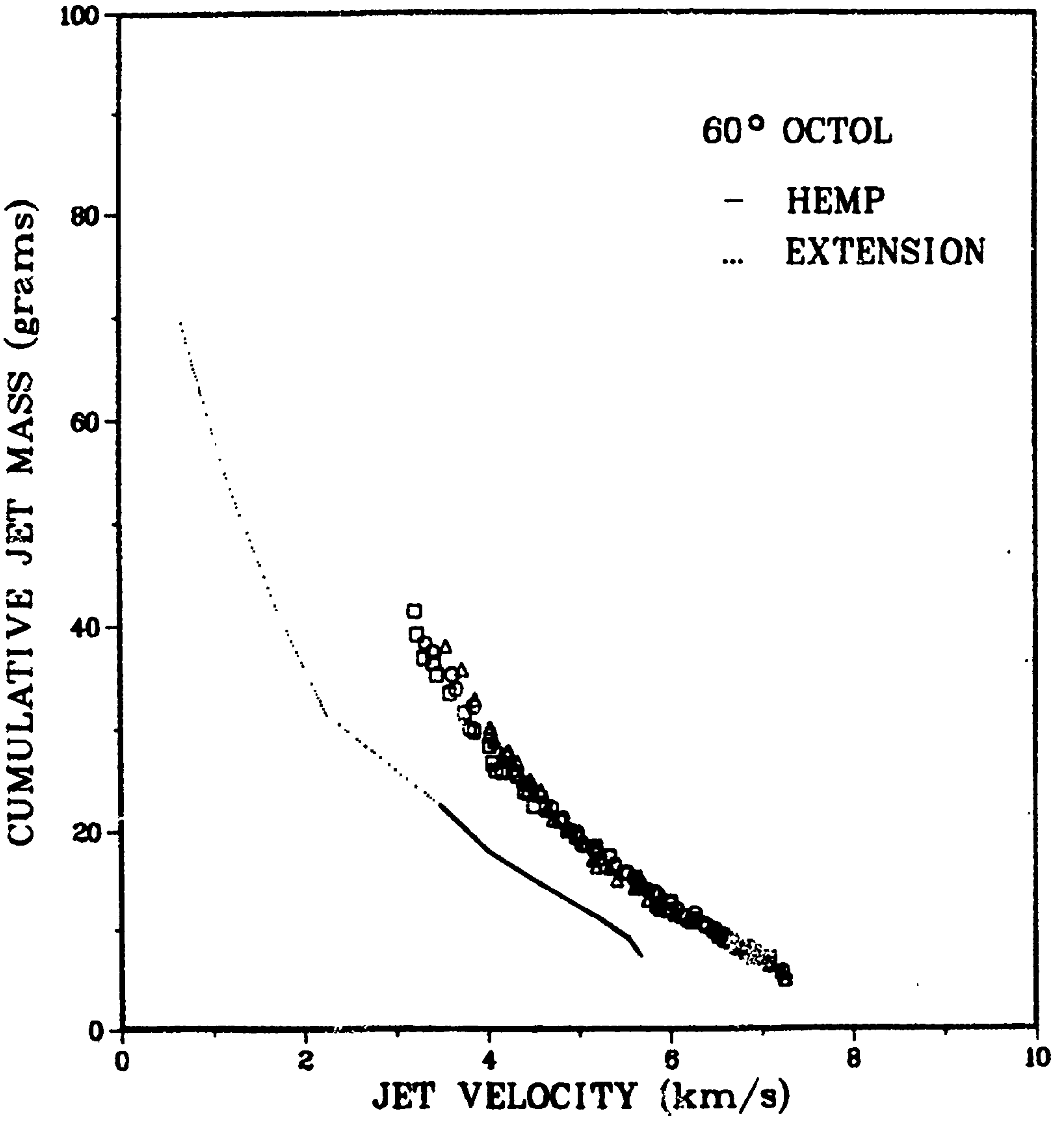

D-3-a. 60°, Octol Simulation, Basic Configuration.

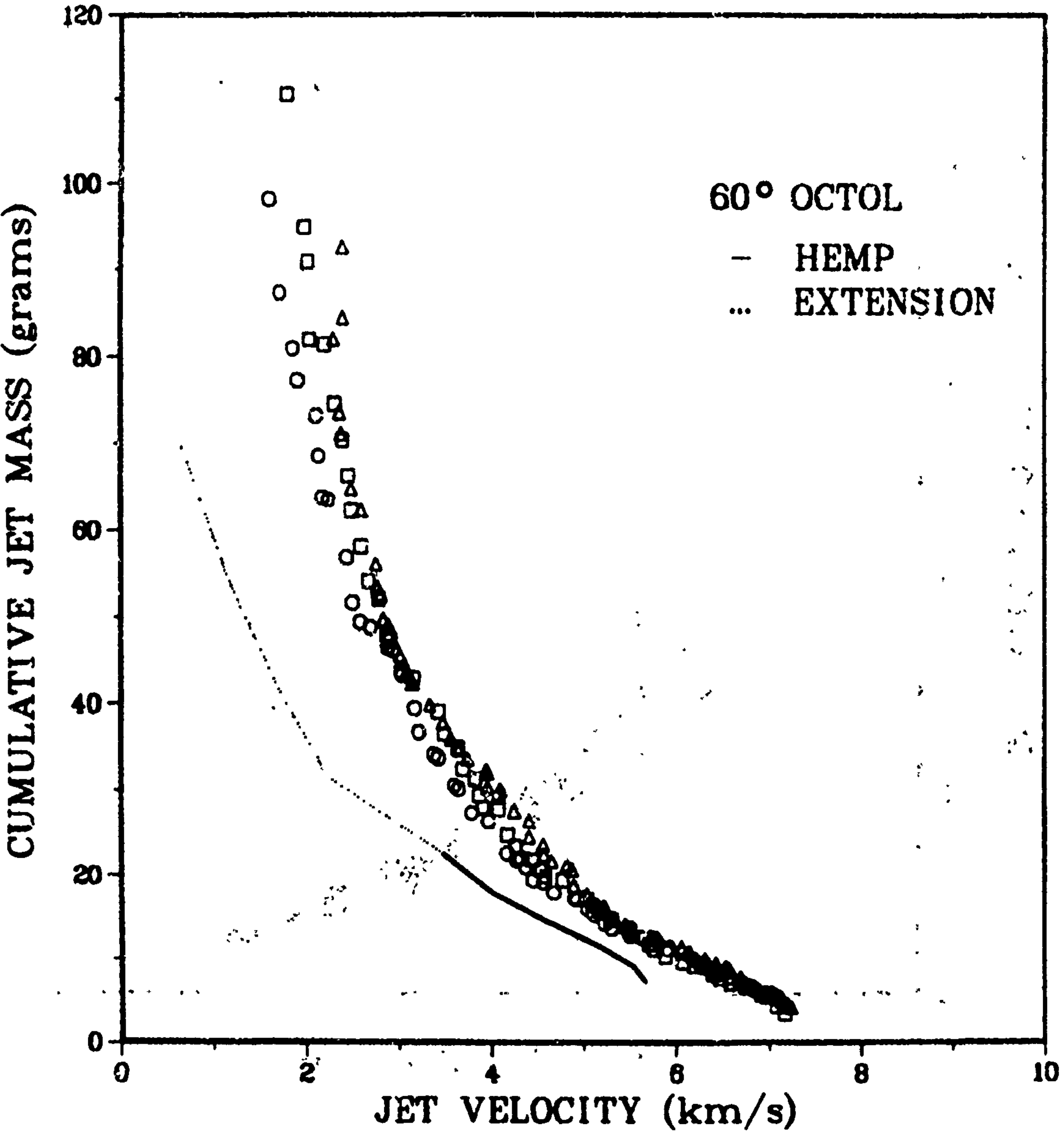

D-3-b. 60°, Octol Simulation, Basic Configuration.

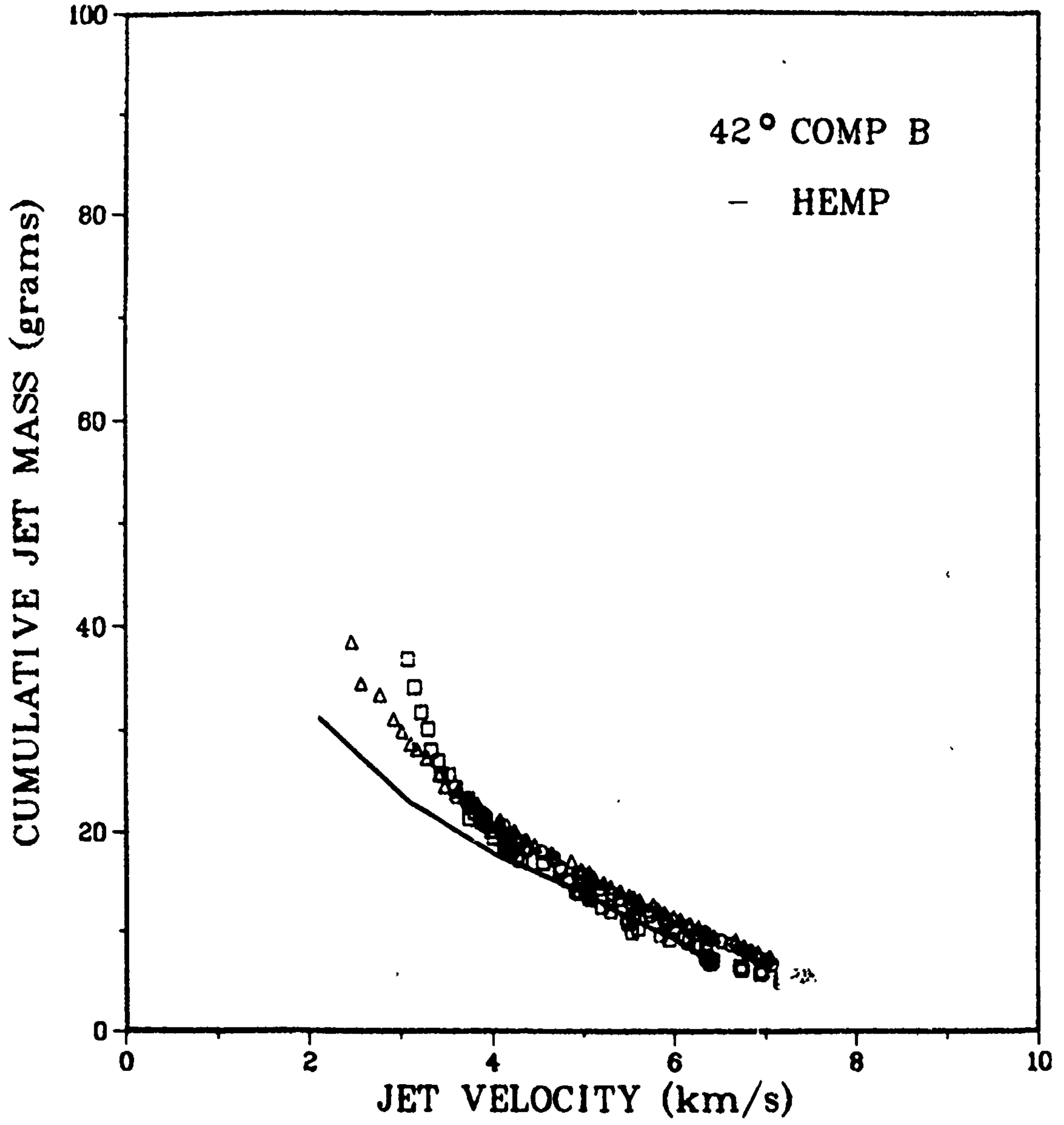

D-4-a, 42°, Comp. B Simulation, Curved Apex Configuration.

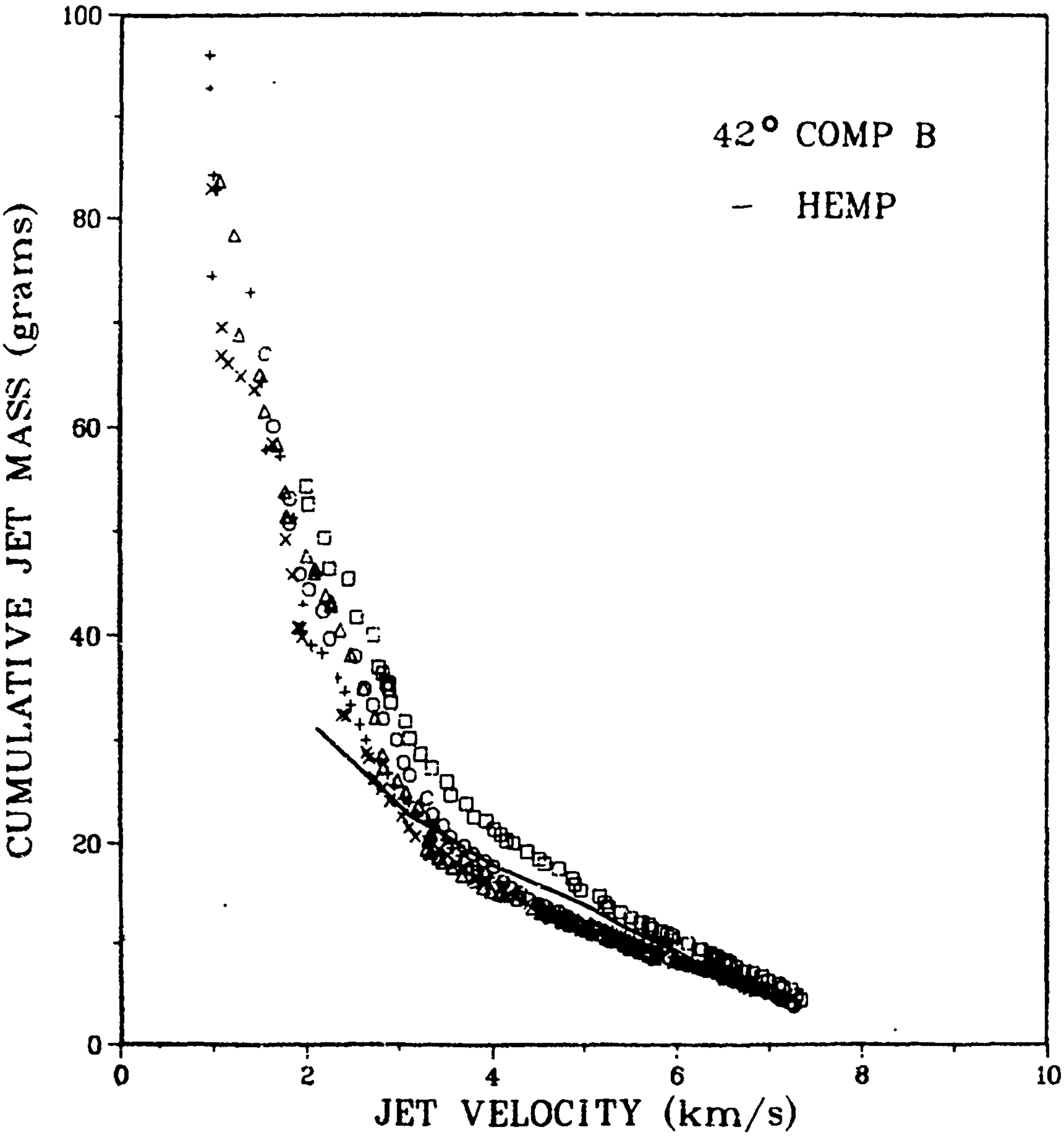

D-4-b. 42°, Comp. B Simulation, Curved Apex Configuration.

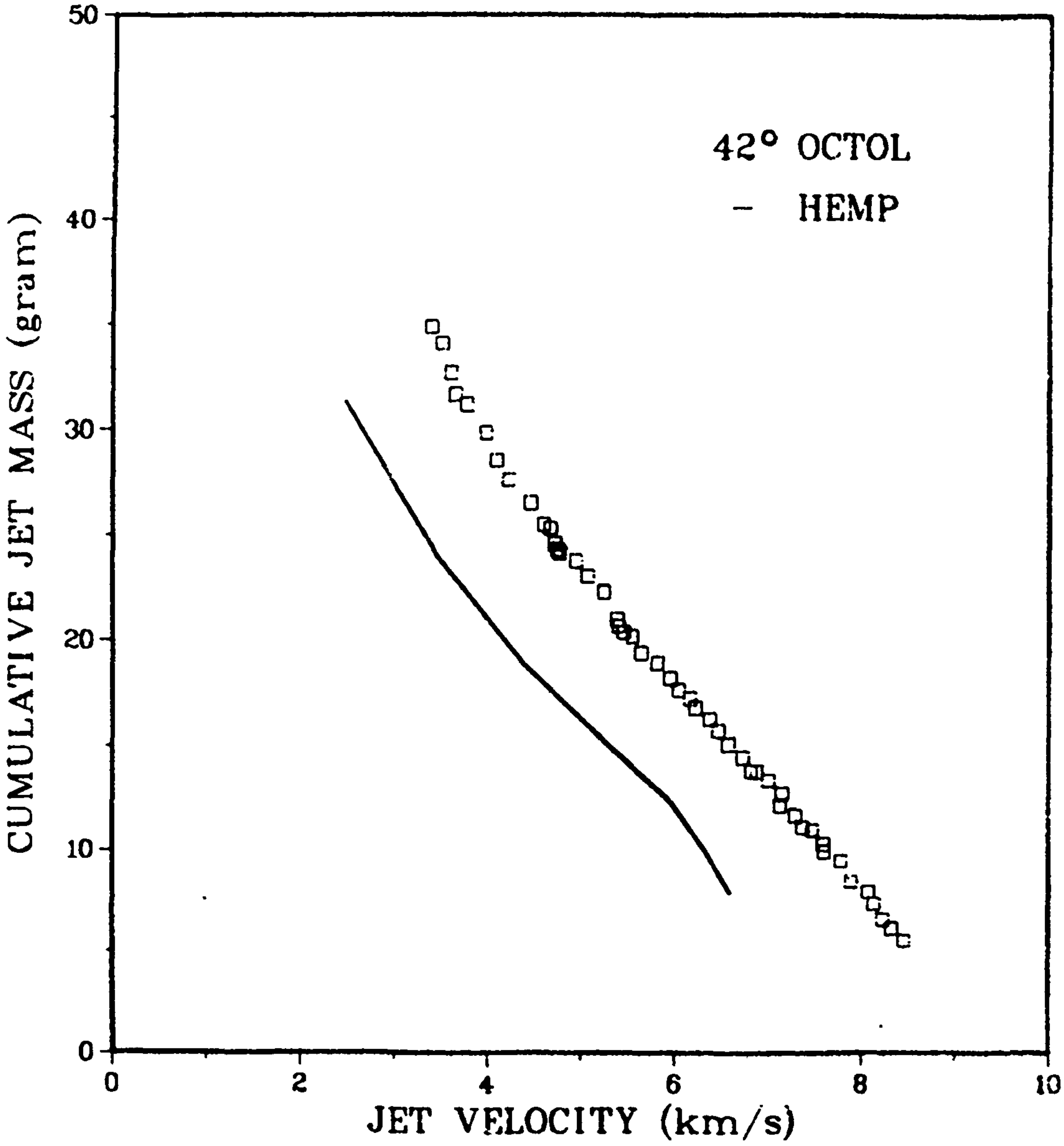

D-5. 42°, Octol Simulation, Curved Apex Configuration.

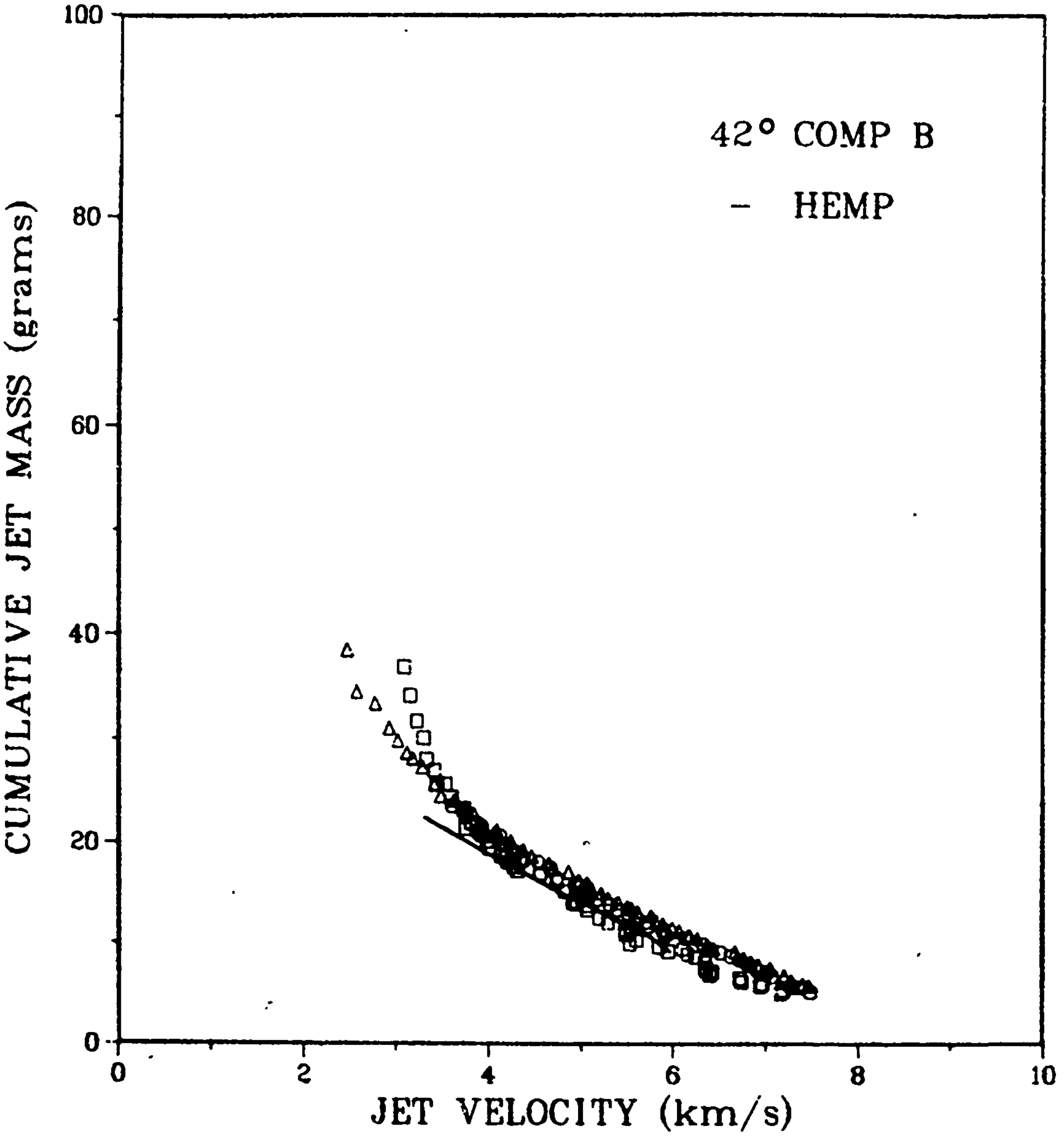

D-6-a. 42°, Comp. B Simulation, Curved Apex Configuration, Polar Zoning.

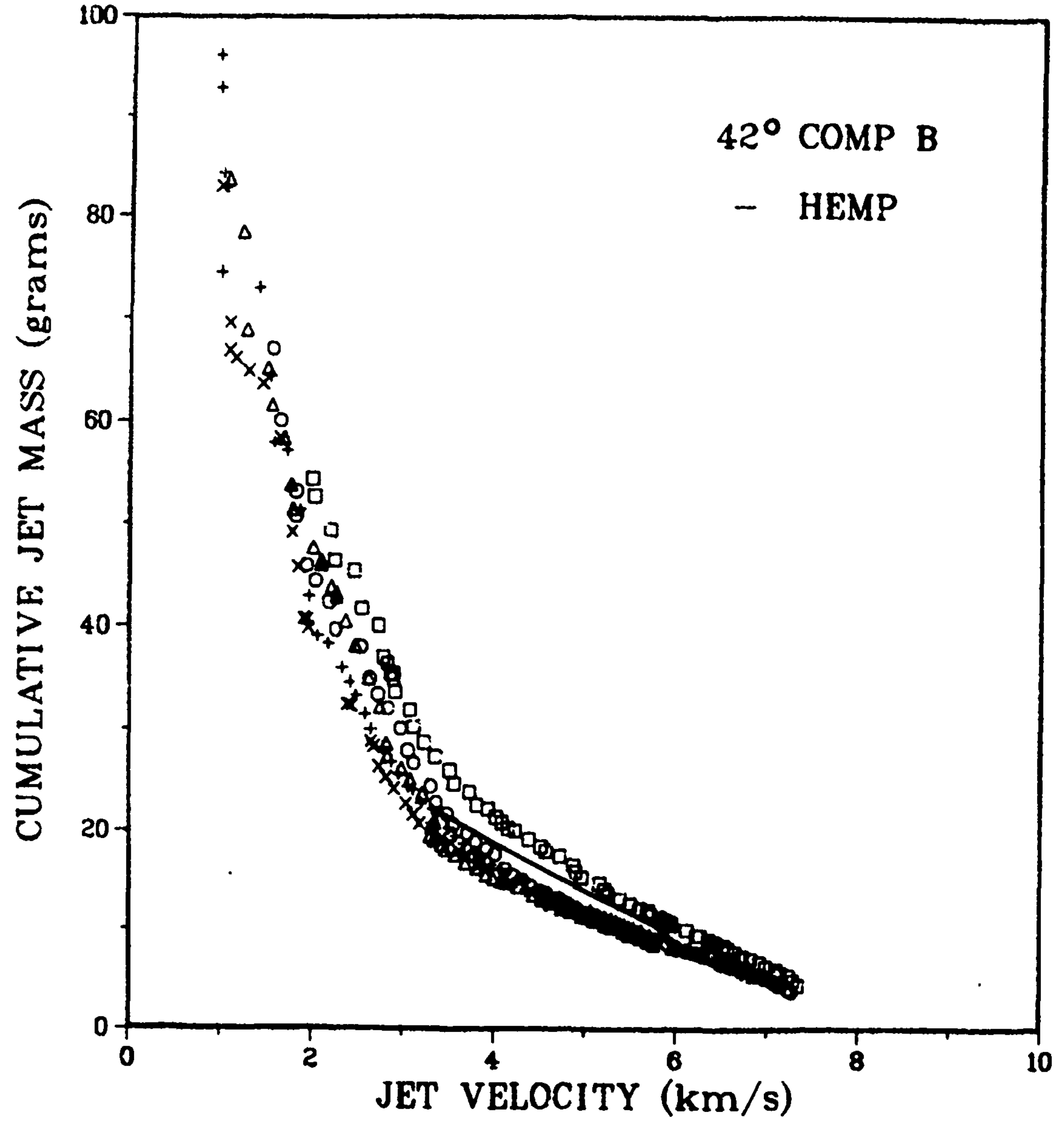

D-6-b. 42°, Comp. B Simulation, Curved Apex Configuration, Polar Zoning.

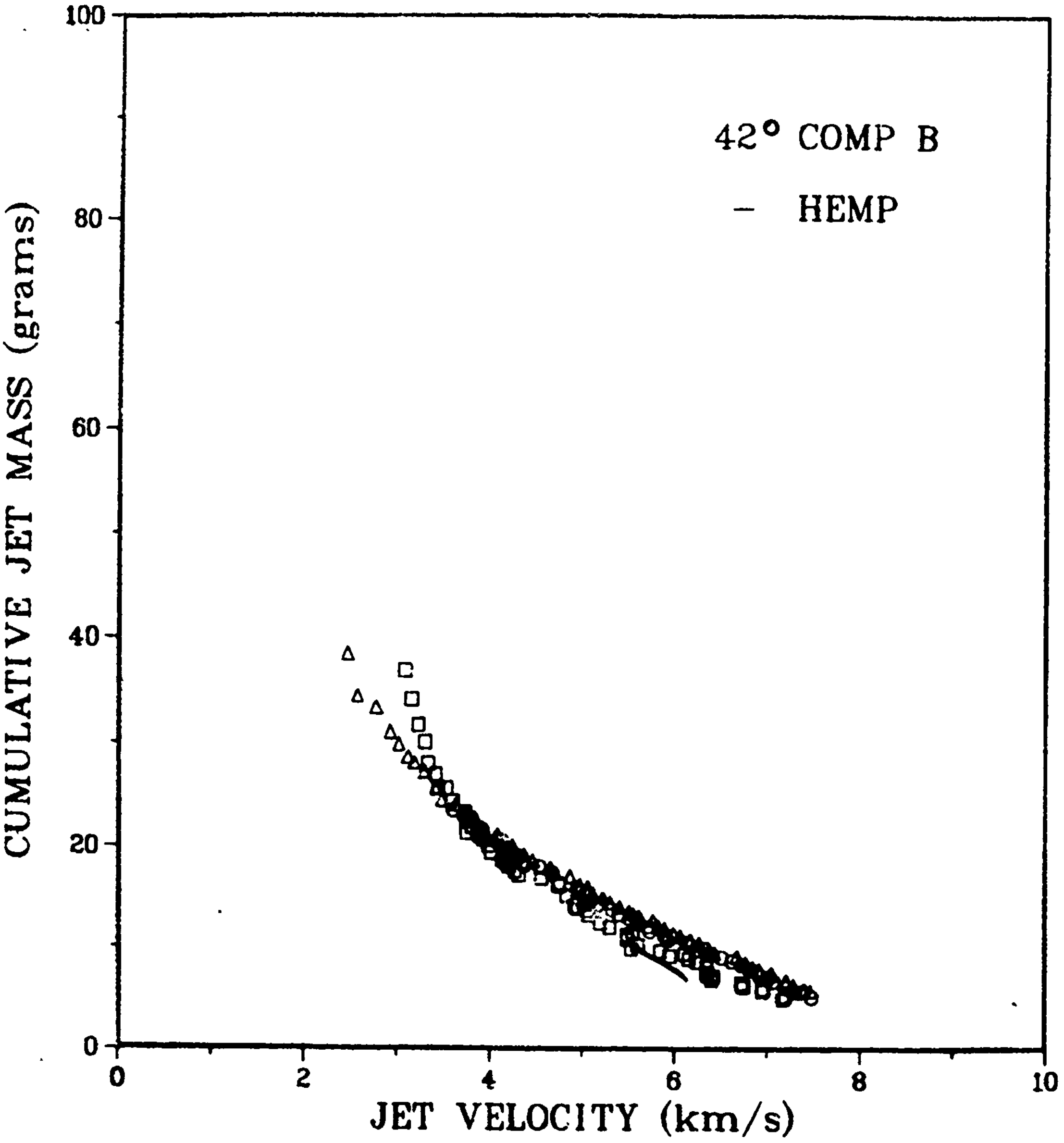

D-7-a. 42°, Comp. B Simulation, Double-Zoning Configuration.

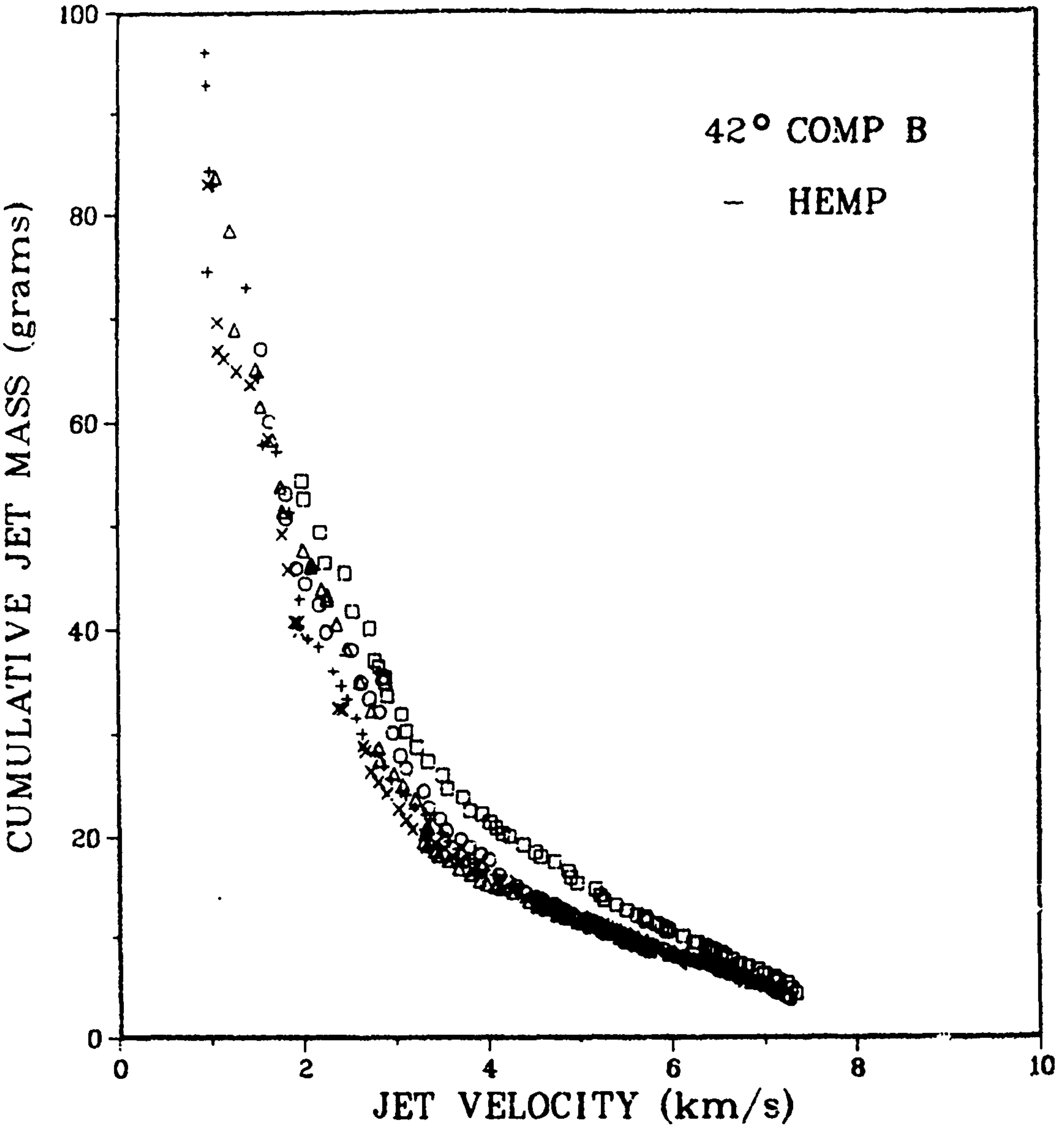

D-7-b. 42°, Comp. B Simulation, Double-Zoning Configuration.

DISTRIBUTION LIST

Copies Organization

12 Administrator
Defense Technical Infor Center
ATTN; DTIC-DDA
Cameron Station
Alexandria, VA 22314

1 Commander
US Army Materiel Command
ATTN: AMCDRA-ST
5001 Eisenhower Avenue
Alexandria, VA 22333

1 Commander
Armament R&D Center
US Army AMCCOM
ATTN: SMCAR-TDC
Dover, NJ 07801

1 Commander
Armament R&D Center
US Army AMCCOM
ATTN: SMCAR-TSS
Dover, NJ 07801

1 Commander
US Army Armament, Munitions
and Chemical Command
ATTN: AMSMC-LEP-L
Rock Island, IL 61299

1 Director
Benet Weapons Laboratory
Armament R&D Center
US Army AMCCOM
ATTN: SMCAR-LCB-TL
Watervliet, NY 12189

1 Commander
US Army Aviation Research
and Development Command
ATTN: AMSAV-E
4300 Goodfellow Blvd
St. Louis, MO 63120

1 Commander
US Army Development and
Employment Agency
ATTN: MODE-TED-SAB
Fort Lewis, WA 98433

Copies Organization

1 Director
US Army Air Mobility Research
and Development Laboratory
Ames Research Center
Moffett Field, CA 94035

1 Commander
US Army Communications Rsch
and Development Command
ATTN: AMSEL-ATDD
Fort Monmouth, NJ 07703

1 Commander
US Army Electronics Research
and Development Command
Technical Support Activity
ATTN: AMDSD-L
Fort Monmouth, NJ 07703

1 Commander
US Army Missile Command
ATTN: AMSMI-R
Redstone Arsenal, AL 35898

1 Commander
US Army Missile Command
ATTN: AMSMI-YDL
Redstone Arsenal, AL 35898

1 Commander
US Army Tank Automotive
Command
ATTN: AMSTA-TSL
Warren, MI 48090

1 Director
US Army TRADOC Systems
Analysis Activity
ATTN: ATAA-SL
White Sands Missile Range
NM 88002

1 Commandant
US Army Infantry School
ATTN: ATSH-CD-CSO-OR
Fort Benning, GA 31905

1 AFWL/SUL
Kirtland AFB, NM 87117

DISTRIBUTION LIST

Copies	Organization
1	Assistant Secretary of the Army (R&D) ATTN: Asst for Research Washington, DC 20310
2	Commander Armament R&D Center US Army AMCCOM ATTN: SMCAR-TSS Mr. G. Randers-Pehrson Mr. J. Pearson Dover, NJ 07801
2	Commander US Army Materials and Mechanics Research Center ATTN: AMXMR-RD, J. Mescall Tech Lib Watertown, MA 02172
1	Army Research Office Durham ATTN: R. Singleton P.O. Box 12211 Research Triangle Park NC 27709
1	Director US Army TRADOC Systems Analysis Activity ATTN: ATAA-SL, Tech Lib White Sands Missile Range NM 88002
2	Chief of Naval Research Department of the Navy ATTN: Code 427 Code 470 Washington, DC 20325
2	Commander Naval Air Systems Command ATTN: Code AIR-310 Code AIR-350 Washington, DC 20360
1	HQDA DAMA-ART-M Washington, DC 20310
1	Commander Naval Ordnance Systems Command ATTN: Code ORD-0332 Washington, DC 20360
4	Commander Naval Surface Weapons Center ATTN: Code DG-50 DX-21, Lib Br N. Coleburn, R-13 Code 730 White Oak, MD 20910
3	Commander Naval Surface Weapons Center ATTN: Code G13, T. Wasmund Code G13, D. Dickinson Tech. Lib. Dahlgren, VA 22448
3	Commander Naval Weapons Center ATTN: Code 4057 Code 45, Tech Lib Code 3261, M. Alexander China Lake, CA 93555
1	David W. Taylor Naval Ship R&D Center ATTN: D. R. Garrison, Code 1740.3 Bethesda, MD 20084
1	Commander Naval Research Laboratory Washington, DC 20375
1	USAF/AFRDDA Washington, DC 20311
1	AFSC/SDW Andrews AFB, MD 20334
2	US Air Force Academy ATTN: Code FJS-41 (NC) Tech Lib Colorado Springs, CO 80840

DISTRIBUTION LIST

Copies Organization

1 AFATL/DLJR (J. Foster)
Eglin AFB, FL 32542

1 AFWL (SUL, LT Tennant)
Kirtland AFB, NM 87117

1 AFWL/WR
Wright-Patterson AFB, OH
45433

6 Director
Lawrence Livermore Laboratory
ATTN: Dr. J. Kury
Dr. M. Wilkins
Dr. E. Lee
Dr. H. Horning
Dr. M. Van Thiel
Technical Library
P.O. Box 808
Livermore, CA 94550

1 Battelle-Columbus Laboratories
ATTN: Technical Library
505 King Avenue
Columbus, OH 43201

1 Dyna East Corporation
ATTN: P. C. Chou
227 Hemlock Road
Wynnewood, PA 19096

1 Aerojet Ordnance Corporation
ATTN: Warhead Tech. Dept.
Dr. J. Carleone
2521 Michelle Drive
Tustin, CA 92680

1 Physics International Company
Tactical Systems Group
Eastern Division
ATTN: E.R. Berus
901 Seville Road
Wadsworth, OH 44281

1 Honeywell, Inc.
Government and Aerospace
Products Division
ATTN: G. Johnson
600 Second Street, NE
Hopkins, MN 55343

1 Director
Sandia National Laboratory
ATTN: Technical Library
Albuquerque, NM 87115

Copies Organization

1 S-CUBED
ATTN: Dr. R. Sedgwick
P.O. Box 1620
La Jolla, CA 92038-1620

1 Physics International Company
Ordnance Technology Department
Computational Physics Group
ATTN: D. Davidson
2700 Merced Street
San Leandro, CA 94577

4 University of California
Los Alamos Scientific Lab
ATTN: Dr. J. Walsh
Dr. R. Karpp
Dr. C. Mautz
Technical Library
P.O. Box 1663
Los Alamos, NM 87545

1 University of Denver
Denver Research Institute
ATTN: Mr. R. F. Recht
2390 S. University Blvd.
Denver, CO 80210

2 University of Illinois
Dept of Aeronautical and
Astronautical Engineering
ATTN: Prof. A. R. Zak
Prof. S. M. Yen
Urbana, IL 61801

Aberdeen Proving Ground

Dir, USAMSAA
ATTN: AMXSY-D
AMXSY-MP, H. Cohen
AMXSY-R, R. Simmons
Cdr, USATECOM
ATTN: AMSTE-TO-F
Cdr, CRDC, AMCCOM
ATTN: SMCCR-RSP-A
SMCCR-MU
SMCCR-SPS-IL